Radiative simulations of moderately magnetized accreting pulsars as ultraluminous X-ray sources

Author:
Fatemeh Kayanikhoo

A thesis submitted in partial fulfillment of the requirements
for the Doctor of Philosophy degree in Astronomy

Nicolaus Copernicus Astronomical Center
at the
Polish Academy of Science (CAMK PAN)

Supervisors:
Prof. Włodzimierz Kluźniak, Dr. Miljenko Čemeljić

Warsaw, June 2024

Dedication

To my wonderful family

To my supportive parents, Shahnaz and Esmaeel, your constant encouragement and belief in me have been my foundation. I am deeply grateful for everything you have done for me since I was a little girl.

To my smart and strong sister, Samira, you were always there whenever I was tired, sad, and needed emotional support. Your unwavering support and friendship have kept me going through the toughest times.

To my joyful and intelligent brother, Mehdi, your humor and positive attitude always made me happy and kept me going.

Your love and support made this journey possible.

Acknowledgements

My academic journey began years ago when I decided to tie my life to physics and astronomy—a journey that has not yet reached its end! Throughout these years, I have experienced many ups and downs. I have met numerous individuals, each of whom has left a lasting impact on my life. Some steps of my life were incredibly challenging, while others were joyful, and I cherish every single one of them. I am deeply grateful to all those who supported me in various ways during the four years of my PhD study and writing this thesis. Their assistance has been invaluable, and I am thankful for their encouragement and guidance.

I would like to begin by sincerely thanking my thesis advisors, Prof. Włodek Kluźniak and Dr. Miljenko Čemeljić, for their guidance, encouragement, and patience throughout my research projects.

I also warmly thank Dr. David Abarca, my friend and colleague, for our discussions and his technical help and support.

I thank my groupmate and collaborator, Dr. Maciek Wielgus, for his guidance and the idea that initiated the first project of my PhD.

I am grateful to Prof. Constança Providência, my dear advisor at Coimbra University. She opened a new window in my life! My wonderful journey in Poland began with her support and advice.

I extend my gratitude to my colleagues at the Nicolaus Copernicus Astronomical Center for their discussions, advice, and assistance, which contributed to a deeper understanding of the universe. I am particularly thankful to Prof. Krzysztof Nalewajko, Prof. Leszek Zdunik, Prof. Agata Różańska, and Prof. Jean-Pierre Lasota.

Additionally, I would like to thank my friends and group mates, Ruchi, Angelos, Tomek, Debora, and Deepika for their companionship. Together, we shared wonderful moments and memorable scientific trips.

I want to express my thanks to my emotional supporters. First of all, my dearest, my dog, **Pepi**, gave me pure love and full attention. She was with me on more than 15 scientific travels; no matter how difficult it was, she never left me alone. Pepi is the best companion I have ever had, and words cannot express my emotions towards her.

I am grateful to Kasia and David for their friendship, to my Persian friends: Sedighe for her emotional support and belief in me, and to Reza who always helped me whenever I needed it. I also extend my heartfelt thanks to my Polish grandma Ela, who always made me feel at home.

Last but not least, I am grateful to Dominik. The past year he has been the best companion for me and Pepi. We shared wonderful observation trips and adventures. He not only helped me with technical problems related to my simulations and analyses but also supported me in every possible way. His belief in me makes me much stronger and makes this journey easier. *Zawsze jesteś mi potrzebny w moim życiu!*

Abstract

The subject of this thesis is the numerical simulation of ultraluminous X-ray sources (ULXs), that are powered by neutron stars with moderately strong dipolar magnetic fields.

A numerical test has been conducted, evaluating the performance of codes in astrophysics, the General Relativistic Radiative Magnetohydrodynamics (GRRMHD) code `Koral` and the Newtonian code `Pluto` through simulations of the Orszag-Tang problem–a simple yet well-established test for magnetohydrodynamics (MHD) codes. A qualitative and quantitative comparison of codes has been performed between the results obtained from simulations in different MHD models, resolutions, and dimensions. Numerical diffusion has been estimated and the resolution at which the results are physical with the least impact of numerical error has been determined using resistive MHD simulations in `Pluto`. It has been demonstrated that `Koral` excels in capturing substructures in numerical simulations with higher accuracy and exhibits reduced numerical dissipation compared to `Pluto`. Consequently, it has been concluded that it is feasible to conduct simulations using `Koral` at lower resolutions than in `Pluto`.

Ten numerical simulations of super-Eddington accretion onto the neutron star with a dipolar magnetic field of moderate strengths (10^{10-11} G) have been conducted using the `Koral` code. The goal was to find the magnetic dipole strength and accretion rate at which the accreting neutron star exhibits the apparent luminosity of observed ULXs. The study has been divided into two parts: In the first part, the simulations have been performed with six different dipole strengths and mass accretion rates of not less than 200 Eddington luminosities. It has been found that the weaker dipole simulation results in higher apparent luminosity compared to the stronger dipole. In weak dipole simulations (10^{10} G), the apparent luminosity is about 120 Eddington units. For the dipole one order of magnitude stronger (10^{11} G) this value is only 40 Eddington units. In the second part, the impact of the accretion rate has then been investigated by comparing three accretion rates for two different dipole strengths, 3×10^{10} and 10^{10} G. The apparent luminosity increases with the increase of the accretion rate. However, for both dipole strengths with accretion rates beyond 300 Eddington luminosities, apparent luminosity is exceeding ~ 100 Eddington units, which is compatible with ULX observations.

Streszczenie

(Abstract in Polish)

Przedmiotem tej pracy są symulacje numeryczne ultrajasnych źródeł rentgenowskich (ULX), zasilanych przez akrecję na gwiazdy neutronowe z umiarkowanymi dipolowymi polami magnetycznymi.

Przeprowadzono test numeryczny oceniający wydajność kodów numerycznych w astrofizyce: kodu `Koral`, rozwiązującego równania ogólno-relatywistycznej promienistej magnetohydrodynamiki (GRRMHD) oraz kodu newtonowskiego `Pluto`. Symulowano problem Orszaga-Tanga – prosty, ale powszechnie uznany problem testowy dla kodów magnetohydrodynamicznych (MHD). Przeprowadzono jakościowe i ilościowe porównanie obu kodów na podstawie wyników uzyskanych z symulacji w różnych modelach MHD, rozdzielczościach i wymiarach. Oszacowano dyfuzję numeryczną i określono rozdzielczość, przy której wyniki są fizyczne przy najmniejszym wpływie błędu numerycznego, wykorzystując symulacje rezystywnej MHD w `Pluto`. Wykazano, że `Koral` z większą dokładnością wychwytuje podstruktury w symulacjach numerycznych i wykazuje mniejszą dyssypację numeryczną w porównaniu z `Pluto`. W związku z tym stwierdzono, że za pomocą kodu `Koral` możliwe jest przeprowadzanie symulacji przy niższych rozdzielczościach niż w przypadku `Pluto`.

Za pomocą kodu `Koral` przeprowadzono dziesięć symulacji numerycznych akrecji super-Eddingtonowskiej na gwiazdę neutronową z dipolowym polem magnetycznym o umiarkowanej wartości (10^{10-11} G). Celem było znalezienie siły dipola magnetycznego i tempa akrecji, przy których akreująca gwiazda neutronowa wykazuje jasność pozorną równą obserwowanym ULX. Badania wykonano w dwóch krokach. W pierwszym, przeprowadzono symulacje z sześcioma różnymi siłami dipola i tempami akrecji nie mniejszymi niż 200 jasności Eddingtona. Stwierdzono, że symulacja ze słabszym dipolem skutkuje wyższą jasnością pozorną w porównaniu do symulacji z silniejszym dipolem. Dla wartości pola (10^{10} G) jasność pozorna wynosi około 120 jednostek Eddingtona, a dla pola o rząd wielkości silniejszego – 40 jednostek Eddingtona. W drugim kroku zbadano wpływ tempa akrecji, symulując trzy wartości tempa akrecji dla dwóch różnych wartości pól magnetycznych 3×10^{10} i 10^{10} G. Jasność pozorna rośnie wraz ze wzrostem tempa akrecji. Jednak dla obydwu dipoli z tempem akrecji przekraczającym 300 jasności Eddingtona skutkują jasnością pozorną przekraczającą $\sim$ 100 jednostek Eddingtona, co jest zgodne z obserwacjami ULX.

Contents

Chapter 1

Introduction

This thesis investigates ULXs driven by super-Eddington accretion onto neutron stars with moderate-strength dipolar magnetic fields. ULXs are non-nuclear extragalactic sources that emit X-rays at luminosities exceeding $10^{39}\,\mathrm{erg\,s^{-1}}$.

The discovery of coherent pulsations in ULX emission (Bachetti, Harrison, et al., 2014) suggested that the central object is a neutron star accreting beyond its Eddington limit.

Both numerical simulations and analysis of observational data are necessary to explore the physics responsible for the pulsation and high-rate X-ray emission of ULXs. However, simulation of accreting neutron stars is challenging due to their hard surface and intrinsic magnetic field.

I perform numerical simulations of super-Eddington accretion onto a neutron star with moderately strong dipolar magnetic fields in a general relativistic radiative magnetohydrodynamic (GRRMHD) code. I aim to find the limits of the strength of dipole and accretion rate in which the ULXs are powered by accreting neutron stars.

The introduction chapter is structured as follows: Accretion-powered X-ray pulsars are described in the first Section 1.1. ULXs are discussed in Section 1.2. The final section of the introduction focuses on the numerical simulations used to study accreting compact objects, including neutron stars, with the description of the numerical simulation code `Koral` that is used in my study.

1.1 Accretion powered X-ray pulsars

Pulsars are magnetized rotating neutron stars that emit beams of electromagnetic radiation. These beams are characterized by regular pulsing signals, which can be detected in radio, optical, X-ray, and gamma-ray wavelengths. The first pulsar was discovered by Hewish, Bell, et al. (1968) with emission in radio wavelengths and is often recognized as the first observationally confirmed neutron star.

A few months before the discovery of the first radio pulsar, Shklovsky (1967) accurately indicated that Scorpius X-1 is powered by an accreting neutron star. X-ray pulsars represent a significant subclass of pulsars characterized by their accretion-powered X-ray emissions. These pulsars are typically found in binary systems, where the intense gravitational field of the neutron star draws material from its companion star. The gravitational energy of accreted material dissipates to X-ray emission.

The focus of my thesis is on accretion-powered X-ray pulsars, so I introduce X-ray binaries, focusing on those containing neutron stars.

1.1.1 X-ray binaries

In X-ray binary systems, accretion onto the compact object can occur either from the stellar winds of the companion or from matter transfers when the companion overflows its Roche-lobe. According to the companion star, X-ray binaries are categorized into two main groups, low-mass X-ray binaries (LMXBs) and high-mass X-ray binaries (HMXBs).

LMXBs contain a low-mass star companion ($\leq 1\,M_\odot$). These binary systems typically are old with a companion that can be a brown dwarf, white dwarf, or subgiant. The accretion occurs when the companion fills its Roche-lobe. In the LMXBs the magnetic field of the neutron star is $\lesssim 10^9$ G. Their spin period depends on the mass accretion rate and magnetic field of the neutron star e.g. for a neutron star with magnetic field $\sim 10^8$ G and accretion rate near the Eddington limit (Eddington accretion rate is discussed in subsection 'Accretion rate') the spin period is about millisecond (Harding, 2013). The X-ray luminosity of neutron star LMXBs in quiescence state is about $10^{32-33}\,\mathrm{erg\,s^{-1}}$(Tomsick, Gelino, et al., 2004; Meyer-Hofmeister, Cheng, & Liu, 2024).

HMXBs typically involve a massive star (O or B type) with a mass larger than solar mass. In HMXBs accretion often occurs via stellar winds from the massive companion and it is rarely observed that the companion overflows its Roche-lobe (Kretschmar, Fürst, et al., 2019). The magnetic field of the neutron star in HMXBs is about 10^{11} - 10^{13} G, and the spin period is from less than a second to 12 minutes (King, Lasota, & Middleton, 2023). Particularly, Her-X1 has the magnetic field of 10^{12} G and a $2\,M_\odot$ companion (Truemper, Pietsch, et al., 1978). A large number of HMXBs are Be-X binary systems containing a neutron star and a B-type companion. Be-X binaries have a wide, eccentric orbit. This results in periodic accretion of material when the neutron star crosses through a disk surrounding the B-type star. These binaries have a steady luminosity about $10^{32}\,\mathrm{erg\,s^{-1}}$. They emit X-ray $\gtrsim 10^{39}\,\mathrm{erg\,s^{-1}}$ during outburst, classifying them as ULXs (see review by King, Lasota, & Middleton, 2023, and references therein).

Another interesting observed property of neutron star HMXBs is pulsation. The magnetic field of the neutron star is strong enough to truncate the accretion in the inner region of the disk, and the gas is forced to move along the field lines toward the pole of the neutron star. The gravitational energy of infalling material that is released in the form of X-ray is not emitted isotropically, and the misalignment of the rotation and magnetic field axes causes the periodic pulsation for a distant observer (Giacconi, Gursky, et al., 1971). The pulsations observed in ULXs (Bachetti, Harrison, et al., 2014) have introduced an interesting new area of study in the field of X-ray pulsars.

In my thesis, I study models of ULXs powered by accreting pulsars in HMXBs.

Accretion mechanism

The accretion disk of compact objects, such as black holes or neutron stars, is a structure formed by material spiraling towards the compact object. Transfer of the matter towards the compact object is attributed to the loss of angular momentum.

The gas particles within the disk collide and interact, losing the angular momentum through viscous friction and magnetic diffusion.

Effective viscosity in the disk plays a crucial role in angular momentum transfer, often parameterized using the α viscosity when the dominant component of the viscous stress tensor is proportional to the pressure: $T_{\mathrm{r}\phi} = \alpha P$ (Shakura & Sunyaev, 1973). High viscosity facilitates the transfer of angular momentum outward, enabling the material to move inward. As the material in the disk moves closer to the compact object, gravitational energy is converted into thermal energy, causing the disk to heat up. This process results in the emission of X-rays, which are particularly intense near the inner regions of the disk where temperatures can reach millions of degrees.

Magnetorotational instability (MRI) is the fundamental mechanism allowing angular momentum transfer within accretion disks, enabling the movement of material towards the compact object. MRI manifests in the presence of a weak magnetic field within a differentially rotating disk (Balbus & Hawley, 1991; Balbus & Hawley, 1998). The instability arises when magnetic field lines within the disk connect parcels of gas at different radii. Magnetic tension acts as a mediator between the deferentially rotating gas parcels facilitating the transfer of angular momentum between them. This process results in the outward transport of angular momentum and the inward flow of matter.

MRI plays a crucial role in generating turbulence within the disk, significantly increasing its viscosity and thereby enhancing the rate of accretion. The turbulence driven by MRI sustains the conditions necessary for continuous accretion and the consequent high-energy emissions observed from compact objects. In the context of this study, the simulations are conducted utilizing the MRI mechanism.

Magnetospheric radius

In the accreting neutron star system the magnetic field of the neutron star can be strong enough to truncate the disk at a radius known as Alfvén or magnetospheric radius. The disk is truncated where the ram pressure is equal to the magnetic pressure. At this radius accreting material is forced to follow the magnetic field lines towards the neutron star pole, forming accretion columns. A basic estimation of this radius by assuming the spherical accretion free-falling onto a dipolar magnetic field was done by Elsner & Lamb (1977),

$$R_{\mathrm{m}}^{\mathrm{EL}} = \left(\frac{\mu^4}{2GM\dot{M}^2}\right)^{1/7} = 3.2\times10^8 \dot{M}_{17}^{-2/7}\mu_{30}^{4/7}\left(\frac{M}{M_\odot}\right)^{1/7}\ \mathrm{cm}, \tag{1.1}$$

where $\mu_{30} = 10^{30}\mu$ with the magnetic moment μ and $\dot{M}_{17} = 10^{17}\dot{M}$ with the accretion rate $\dot{M}$. So the magnetospheric radius $R_{\mathrm{m}}^{\mathrm{EL}}$ is proportional to $\dot{M}^{-2/7}\,\mu^{4/7}$.

I note that numerical models are more complicated and the estimated magnetospheric radius does not precisely follow the analytical solution. In my simulations, the inner part of the disk is radiation-dominated. The disk is nearly Keplerian and although the radial velocity is large, it is a fraction of the free-falling velocity. Thus it is expected that the numerical models may not be consistent with the analytical solution.

Corotation radius

A radius at which Keplerian angular velocity in the disk and the neutron star angular velocity $\Omega_{\rm NS}$ are the same is called the corotation radius $R_{\rm co}$,

$$R_{\rm co} = \left(\frac{GM}{\Omega_{\rm NS}^2}\right)^{1/3}. \tag{1.2}$$

If $R_{\rm m} \leq R_{\rm co}$, accretion is possible and the angular momentum of the accreting material may be transferred to the neutron star, causing its spin-up. Conversely, when $R_{\rm m} > R_{\rm co}$ the centrifugal force can be stronger than the gravitational force causing the accreting material to be ejected. This may happen when the neutron star is rotating rapidly enough and has a strong magnetic field. This scenario is known as the propeller regime (Illarionov & Sunyaev, 1975; Papitto & Torres, 2015). The propeller regime is not the subject of my study.

Spherization radius

The radius at which the total emitted radiation exceeds the Eddington limit is referred to as the spherization radius $R_{\rm sph}$ (Shakura & Sunyaev, 1973). Within the radius $R_{\rm sph}$, radiation induces outflow which is discussed in the following subsection 'Accretion rate'.

There are slightly different approaches to compute the spherization radius, as detailed in the review paper by King, Lasota, & Middleton (2023). Here, I will briefly discuss one method to compute this radius.

The spherization radius for the thin disk can be computed by equality of the local radiative flux generated by viscosity $F_{\rm vis}$ (Frank, King, & Raine, 2002) within the disk and the local Eddington flux: $F_{\rm visc} = F_{\rm Edd} = L_{\rm Edd}/(4\pi R^2)$. This gives the spherization radius $R_{\rm sph} = 15\dot{m} r_{\rm g}$, where the accretion rate is $\dot{m} = \dot{M}/\dot{M}_{\rm Edd}$ ($\dot{M}_{\rm Edd}$ is the Eddington accretion rate) and the gravitational radius is $r_g = GM/c^2$. Considering that the outer region around the compact object can be strongly self-irradiated, we can write $F_{\rm Edd} = F_{\rm vis} + F_{\rm irr}$, with the equation irradiated flux $F_{\rm irr}$ given in Dubus, Lasota, et al. (1999). Thus, the spherization radius is

$$R_{\rm sph} = 15\left(1 - C\frac{\dot{m}}{2}\right)^{-1} \dot{m}\, r_{\rm g}, \tag{1.3}$$

where the constant $C \sim 10^{-2}$ (Dubus, Hameury, & Lasota, 2001). However, the spherization radius is computed for the thin disk model and is not accurately applicable to my model.

Accretion rate

As the accreting material moves toward the compact object through the accretion disk with the rate of $\dot{M}$, it releases energy L. The released energy is a fraction η of the accretion rate,

$$L = \eta \dot{M} c^2, \tag{1.4}$$

where the parameter η represents the efficiency of gravitational mass-to-energy conversion. In the Newtonian gravitational potential, if the disk ends at the radius $6\, r_{\rm g}$, efficiency is 1/12. In the relativistic estimate for a geometrically thin disk around

the non-rotating black hole, this value reaches 0.057 and for a maximally rotating black hole, it increases to 0.4 (Shakura & Sunyaev, 1973). The efficiency for the accreting neutron star with the radius $5\,r_{\rm g}$ is about 0.1, as discussed in Syunyaev & Shakura (1986).

If the accretion disk releases the energy equal to Eddington $L_{\rm Edd}$, then we can define

$$\dot{M}_{\rm Edd} = \frac{L_{\rm Edd}}{\eta_0 c^2} \tag{1.5}$$

where η_0 is the assumed efficiency.

When the accretion rate is a small fraction of the Eddington accretion rate ($\dot{M} \lesssim 10^{-4}\dot{M}_{\rm Edd}$), the disk becomes optically thin and does not cool efficiently. At this rate, radiation pressure expands the disk. A similar model of the accretion disk is known as advection-dominated accretion flow (ADAF), in which radiation is advected with the gas (Abramowicz, Czerny, et al., 1988).

It has been known since Shakura & Sunyaev (1973) that super-Eddington ($\dot{M} \gtrsim \dot{M}_{\rm Edd}$) geometrically thin accretion disks result in luminosity surpassing the Eddington luminosity ($L > L_{\rm Edd}$). When the spherization radius is larger than the ISCO in a black hole super-Eddington geometrically thin accretion disk, the disk radiation increases logarithmically,

$$L \simeq L_{\rm Edd}[1 + \ln \dot{m}], \tag{1.6}$$

where $\dot{m} = \dot{M}/\dot{M}_{\rm Edd}$. Thus, if the accretion rate is $100\,\dot{M}_{\rm Edd}$ the disk luminosity is only $\sim 5.6\,L_{\rm Edd}$. In this model, within the spherization radius $R_{\rm sph}$, where the emitted radiation becomes super-Eddington, strong radiation pressure drives powerful outflows from the disk. However, in reality due to the high optical depths in these disks, photons generated in the inner regions are advected over a significant distance before diffusing out, leading to a substantial fraction of them being accreted onto the black hole without escaping. In the case of an accreting neutron star, the advected radiation is supposed to be reflected from the surface of the neutron star (Houck & Chevalier, 1992; Ohsuga, Mineshige, et al., 2002).

In the accreting neutron star system, when accretion is super-Eddington, the accretion channeled along the strong magnetic field lines becomes optically thick. Thus, the radiation can not easily escape, the accretion column becomes radiation pressure dominated, resulting in a radiation shock right above the neutron star surface. Radiation escapes from the side of the accretion column while the accreting material sinks through the dense magnetic field lines. The radiation shock was first studied by Basko & Sunyaev (1976) and later by Mushtukov, Suleimanov, et al. (2015); Revnivtsev & Mereghetti (2014).

1.2 Ultraluminous X-ray sources

ULXs are defined to have apparent X-ray luminosity $L_{\rm X} \geq 10^{39}\,{\rm erg\,s^{-1}}$. Thus, $L_{\rm X}$ is above the critical Eddington luminosity for a compact object with a mass less than $10\,M_\odot$,

$$L_{\rm Edd} = \frac{4\pi G M m_{\rm p} c}{\sigma_{\rm T}} = 1.26 \times 10^{38} \left(\frac{M}{M_\odot}\right) {\rm erg\,s^{-1}}, \tag{1.7}$$

where $m_{\rm p}$ is proton mass, $\sigma_{\rm T}$ is Thompson scattering cross section and $M_\odot$ is the solar mass.

The principle progenitor could be a massive black hole that is accreting below the Eddington limit, a neutron star, or a stellar-mass black hole ($10\,M_\odot$) that is accreting beyond its Eddington limit. ULXs are most likely X-ray binary systems with a compact object accretor.

The first detection of ULXs was during the X-ray survey by Einstein and ROSAT satellites. Fabbiano (1989) reported 16 ULXs with luminosities $L_X > 10^{39}\,\mathrm{erg\,s^{-1}}$. The number of detected ULXs increased quickly with Walton, Mackenzie, et al. (2022) categorizing 1843 ULXs from 951 host galaxies based on data from the XMM-Newton, Swift, and Chandra observatories. Several sources in this catalogue have luminosities higher than $10^{41}\,\mathrm{erg\,s^{-1}}$. There are 10 known magnetized neutron stars and four transient Be-X binary systems between them. Most ULXs are found outside the centers of galaxies, distinguishing them from AGNs. Additionally, the luminosity of ULXs is less than AGNs (about $10^{42}\,\mathrm{erg\,s^{-1}}$ for AGNs in nearby galaxies and about $10^{47}\,\mathrm{erg\,s^{-1}}$ for quasars in distant galaxies).

The study of ULXs started by Colbert & Mushotzky (1999), where they investigated a sample of 20 ULXs with luminosities in the range of $10^{40} - 10^{42}\,\mathrm{erg\,s^{-1}}$. They suggest that the central accretor might be a black hole with a mass range of $10^2 \leq M/M_\odot \leq 10^4$, now called intermediate-mass black holes (IMBHs) (Matsushita, Kawabe, et al., 2000).

The photon bubble instability in the accretion disk of a stellar mass black hole $M/M_\odot \leq 10$ was proposed by Begelman (2002). In this model, the instability occurs because of the interaction between X-ray photons and the gas in the accretion disk. X-ray photons transfer some of their momentum to the surrounding gas particles causing the gas to heat up and expand, forming a bubble-like structure. Thus radiation that escapes from this disk exceeds the predictions of standard accretion disk theory. However, this model could not explain a luminosity higher than $10^{40}\,\mathrm{erg\,s^{-1}}$ without beaming (see Lasota, 2024, and references therein).

In a different scenario, the magnetic fields of accreting neutron stars were suggested to be responsible for a high radiation luminosity. In the presence of the magnetic field $\gtrsim 10^{14}\,\mathrm{G}$, the electron scattering opacity for X-rays reduces, allowing large amounts of X-rays to escape (Canuto, Lodenquai, & Ruderman, 1971; Elsner & Lamb, 1977; Herold, 1979). Paczynski (1992) showed that in the presence of a strong magnetic field, the critical luminosity for an accreting star with the mass $1.4\,M_\odot$ is,

$$L \sim 2 \times 10^{40} \left(\frac{B}{10^{14}\,\mathrm{G}}\right)^{4/3} \mathrm{erg\,s^{-1}}. \tag{1.8}$$

This means that the magnetic field of $B \geq 10^{14}\,\mathrm{G}$ is required for the luminosity $\gtrsim 10^{40}\,\mathrm{erg\,s^{-1}}$ (Mushtukov, Suleimanov, et al., 2015). However, in the review paper by Revnivtsev & Mereghetti (2014), it is reported that the magnetic field of neutron stars in X-ray binaries is observed to be lower than $10^{13}\,\mathrm{G}$. HMXBs exhibit periodic X-ray pulsations indicative of magnetic fields around $10^{12}\,\mathrm{G}$, similar to what is inferred from young radio pulsar spin-down rates. In contrast, the infrequency of pulsations occurring in LMXBs suggests much weaker magnetic fields in these typically older systems.

In a quite different scenario to describe the extremely high luminosity of ULXs, King, Davies, et al. (2001) suggested that ULXs are powered by super-Eddington accretion onto stellar-mass compact objects which could be black holes with mass

Table 1.1: Observed and derived properties of some neutron star ULXs in KLK model (King, Lasota, & Kluźniak, 2017) (updated in Lasota, 2024).

Name	$L_X^{\max}$ [erg/s]	$\dot{\nu}$ [s^{-2}]	$\dot{m}_0$	b	$\boldsymbol{B}$ [G][1]	$\boldsymbol{R}_{\rm sph}$ [cm]	$\boldsymbol{R}_M$ [cm]
M82 ULX2	2.0×10^{40}	10^{-10}	46	0.03	4.0×10^{10}	1.1×10^{8}	1.0×10^{7}
NGC 7793 P13	5.0×10^{39}	2×10^{-10}	25	0.12	1.1×10^{11}	5.8×10^{7}	1.6×10^{7}
NGC5907 ULX1	$\sim 10^{41}$	3.8×10^{-9}	95	0.01	9.4×10^{12}	2.2×10^{8}	1.1×10^{8}
NGC300 ULX1	4.7×10^{39}	5.6×10^{-10}	24	0.13	5.3×10^{11}	5.5×10^{7}	3.2×10^{7}
M51 ULX7	7×10^{39}	2.8×10^{-10}	28	0.09	1.9×10^{11}	6.4×10^{7}	2.0×10^{7}
NGC 1313 X-2	2×10^{40}	1.2×10^{-10}	46	0.03	5.3×10^{10}	1.1×10^{8}	1.8×10^{6}
SMC X-3	2.5×10^{39}	6.9×10^{-11}	18	0.23	2.3×10^{10}	4.1×10^{7}	7.1×10^{6}
NGC 2403 ULX	1.2×10^{39}	3.4×10^{-10}	13	0.43	2.5×10^{11}	3.0×10^{7}	2.3×10^{7}
Swift J0243.6+6124	$\gtrsim 1.5 \times 10^{39}$ (?)[2]	$2. \times 10^{-10}$	14	0.37	1.3×10^{11}	3.2×10^{7}	1.7×10^{7}
RXJ0209.6-7427	$1 - 2 \times 10^{39}$	1.165×10^{-10}	17	0.25	5.3×10^{10}	3.2×10^{7}	1.8×10^{6}

- Systems in the last four rows are transient and have confirmed or suspected Be–star companions.
[1] - B obtained from detected magnetic moment μ assuming $R_{\rm NS} = 10^6$ cm and $M_{\rm NS} = 1\,M_\odot$.
[2] - System in the Galaxy: distance uncertain.

$\sim 10\,M_\odot$, neutron stars or white dwarfs. In this scenario, the high accretion rate plays a crucial role. As mentioned earlier, radiation pressure in a thin disk model within $R_{\rm sph}$ drives powerful outflows. In the accreting neutron star system, there are radiation-driven outflows between spherization and magnetospheric radii when $R_{\rm sph} \geq R_{\rm m}$. The strong outflows create a funnel-like optically thin region near the polar axis. Consequently, the compact object emits its radiation within a fraction b of the unit sphere, causing the luminosity to be overestimated by a factor of $1/b$. If b, known as the beaming factor, is sufficiently small, then the inferred isotropic luminosity, $L_{\rm iso} \sim L/b$ (where L is the true luminosity), could easily reach values of $10^{39} - 10^{41}\,{\rm erg\,s^{-1}}$ (King, 2009).

In the KLK model (King, Lasota, & Kluźniak, 2017; King & Lasota, 2019, 2020) the period, spin-up and luminosity are considered to predict the strength of the magnetic field and the beaming factor in accreting neutron stars. As mentioned earlier, if the magnetospheric radius $R_{\rm m}$ is less than the spherization radius $R_{\rm sph}$ the disk launches outflows that cause the beaming, which is estimated as a function of the accretion rate $\dot{m} = \dot{M}/\dot{M}_{\rm Edd}$ (King, Davies, et al., 2001) with,

$$b \simeq \frac{73}{\dot{m}^2}. \tag{1.9}$$

Utilizing Equations 1.6 and 1.9, one can estimate the apparent luminosity of the accretion disk with an accretion rate of $\dot{m} = 100$ to exceed $800\,L_{\rm Edd}$.

The magnetic field of the neutron star in KLK model is predicted to fall within the range of 10^{10} to 10^{13} G with the majority of results falling between $10^{10} - 10^{11}$ G (King, Lasota, & Kluźniak, 2017). Some of the observed and predicted properties of neutron star ULXs in King, Lasota, & Kluźniak (2017) are shown in Table. 1.1. This range is the basis for the selected magnetic field strengths in this thesis.

1.2.1 Pulsating ULXs (PULXs)

Bachetti, Harrison, et al. (2014) discovered pulsation in ULX M82 X–2 with apparent luminosity $L \sim 1.810^{40}\,\mathrm{erg\,s^{-1}}$ and coherent periodicity $P = 1.37\,\mathrm{s}$. This discovery showed that the accretor must be a neutron star with a super-Eddington accretion which can produce the apparent luminosity more than 100 times its Eddington luminosity.

After the first discovery of PULXs, more investigations reported pulsation in ULXs with periods less than a second to 12 minutes (Chandra, Roy, et al., 2020; Heida, Lau, et al., 2019; Brightman, Harrison, et al., 2018; Fürst, F., Walton, D. J., et al., 2018; Carpano, Haberl, et al., 2018; Doroshenko, V., Tsygankov, S., & Santangelo, A., 2018; Israel, Belfiore, et al., 2017; Townsend, Kennea, et al., 2017; Tsygankov, S. S., Doroshenko, V., et al., 2017; Israel, Papitto, et al., 2016; Bachetti, Harrison, et al., 2014; Motch, Pakull, et al., 2014; Trudolyubov, 2008).

After the discovery of the first PULX, Kluźniak & Lasota (2015) pointed out that this source has an extremely high spin-up rate of $10^{-10}\,\mathrm{s^{-2}}$ that is 2 orders of magnitude higher than the one for normal X-ray pulsars. It demonstrates the torque transfer to the neutron star by the accreting material through the magnetosphere. King, Lasota, & Kluźniak (2017) and later Vasilopoulos, Petropoulou, et al. (2019) assumed the spin-up rate of the accretion,

$$\dot{\nu} = \frac{\dot{J}(R_\mathrm{m})}{2\pi I} = \frac{\dot{M}(GMR_\mathrm{m})^{1/2}}{2\pi I} \propto \dot{M}^{6/7}\mu^{2/7}, \tag{1.10}$$

where $\dot{J}$ is the angular momentum accretion rate and I is the moment of inertia of the neutron star with the magnetospheric radius $R_\mathrm{m} = R_\mathrm{m}^\mathrm{EL}$ (Eq. 1.1). Hence,

$$\dot{M} \approx 5.7 \times 10^{18}\dot{\nu}_{-10}^{7/6}\mu_{30}^{-1/3}\,\mathrm{g\,s^{-1}}. \tag{1.11}$$

Considering the efficiency of accretion $L_\mathrm{X} = 0.1\dot{M}c^2$ (Lasota & King, 2023),

$$L_\mathrm{X} \approx 2 \times 10^{38}\dot{\nu}_{-10}^{7/6}\mu_{30}^{-1/3}\,\mathrm{erg\,s^{-1}}, \tag{1.12}$$

Based on this equation, Lasota & King (2023) noted that the magnetic field strength required to increase the radiation pressure luminosity to the observed isotropic luminosity of PULXs ($L \gg L_\mathrm{Edd}$) is inconsistent with the spin-up rates observed in PULXs. This discovery rejected the idea of ULXs being powered by the accreting onto extremely magnetized neutron stars: PULXs are not powered by accreting magnetars but by pulsars with normal magnetic fields, as predicted by the KLK model and the extraordinary luminosity of ULXs is caused by beaming.

The pulsations observed in PULXs when the neutron star is the accretor are attributed to the effect of the inclination angle of the magnetic field relative to the rotation axis of the neutron star. In some pulsating sources, the inclination angle can affect the observed pulse fraction by changing the geometry of the system so that the observed emission from pulsar changes along the line of sight (Bachetti, Harrison, et al., 2014; Israel, Belfiore, et al., 2017). The magnetospheric and spherization radii must be adjusted to generate adequate outflows for collimating the radiation without overly obstructing the pulsations. The KLK model predicts that the magnetospheric and spherization radii are similar ($R_\mathrm{m} \sim R_\mathrm{sph}$).

Another interesting information understood from the study of PULXs is the short duration of the spin-up phase that was studied by King, Davies, et al. (2001);

Revnivtsev & Mereghetti (2018), and more recently by Lasota & King (2023). This suggests that PULXs typically function as normal pulsar X-ray binaries for the majority of their lifespan, transitioning into the PULX state during a distinct phase in the evolution of their companions. A potential candidate for such a system could be a Be–X binary that undergoes the transient phase.

1.3 Numerical simulations

1.3.1 Previous works

Over recent years, the numerical modeling of accreting black holes has seen significant improvements, allowing for a more accurate and detailed study of these systems. An important development in the field of numerical simulations of accreting black holes has been the utilization of general relativistic radiative magnetohydrodynamic (GRRMHD) codes (Narayan, Sądowski, et al., 2012; Sądowski, Narayan, et al., 2013; Jiang, Stone, & Davis, 2014; Sądowski, Narayan, et al., 2014; McKinney, Dai, & Avara, 2015; Sądowski & Narayan, 2016; Mishra, Fragile, et al., 2016; Chael, Narayan, & Sądowski, 2017; Lančová, Abarca, et al., 2019).

There are only a few numerical simulations relevant for ULXs with neutron star accretors. Takahashi & Ohsuga (2017) investigated supercritical accretion onto a non-rotating, magnetized neutron star and its implications for ultra-luminous X-ray pulsars. They performed 2.5D radiative GRMHD simulations of accreting ordinary magnetized neutron stars with the dipole magnetic field of strength 10^{10} G, to show that the disc is truncated at approximately three times the neutron star radius. The angular momentum of the disk around the truncation radius is transported inwards through magnetic torque by dipole fields, leading to the spin-up of the neutron star at a rate of $\dot{P} \sim -10^{-11}$. Their results support the hypothesis that PULXs are powered by the supercritical accretion onto ordinary magnetized neutron stars. They also investigated the possibility of supercritical accretion onto a neutron star by comparing it with that of a black hole through 2.5D radiative GRMHD simulations in (Takahashi, Mineshige, & Ohsuga, 2018). Those simulations show that supercritical accretion onto a black hole is feasible due to its ability to swallow excess radiation energy while it is challenging for a neutron star with a surface. However, they found that the radiation force can be self-regulated by balancing with gravity and centrifugal forces, resulting in a significant reduction in the mass accretion rate. The strong radiation pressure-driven outflow around the neutron star forms. These findings provide information about the dynamics of supercritical accretion onto a neutron star and can help in the understanding of high-energy phenomena associated with neutron star accretion.

Abarca, Kluźniak, & Sądowski (2018); Abarca, Parfrey, & Kluźniak (2021), run the 2.5D radiative GRMHD simulations of super-Eddington accretion disks around the black hole, non-magnetized non-rotating neutron star, and magnetized neutron star with the dipole magnetic field of strength 2×10^{10} G. They conducted simulations of accretion onto a neutron star and revealed that the formation of a transition layer in the inner region of the disk results in a larger mass outflow rate and a lower radiative luminosity than that of accretion onto a black hole. It is also found that the total luminosity is about $2.5\,L_{\rm Edd}$. The radiation is strongly directed by the accretion disk outflows thus, the apparent isotropic luminosity, which is reliant on the angle of observation, reaches a peak above $100\,L_{\rm Edd}$, which is consistent with the observed luminosities in ULXs.

Studies have also been conducted on the accretion column of magnetized neutron stars, which may be linked to ultraluminous X-ray emissions. Kawashima, Mineshige, et al. (2016), proposed a model to explain the pulsed emission observed in ULXs. They studied the impact of the neutron star magnetic field on periodic variation of accretion rate. By analyzing the behavior of the accretion flow and the

resulting X-ray spectra, using numerical simulations they found that the proposed model can successfully reproduce the observed pulsation frequency and pulse shape in PULXs. Kawashima & Ohsuga (2020) investigated the effect of general relativity on the propagation of pulsed emission in PULXs. They simulated the behavior of X-ray photons emitted from a pulsar in a strong gravitational field. The results show that general relativistic effects can significantly alter the observed pulse shape and amplitude of the emitted X-rays. The observed pulse fraction was found to be affected by the inclination angle of the observer, with higher inclinations resulting in larger pulse fractions. Overall, the findings of both studies (Kawashima, Mineshige, et al., 2016; Kawashima & Ohsuga, 2020) contribute to our understanding of the physical processes that govern the emission from PULXs.

The study by Zhang, Blaes, & Jiang (2023) presents a 2D axisymmetric radiative relativistic MHD simulation of radiation pressure-supported neutron star accretion columns in split-monopole magnetic fields. They found that the accretion columns exhibit quasi-periodic oscillations with $2 - 10$ kHz peaks and broader extensions to higher frequencies in the luminosity power spectrum.

Due to the increased complexity in developing 3D models of accreting magnetized neutron stars, only a limited number of numerical simulations have been conducted. Romanova, Koldoba, et al. (2021) used 3D simulations to study the effect of tilt angle on the dynamics and structure of the accretion flow onto a magnetized rotating star with a tilted magnetic field. The simulations revealed that the flow patterns around the star strongly depend on the tilt angle of the magnetic axis. The tilt angle has a significant impact on the magnetic field topology of the star, with low tilt angles resulting in mostly axisymmetric fields and high tilt angles leading to highly distorted and complex magnetic fields with multiple magnetic poles and non-axisymmetric structures. The interaction between the accretion flow and the tilted magnetic field was found to generate powerful outflows from the star. Radiation was not implemented in these simulations.

Takasao, Tomida, et al. (2018) performed 3D simulations with `Athena++` code to study accretion onto weakly magnetized stars. They include the effects of radiative cooling, which allows for the formation of a thermally unstable layer in the disk that drives outflows from the disk surface.

Recently, Yang & Li (2023) investigated the long-term evolution of the magnetic field inclination angle of accreting neutron stars in intermediate/low-mass X-ray binaries. They studied the accreting neutron star with a dipole magnetic field that is initially inclined with respect to the rotation axis. They found that the magnetic inclination angle evolves with time due to the accretion of matter onto the neutron star surface. Some neutron stars show significant changes in inclination angle over time (see Yang & Li, 2023, and references therein).

Most recently 3D simulations of neutron star jets were performed by Das & Porth (2024). They have shown that the magnetic field of the neutron star disk plays a crucial role in launching the jet with power proportional to $\Phi^2_{\rm jet}$, where Φ is the open magnetic flux in the jet. They found that the inclination of the neutron star magnetic field impacts the power of the jet. Murguia-Berthier, Parfrey, et al. (2024), studied accretion onto oblique pulsars with 3D GRMHD simulations. They have considered the magnetic field in the accretion disk as well as the tilted magnetic field of neutron stars. The impact of dipole strength and obliquity on the power of neutron star jets is studied.

Although there have been notable numerical simulations of accreting neutron star systems discussed in this section, most of the models are simplified. The dynamic evolution of radiation is usually ignored. Additionally, the magnetic field in the disk interacting with the neutron star dipole and super-Eddington accretion is not fully studied. I include the dynamical evolution of radiation, high accretion rate, neutron star dipole, and loop magnetic field in the torus in my study using the code and numerical methods that are presented in the next section and Chapter 3.

1.3.2 General relativistic radiative magnetohydrodynamic code

Super-Eddington accretion onto a neutron star with a moderate magnetic field entails numerous extreme physical conditions, such as extraordinarily high temperature and luminosity, strong gravitational force, rapid velocity, and intense magnetic field. To accurately conduct numerical simulations of such a system, a robust magnetohydrodynamics (MHD) code that incorporates the equations of general relativity (GR) and an effective radiation transfer scheme is indispensable. General Relativistic Radiative Magnetohydrodynamic (GRRMHD) code `Koral` is suitable for these simulations. The original `Koral` of Dr. Aleksander Sądowski (Sądowski, 2011), is currently maintained by Dr. Andrew Chael (Chael, 2024). Despite being utilized by a limited number of research groups globally, `Koral` has proven its effectiveness as a state-of-the-art tool for conducting advanced simulations of astrophysical phenomena. A significant number of publications using this code studied accretion systems of black holes and neutron stars (Sądowski, 2011; Sądowski, Narayan, et al., 2013; Sądowski, Narayan, et al., 2014; Sądowski, Narayan, et al., 2015; Sądowski & Narayan, 2016; Sądowski & Narayan, 2016; Abarca, Kluźniak, & Sądowski, 2018; Lančová, Abarca, et al., 2019; Abarca, Parfrey, & Kluźniak, 2021; Chatterjee, Chael, et al., 2023; Hallur, Medeiros, & Christian, 2023; Chael, 2024)

Given the extreme conditions inherent in these simulations, it was imperative to execute a standard test problem to examine energy transformation within the MHD simulations. In addition to `Koral`, I utilized the well-known MHD code `Pluto` to compare the results for a test problem for MHD codes, the Orszag-Tang vortex. I investigated energy transfer and reconnection rates in different models of relativistic, non-relativistic, and resistive MHD. I also investigated how the resolution of numerical simulations impacts the final results in both 2D and 3D simulations. I estimated the numerical dissipation in `Pluto` simulations and have found the resolution at which the numerical errors have the least impact on the results. The full study was published in a paper (Kayanikhoo, Čemeljić, et al., 2023b) attached to this thesis as Chapter 2. Part of the resolution study is published in a conference proceedings paper (Kayanikhoo, Čemeljić, et al., 2023a). The MHD equations for each model and a comparison of the codes are provided in detail in Kayanikhoo, Čemeljić, et al. (2023b). In the following subsection, I briefly introduce the `Koral` code, which is used to perform the accreting neutron star simulations presented in this thesis.

1.3.3 Equations

The equations that are solved in `Koral` are as follows (Sądowski, Narayan, et al., 2014):

`Koral` solves the equations of radiative GRMHD which can be expressed in their conservative form,

$$\nabla_\mu(\rho u^\mu) = 0, \tag{1.13}$$

$$\nabla_\mu T^\mu{}_\nu = G_\nu, \tag{1.14}$$

$$\nabla_\mu R^\mu{}_\nu = -G_\nu, \tag{1.15}$$

which can be expressed in two or three dimensions. The gas density in the co-moving fluid frame is denoted by ρ, and u^μ represents the gas four-velocity. The gas stress-energy tensor $T^\mu{}_\nu$ and the radiation stress-energy tensor $R^\mu{}_\nu$ are coupled by the radiation four-force G_ν, making use of electron scattering, bremsstrahlung, and synchrotron opacities as well as photon-conserving Comptonization (Sądowski & Narayan, 2015).

The gas energy-momentum tensor is given as,

$$T^\mu{}_\nu = (\rho + p + u_{int} + b^2)u^\mu u_\nu + (p + b^2/2)\delta^\mu_\nu - b^\mu b_\nu \tag{1.16}$$

which includes the internal energy u_{int}, the pressure p which is given by the ideal gas equation of state, $p = (\gamma - 1)u_{int}$ with adiabatic index γ and the magnetic four-vector b^μ which is defined in terms of the electromagnetic field tensor $F_{\lambda\kappa}$ and Levi-Civita tensor $\epsilon^{\mu\nu\kappa\lambda}$ (Gammie, McKinney, & Tóth, 2003):

$$b^\mu = \frac{1}{2}\epsilon^{\mu\nu\kappa\lambda}u_\nu F_{\lambda\kappa}. \tag{1.17}$$

The magnetic field is evolved using the induction equation as follows,

$$\partial_t(\sqrt{-g}B^i) = -\partial_j\left(\sqrt{-g}(b^j u^i - b^i u^j)\right), \tag{1.18}$$

where B^i is the magnetic three-vector. The magnetic 4-vector is,

$$b^t = B^i u^\mu g_{i\mu}, \tag{1.19}$$

$$b^i = \frac{B^i + b^t u^i}{u^t}, \tag{1.20}$$

where $g_{i\nu}$ is metric.

`Koral` applies a Godunov-type shock-capturing method based on the MUSCL scheme (Komissarov, 1999) to solve equations on a static grid. It offers various reconstruction methods, while time integration employs an implicit-explicit second-order Runge-Kutta scheme to handle the stiff radiation source terms. The numerical implementation is thoroughly explained in Sądowski, Narayan, et al. (2013) and Sądowski & Narayan (2015).

1.3.4 Radiation transfer: $M1$ closure scheme

I already mentioned that the time component of radiation stress-energy tensor is evolved using Eq. 1.15. The scheme that is used in `Koral` to evolve the remaining components of radiation stress-energy tensor (R^{ij}) is called the $M1$ closure scheme (Mihalas & Mihalas, 1984).

The $M1$ scheme assumes that there is a frame, characterized by the four-velocity u^μ_R, where the radiation stress-energy tensor is isotropic. Denoting the energy density in that frame as $\bar{E}$ we have

$$\bar{R}^{\mu\nu} = \bar{E}\, u_R^{\mu}\, u_R^{\nu} + \bar{E} g^{\mu\nu}. \tag{1.21}$$

This closure scheme is a powerful tool that provides treatment of radiation in astrophysical simulations. It is especially useful in modeling accretion discs, where radiation plays a crucial role in the dynamics and energy balance of the system. One of the advantages of the $M1$ closure scheme is its ability to capture the anisotropic nature of radiation and its important radiative effects such as emission, absorption, scattering, and advection.

Moreover, the $M1$ closure scheme allows radiation to propagate along geodesics when in the optically thin regime while facilitating diffusion through the gas when in the optically thick regime. This scheme results in a nearly symmetrical formulation of both the gas and radiation components. The conservation equations are used to describe the microscopic behavior of the gas while the radiative transfer equation depicts the evolution of radiation.

While the $M1$ scheme is approximate when multiple light sources are involved, it is still considered adequate for accretion disc simulations. In many cases, highly anisotropic configurations with multiple beams are not commonly encountered in accretion discs, making this scheme a suitable choice for modeling the dominant radiation source.

1.3.5 Numerical methods

In `Koral` are defined two vectors of primitive, $\boldsymbol{P} = (\rho, u_{\rm int}, v^i, B^i, \bar{E}, v^i_{\rm R})$, and conserved quantities, $\boldsymbol{U} = (\rho u_t, T^t{}_t, T^t{}_i, B^i, R^t{}_t, R^t{}_i)$, (for definitions see Section 1.3.3 and 1.3.4), where the indices are $i = 1, 2, 3$. $v^i = u^i/u^t$, $v^i_{\rm R} = u^i_{\rm R}/u^t_{\rm R}$ are the 3-velocities of gas and radiation rest frame, respectively and $\bar{E}$ is the radiation energy density in the radiation rest frame. The code evolves the conserved quantities. The density, gas and radiation fields are evolved using Eqs. 1.13 to 1.15 and the magnetic field using Eq. 1.18.

A semi-implicit/explicit method is used to evolve the equations forward in time. The explicit step handles the advection and geometric source terms, while the implicit step incorporates the radiative source terms, $\pm\sqrt{-g}G_\nu$. The following steps are used in the code to evolve the quantities (detailed in Abarca, 2022):

- The minmod (Minimum mode) reconstruction is used for primitives. The minmode reconstruction approximates data by retaining the most significant components or modes, reducing complexity while preserving essential features.
- The magnetic fluxes are recomputed using the flux-CT (Flux Constrained Transport) method. The flux-CT method ensures the divergence-free condition.
- The CFL (Courant-Friedrichs-Lewy) condition is used to compute the length of the time step Δt by finding the minimum signal crossing time, $\Delta x_i/a_i$ where a_i is the maximum signal speed and Δx_i is the length both related to the cell i.
- The left and right biased fluxes and conserved quantities are computed from the reconstructed primitives, and the intercell flux is obtained by calculating the left and right moving wave speeds and solving the Riemann problem using the HLL (Harten-Lax-van Leer) Riemann solver.

- The conserved quantities are evolved in time by summing the fluxes and the geometric source terms.
- The cell centered primitives are then recovered using the new conserved quantities using the function defined as $\boldsymbol{U}(\boldsymbol{P})$ (Noble, Gammie, et al., 2006).
- Various constraints, such as floors and ceilings, are applied to the primitive quantities to maintain code stability and prevent the occurrence of unphysical values in quantities e.g. internal energy density, mass-density, and magnetization.
- During the inversion of primitive/conserved quantities, numerical errors are flagged, problem cells are fixed up, and numerical floors are applied.
- In every cell, a comparison is made between the radiative and gas energies to determine which fluid energetically dominates.
- The Newton-Raphson numerical method is used to solve the implicit equations either $T^{t,(n+1)\mu} = T^{t,(n)}{}_{\mu} + G^{(n+1)}{}_{\nu}\,\Delta t$ or $R^{t,(n+1)}{}_{\mu} = R^{t,(n)}{}_{\mu} - G^{(n+1)}{}_{\nu}\,\Delta t$ based on the initial guess in the previous step.
- Second-order Runge-Kutta method (RK2) is used for the time evolution.

At the boundary, the grid cells are extended for a few number of cells, called ghost cells which are not evolved in time. These cells are used to compute the intercell flux at the boundary. These ghost cells are used for the inner boundary on the surface of a neutron star (explained at the end of Section 3.1.2)

Mean-field dynamo

The mean-field magnetic dynamo is a useful tool in `Koral` that allows the axisymmetric 2D accretion disk to run for extended periods.

In axisymmetric ideal MHD systems, there is no dynamo mechanism to regenerate the magnetic field (for the anti-dynamo theorem, see Cowling, 1933). Consequently, the magnetic field decays during simulations, causing the accretion to stop in a short time. However, running simulations in 2D is computationally much cheaper than in 3D. To address this issue, Sądowski, Narayan, et al. (2015) introduced a mean-field dynamo in `Koral`, which compensates for the missing dynamo in 2D simulations and drives the properties of turbulence towards those characteristic of MRI instability in 3D simulations. Mean-field dynamo is tested by comparing 2D and 3D simulations and it accurately approximates the spatial properties of the disk, accretion rate, surface density, and angular momentum (Sądowski, Narayan, et al., 2015).

Chapter 2

Paper 1: Energy distribution and substructure formation in astrophysical MHD simulations

In this chapter, I attach the paper (Kayanikhoo, Čemeljić, et al., 2023b), in which I studied magnetic energy dissipation and structure formation in astrophysical simulations. I performed numerical simulations of a standard Orszag-Tang test problem for MHD codes in different models: ideal MHD in both non-relativistic and relativistic models, resistive non-relativistic MHD model, each in two and three dimensions. The main motivation of this project is to evaluate two high-performance state-of-the-art codes in astrophysics, `Pluto` and `Koral`, by investigating the energy conversion in astrophysical simulations. I estimate the numerical diffusion and have found a good resolution in which the results are physical, with the least impact of numerical error. I also demonstrated that `Koral` excels in capturing substructures in numerical simulations with higher accuracy and exhibits reduced numerical dissipation compared to `Pluto`.

Monthly Notices of the ROYAL ASTRONOMICAL SOCIETY

MNRAS **527,** 10151–10167 (2024) https://doi.org/10.1093/mnras/stad3807
Advance Access publication 2023 December 14

Energy distribution and substructure formation in astrophysical MHD simulations

Fatemeh Kayanikhoo,[1]★ Miljenko Čemeljić,[1,2,3]★ Maciek Wielgus [4,2] and Włodek Kluźniak[1]

[1]*Nicolaus Copernicus Astronomical Center of the Polish Academy of Sciences, Bartycka 18, PL-00-716 Warsaw, Poland*
[2]*Research Centre for Computational Physics and Data Processing, Institute of Physics, Silesian University in Opava, Bezručovo nám. 13, CZ-746 01 Opava, Czech Republic*
[3]*Academia Sinica, Institute of Astronomy and Astrophysics, P.O. Box 23-141, Taipei 106, Taiwan*
[4]*Max-Planck-Institut für Radioastronomie, Auf dem Hügel 69, D-53121 Bonn, Germany*

Accepted 2023 December 7. Received 2023 December 6; in original form 2023 August 23

ABSTRACT

During substructure formation in magnetized astrophysical plasma, dissipation of magnetic energy facilitated by magnetic reconnection affects the system dynamics by heating and accelerating the ejected plasmoids. Numerical simulations are a crucial tool for investigating such systems. In astrophysical simulations, the energy dissipation, reconnection rate, and substructure formation critically depend on the onset of reconnection of numerical or physical origin. In this paper, we hope to assess the reliability of the state-of-the-art numerical codes, PLUTO and KORAL by quantifying and discussing the impact of dimensionality, resolution, and code accuracy on magnetic energy dissipation, reconnection rate, and substructure formation. We quantitatively compare results obtained with relativistic and non-relativistic, resistive and non-resistive, as well as two- and three-dimensional set-ups performing the Orszag–Tang test problem. We find sufficient resolution in each model, for which numerical error is negligible and the resolution does not significantly affect the magnetic energy dissipation and reconnection rate. The non-relativistic simulations show that at sufficient resolution, magnetic and kinetic energies convert to internal energy and heat the plasma. In the relativistic system, energy components undergo mutual conversion during the simulation time, which leads to a substantial increase in magnetic energy at 20 per cent and 90 per cent of the total simulation time of 10 light-crossing times – the magnetic field is amplified by a factor of 5 due to relativistic shocks. We also show that the reconnection rate in all our simulations is higher than 0.1, indicating plasmoid-mediated regime. It is shown that in KORAL simulations more substructures are captured than in PLUTO simulations.

Key words: diffusion – magnetic reconnection – MHD – relativistic processes – methods: numerical – software: simulations.

1 INTRODUCTION

Dissipation processes in astrophysical plasma, including magnetic reconnection (Biskamp 2000), are of fundamental relevance for our understanding of a variety of observed systems, such as solar flares (Giovanelli 1946; Jiang et al. 2021) or magnetic substorms in the Earth's magnetosphere (Akasofu 1968; McPherron 1979). The relative motion in plasmas and gas often leads to the formation of shocks. Non-relativistic magnetized shocks in supernovae remnants are possible sources of acceleration of cosmic rays (Chen & Armstrong 1975; Blandford & Ostriker 1978; Bell 1978; van Marle, Casse & Marcowith 2017). Energy dissipation in the relativistic regime leads to spectacular displays, such as jets and relativistic ejections from the accretion systems around compact objects (Giannios, Uzdensky & Begelman 2009; Ripperda et al. 2022), or event horizon scale synchrotron emission (Mehlhaff et al. 2020) and flaring (Dexter et al. 2020; Wielgus et al. 2022) in the hot advection-dominated accretion flows. In the context of accretion onto compact objects, understanding dissipation occurring on small spatial scales is crucial to finding realistic subgrid physics prescriptions for global simulations.

Magnetic reconnection is a process by which the magnetic field lines in a plasma break and reconnect, releasing stored energy in the form of heat, particles/plasmoid acceleration, or radiation. Reconnection often occurs spontaneously and is usually associated with the presence of a current sheet, a region where the magnetic field lines become almost antiparallel and the plasma conductivity is finite. The magnetic field lines can break and reconnect due to the tearing instability, which is driven by the pressure of the plasma and the tension of the magnetic field (Coppi, Laval & Pellat 1966; Komissarov, Barkov & Lyutikov 2007; Del Zanna et al. 2016). Spontaneous reconnection is relatively slow, and the rate is determined by the local plasma conditions (Sweet 1958; Baty 2000). Petschek proposed a shock geometry that allows fast magnetic reconnection to occur (Petschek 1964), this may be realized in magnetohydrodynamic (MHD) simulations for large values of (anomalous) resistivity. In systems with strongly magnetized plasma, Lazarian & Vishniac (1999) state that reconnection will always occur at some upper limit of the reconnection rate. Another

★ E-mail: fatima@camk.edu.pl (FK); miki@camk.edu.pl (MC)

scenario is the forced magnetic reconnection, which occurs due to external perturbation in a turbulent system (Vekstein & Jain 1998; Potter, Browning, & Gordovskyy 2019; Srivastava et al. 2019). In this scenario, the reconnection rate can be much faster than spontaneous reconnection, as the external forces can overcome the moderating resistances of the plasma. Such turbulent systems can be found in various environments, such as solar wind, the interstellar medium, or the accretion discs around black holes and neutron stars.

In this work, we study energy dissipation and magnetic reconnection in the MHD framework, using a simple example of a vortical system, the Orszag–Tang (OT) vortex (Orszag & Tang 1979), a popular test problem for numerical MHD codes. In such a system, the magnetic field lines stretch and twist thus facilitating the reconnection process. This test has already been performed with state-of-the-art codes like ATHENA++ (White, Stone & Gammie 2016), BHAC (Olivares Sánchez, Porth & Mizuno 2018), and HARM (Gammie, McKinney & Toth 2003). Here, we implement the OT test in two more state-of-the-art codes used in numerical simulations of accretion. We quantitatively compare results obtained with the two codes of our choice at different resolutions and set-ups in relativistic/non-relativistic, resistive/non-resistive, and two-dimensional (2D) versus three-dimensional (3D) configurations, to study how much these different aspects impact the obtained results, characterized by the energy balance and reconnection rate.

The well-established codes we selected for the comparison are the widely used, public PLUTO code (Mignone et al. 2007) and the radiative, general relativistic code KORAL (Sądowski et al. 2013, 2014a).

PLUTO has extensively been used in simulations of magnetospheric star–disc interaction with alpha-viscous disc in Zanni & Ferreira (2009) and Čemeljić (2019), with magnetorotational instability including alpha-dynamo in Flock et al. (2011), jet launching discs in Tzeferacos et al. (2009), accretion-ejection problem in Stepanovs & Fendt (2014), to mention only some. It was also used in the simulations of star–planet magnetospheric interaction, e.g. in Strugarek et al. (2014) and Varela et al. (2018) and related papers. A radiative module was included in simulations of accretion columns in classical T Tauri stars in Colombo et al. (2019). KORAL code is used to study the accreting compact objects in general relativity involving radiation using M1 closure scheme (Sądowski et al. 2013). The code has been used to study the radiative black hole accretion discs (Sądowski et al. 2014b; Sądowski et al. 2017; Chael, Narayan & Johnson 2019; Lančová et al. 2019) as well as super-Eddington accretion on to magnetized neutron stars (Abarca, Parfrey & Kluzniak 2021).

The paper is organized as follows. In Section 2, we review the theoretical framework, including the formalism of the MHD equations. The initial conditions in the OT problem in 2D and 3D set-ups are given in Section 3. In Section 4, we discuss the results in different cases. The reconnection rate is studied in Section 5. In Section 6, we present the direct comparison of the results in the two codes we used here and we conclude in Section 7.

2 SPECIAL RELATIVISTIC RESISTIVE MHD EQUATIONS

We investigate the energy distribution in astrophysical simulations in the following set-ups:

(i) Ideal non-relativistic magnetohydrodynamics (Ideal-MHD).
(ii) Ideal relativistic MHD (Rel-MHD).
(iii) Resistive non-relativistic MHD (Res-MHD).

We begin with presenting the resistive special relativistic MHD equations in Minkowski spacetime, which we then simplify to relativistic ideal MHD and non-relativistic resistive MHD cases. The simulations are performed in the PLUTO and KORAL codes, with the exception of Res-MHD, which is performed in PLUTO alone (KORAL only treats non-resistive MHD equations).

The dynamics of magnetic fluids can be described using the equations of conservation of mass, momentum, and energy, as well as the Maxwell–Faraday, Ampère–Maxwell, and Ohm equations. For a fluid propagating in the laboratory reference frame with bulk velocity $\boldsymbol{v} = \boldsymbol{\beta} c$, the Lorentz factor is defined as $\Gamma = (1 - \beta^2)^{-1/2}$, and the fluid four-velocity is $\boldsymbol{u} = (\Gamma c, \Gamma \boldsymbol{v})$. We denote fluid rest-mass density in the fluid frame by ρc^2, fluid pressure by p, fluid internal energy density in the fluid frame by $U_{\rm int}$, electric field by $\boldsymbol{E}$, and magnetic field by $\boldsymbol{B}$. The $\boldsymbol{E}$ and $\boldsymbol{B}$ fields were redefined to absorb a factor of $1/\sqrt{4\pi}$ each, so that factors of $1/(4\pi)$ do not appear in relations such as equations (2), (3), and (7). Furthermore, we define enthalpy density in the fluid frame,

$$\omega = \rho c^2 + U_{\rm int} + p \,, \tag{1}$$

momentum density

$$\boldsymbol{m} = \omega \Gamma^2 \boldsymbol{v} + c \boldsymbol{E} \times \boldsymbol{B} \,, \tag{2}$$

and the total energy density ε

$$\varepsilon = \omega \Gamma^2 - p + \frac{1}{2}(E^2 + B^2) \,. \tag{3}$$

The conservation equations are then

$$\frac{\partial(\Gamma\rho)}{\partial t} + \nabla \cdot (\Gamma \rho \boldsymbol{v}) = 0, \tag{4}$$

$$\frac{\partial \boldsymbol{m}}{\partial t} + \nabla \cdot \left[\omega \Gamma^2 \boldsymbol{v}\boldsymbol{v} + c^2 (p \boldsymbol{I} + \boldsymbol{T}_{EM})\right] = 0, \tag{5}$$

$$\frac{\partial \varepsilon}{\partial t} + \nabla \cdot (\omega \Gamma^2 \boldsymbol{v} + c\, \boldsymbol{E} \times \boldsymbol{B}) = 0, \tag{6}$$

where additionally we denote identity matrix with $\boldsymbol{I}$, and the electromagnetic stress tensor with $\boldsymbol{T}_{EM}$, hence

$$\boldsymbol{T}_{EM} = \frac{1}{2}(E^2 + B^2)\boldsymbol{I} - (\boldsymbol{E}\boldsymbol{E} + \boldsymbol{B}\boldsymbol{B}) \,. \tag{7}$$

The Maxwell–Faraday and Ampère–Maxwell equations are

$$\frac{1}{c}\frac{\partial \boldsymbol{B}}{\partial t} + \nabla \times \boldsymbol{E} = 0, \tag{8}$$

$$\frac{1}{c}\frac{\partial \boldsymbol{E}}{\partial t} - \nabla \times \boldsymbol{B} = -\boldsymbol{J}/c, \tag{9}$$

respectively, where $\boldsymbol{J}$ is the current density that comes from Ohm's law,

$$\boldsymbol{J} = (\Gamma c^2/\eta)(\boldsymbol{E} + \boldsymbol{\beta} \times \boldsymbol{B}), \tag{10}$$

where η is the magnetic diffusivity, which is identical to resistivity. The additional condition $\nabla \cdot \boldsymbol{B} = 0$ from Gauss's law is enforced during the numerical evolution of the magnetic field.

In order to obtain the system of non-relativistic resistive MHD equations from equations (4) to (6), we make a number of approximations based on $\beta \ll 1$ and $p + U_{\rm int} \ll \rho$ assumptions, leading to a following formulation:

$$\frac{\partial \rho}{\partial t} + \nabla \cdot (\rho \boldsymbol{v}) = 0, \tag{11}$$

$$\frac{\partial \rho \boldsymbol{v}}{\partial t} + \nabla \cdot (\rho \boldsymbol{v}\boldsymbol{v} + p\boldsymbol{I} + \boldsymbol{T}_{EM}) = 0, \tag{12}$$

$$\frac{\partial \varepsilon}{\partial t} + \nabla \cdot \left[\left(\omega + \rho \frac{\upsilon^2}{2} \right) \boldsymbol{\upsilon} + c\boldsymbol{E} \times \boldsymbol{B} \right] = 0, \tag{13}$$

where the non-relativistic total energy and enthalpy densities are

$$\varepsilon = U_{\rm int} + \rho \frac{\upsilon^2}{2} + \frac{1}{2}(E^2 + B^2)\,, \tag{14}$$

$$\omega = U_{\rm int} + p\,. \tag{15}$$

Additionally, Ohm's law in resistive non-relativistic MHD becomes

$$\boldsymbol{J} = \frac{c^2}{\eta}(\boldsymbol{E} + \boldsymbol{\beta} \times \boldsymbol{B}) = c\nabla \times \boldsymbol{B}\,, \tag{16}$$

neglecting the displacement currents ($\partial \boldsymbol{E}/\partial t = 0$) in equation (9) to obtain the second equality.

The diffusive time-scale, $\tau_\eta = L^2/\eta$ (in conventional units, if η is in cm^2 s^{-1} and L is in cm, then τ_η is in seconds) can be compared with the dynamical time-scale $\tau_\upsilon = L/\upsilon$, where L is the characteristic length-scale of the system and υ is the characteristic velocity scale. The ratio of the two time-scales is known as the magnetic Reynolds number

$$R_{\rm m} = \frac{\tau_\eta}{\tau_\upsilon} = \frac{\upsilon L}{\eta}\,. \tag{17}$$

When the typical velocity scale of the system is the Alfvén velocity $\upsilon_{\rm A} = B/\sqrt{4\pi\rho}$, this ratio is called the Lundquist number

$$S = \upsilon_A L/\eta. \tag{18}$$

Astrophysical systems often satisfy the condition $S \gg 1$, which is equivalent to $L \gg \eta/\upsilon_A$. In such cases, for either relativistic or non-relativistic cases, we can use the ideal MHD approximation

$$\boldsymbol{E} = \boldsymbol{B} \times \boldsymbol{\beta}. \tag{19}$$

As a consequence, $\boldsymbol{E}$ can be readily evaluated and does not need to be evolved with the Ampère-Maxwell equation (equation 9), simplifying the Maxwell-Faraday equation (equation 8) for the $\boldsymbol{B}$ field evolution to

$$\frac{1}{c}\frac{\partial \boldsymbol{B}}{\partial t} + \nabla \times (\boldsymbol{B} \times \boldsymbol{\beta}) = 0\,. \tag{20}$$

3 ORSZAG–TANG TEST PROBLEM

With implicit inclusion of the most important features of MHD turbulent flow such as energy dissipation and magnetic reconnection (Orszag & Tang 1979; Dahlburg & Picone 1989) the Orszag–Tang vortex is a comprehensive test problem for MHD codes. This problem mostly tests the code performance in simulations with MHD shocks and shock–shock interactions.

We study the energy distribution in different set-ups by performing the OT test problem simulations using two astrophysical simulation codes: PLUTO (version 4.4; Mignone et al. 2007) and KORAL (Sądowski et al. 2014a). The description of our simulations is mostly presented in code units. These are obtained by scaling the equations with fiducial values of certain physical quantities. All velocities are scaled with $\upsilon_0 = c$, e.g. the statement that $\upsilon_{\rm A} = 1$ in code units signifies that the Alfvén velocity is equal to the speed of light. The density is scaled with some density ρ_0, the pressure with p_0, and the electromagnetic fields with B_0. The exact value of ρ_0 is immaterial, as long as $p_0 = \rho_0 \upsilon_0^2$ and $B_0 = \upsilon_0\sqrt{4\pi\rho_0}$.

3.1 Two-dimensional set-up

The simulation is set up in a 2D computational box $0 \le x, y \le 2\pi$ with periodic boundary conditions and the following initial conditions for velocity and magnetic fields (Ripperda, Bacchini & Philippov 2020):

$$v = \tilde{v}(-\sin y, \sin x, 0), \tag{21}$$

$$B = \tilde{B}(-\sin y, \sin 2x, 0). \tag{22}$$

We adopt $\tilde{v} = 0.99\upsilon_0/\sqrt{2}$ and $\tilde{B} = B_0$. The initial density is uniform.

In 2D, we perform the OT simulations in the range of uniform resolutions from 64^2 to 4096^2 in different set-ups (Ideal-MHD, Res-MHD, and Rel-MHD), doubling the number of grid points in each dimension to increase the resolution step by step. In 3D, we run the Ideal-MHD and Rel-MHD simulations in three resolutions 128^3, 256^3, and 512^3. Only with PLUTO, we run the Res-MHD simulation (in both 2D and 3D) in the resolution 512^3. Without resistivity, both PLUTO and KORAL are used for Ideal-MHD and Rel-MHD simulations in 2D and 3D set-ups.[1]

All simulations run to the final time $t = 10\,t_c$, where t_c is the light-crossing time across the typical length in the system. In code units, $t_c = L$, and we take $t_c = 1$.

3.2 Three-dimensional set-up

In order to study the difference between 2D and 3D MHD flows and reconnection, we extend the Orszag–Tang test problem to three dimensions. We set up the simulation in a cubic computational box $0 \le (x, y, z) \le 2\pi$ with periodic boundary conditions.

For the Rel-MHD simulations, the initial equations are chosen in such a way as to result in a realistic turbulent system, following the definition of a Taylor–Green vortex (Orszag & Tang 1979):

$$v = \tilde{v}(\cos z \sin y \cos z, -\sin x \cos y \cos z, 0), \tag{23}$$

$$B = \tilde{B}(-\sin y, \sin 2x, 0), \tag{24}$$

where $\tilde{v}$ and $\tilde{B}$ are the same as in the 2D set-up.

We find that such initial conditions do not result in a sufficiently turbulent outcome in non-relativistic simulations in 3D, so for Ideal-MHD and Res-MHD simulations in 3D we use different initial conditions, following Mininni, Pouquet & Montgomery (2006):

$$v = \tilde{v}(-\sin y, \sin x, 0), \tag{25}$$

$$B = \tilde{B}(-2\sin 2y + \sin z, 2\sin x + \sin z, \sin x + \sin y), \tag{26}$$

where $\tilde{v} = 2v_0$ and $\tilde{B} = 0.8B_0$. The initial density is uniform.

4 ENERGY COMPONENTS IN THE RESULTS

We study the dissipation of magnetic energy and investigate the conversion of energy by following the time evolution of the energy components: the electromagnetic energy density $U_{\rm EB} = E_{\rm B} + E_{\rm E} = \frac{1}{2}(B^2 + E^2)$, the kinetic energy density $E_{\rm K}$, and internal energy density $U_{\rm int}$. We study all components in the laboratory frame, thus the kinetic energy and internal energy densities in the relativistic simulations Rel-MHD are computed as follows:

$$E_{\rm K} = \rho(\Gamma^2 - 1)c^2, \tag{27}$$

[1]The physical resistivity module is publicly available only in non-relativistic PLUTO, and this is the one we use to perform our Res-MHD simulations.

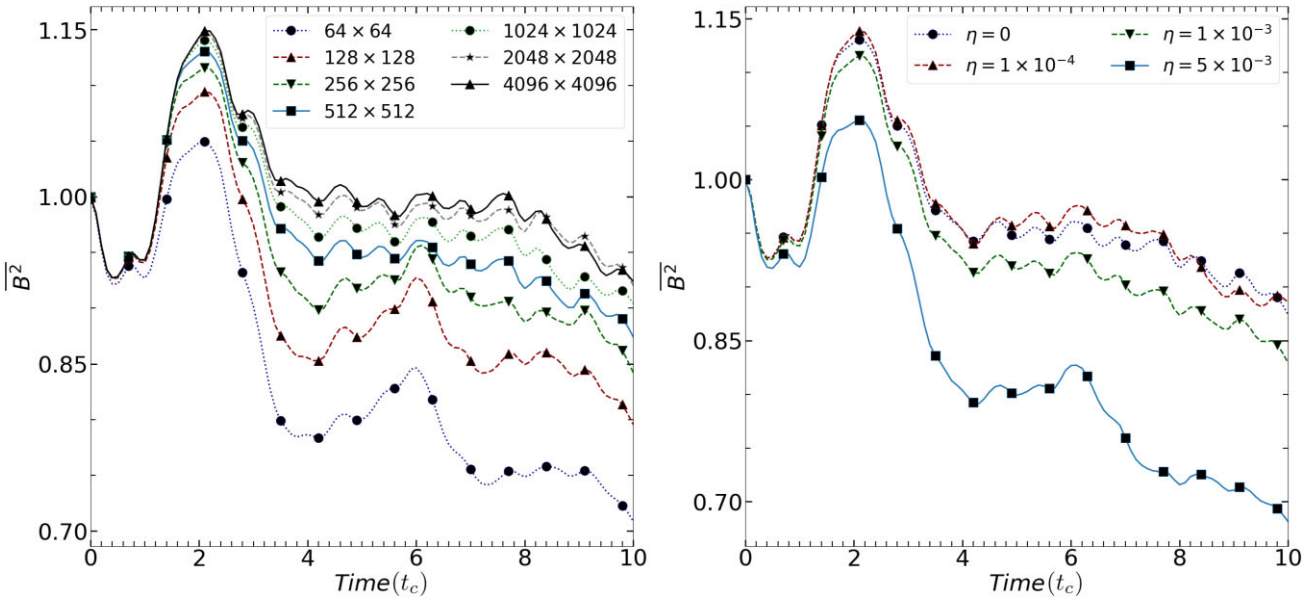

Figure 1. The time evolution of $\overline{B^2}$ in PLUTO simulations: The Ideal-MHD case with different resolutions (*left panel*), and Res-MHD case with different physical resistivities η for the resolution of 512^2 (*right panel*). The unit of time is $t_c = L/c$.

$$U_{\rm int} = \left(\frac{\gamma}{\gamma - 1}\Gamma^2 - 1\right) p. \tag{28}$$

Here, $\gamma = 4/3$ is the polytropic constant. In the non-relativistic limit (simulations Ideal-MHD and Res-MHD), the internal energy density becomes

$$U_{\rm int} = \frac{p}{\gamma - 1}, \tag{29}$$

while the kinetic energy density is

$$E_{\rm K} = \frac{1}{2}\rho\upsilon^2, \tag{30}$$

as can be seen from equations (13) and (14). Another quantity that is a function of space and time is the magnetization defined as $\sigma = B^2/(\rho c^2)$.

We discuss and compare the averaged energy densities denoted by a bar and computed in 3D through

$$\overline{Q} = \frac{\iiint_V Q \, {\rm d}x \, {\rm d}y \, {\rm d}z}{\iiint_V {\rm d}x \, {\rm d}y \, {\rm d}z}, \tag{31}$$

where V is the volume of the simulation box. In 2D, the corresponding formula is

$$\overline{Q} = \frac{\iint_S Q \, {\rm d}x \, {\rm d}y}{\iint_S {\rm d}x \, {\rm d}y}. \tag{32}$$

The results in PLUTO and KORAL simulations are very similar both qualitatively and quantitatively. Unless stated otherwise, we present the PLUTO results. The KORAL results and details of their difference from the PLUTO results are discussed in detail in Section 6.

4.1 Ideal-MHD and Res-MHD simulations

In this section, we estimate the numerical dissipation in the simulations and study the effect of resistivity on the evolution of the system. In the left panel of Fig. 1, we plot the time evolution of the averaged squared magnetic field $\overline{B^2}$ measured in Ideal-MHD simulations for different resolutions. It is clear that at later times the value of $\overline{B^2}$ increases with an increase in the resolution. This is because in grid-based codes the flux is computed over the surface of every grid cell. In such a calculation, there is some amount of computational dissipation, so-called numerical resistivity. Before we study the effect of physical resistivity in simulations, it is important to estimate the numerical dissipation at each resolution and find a reasonable minimal resolution.

We compare the results in non-resistive Ideal-MHD simulations with the Res-MHD simulations set with different physical resistivities (η in equation 16), at each resolution.[2] In the right panel of Fig. 1, the results obtained with the resolution 512^2 are shown. We compare $\overline{B^2}$ of the simulations with $\eta = 0, 10^{-4}, 10^{-3}, 5 \times 10^{-3}$. The curves corresponding to the Ideal-MHD and Res-MHD simulations with $\eta = 10^{-4}$ are almost overlapping, so at this resolution we estimate the numerical resistivity to be below 10^{-4} and conclude that the resolutions higher than 512^2 are reasonably reliable for our simulations with the PLUTO code.

The magnetic energy initially increases and then decreases, forming the hump at $2t_c$ in its plot (Fig. 1). This is caused by the compression of a region around a current sheet and subsequent formation of a reconnection layer (at $t \approx 2t_c$) which then dissipates the magnetic field energy.

In Fig. 2, we show the mass-density plots at $t = 2.5t_c$ in the simulations Ideal-MHD (numerical resistivity below 10^{-4}) and Res-MHD (physical resistivity $\eta = 10^{-4}$) for the resolution of

[2]With a different set-up in PLUTO, Čemeljić, Vlahakis & Tsinganos (2014) found that for the numerical resistivity to decrease by an order of magnitude, the number of grid cells should be quadrupled, as also follows from the estimate with the characteristic length and diffusive timescale, $\eta = L^2/t_\eta$.

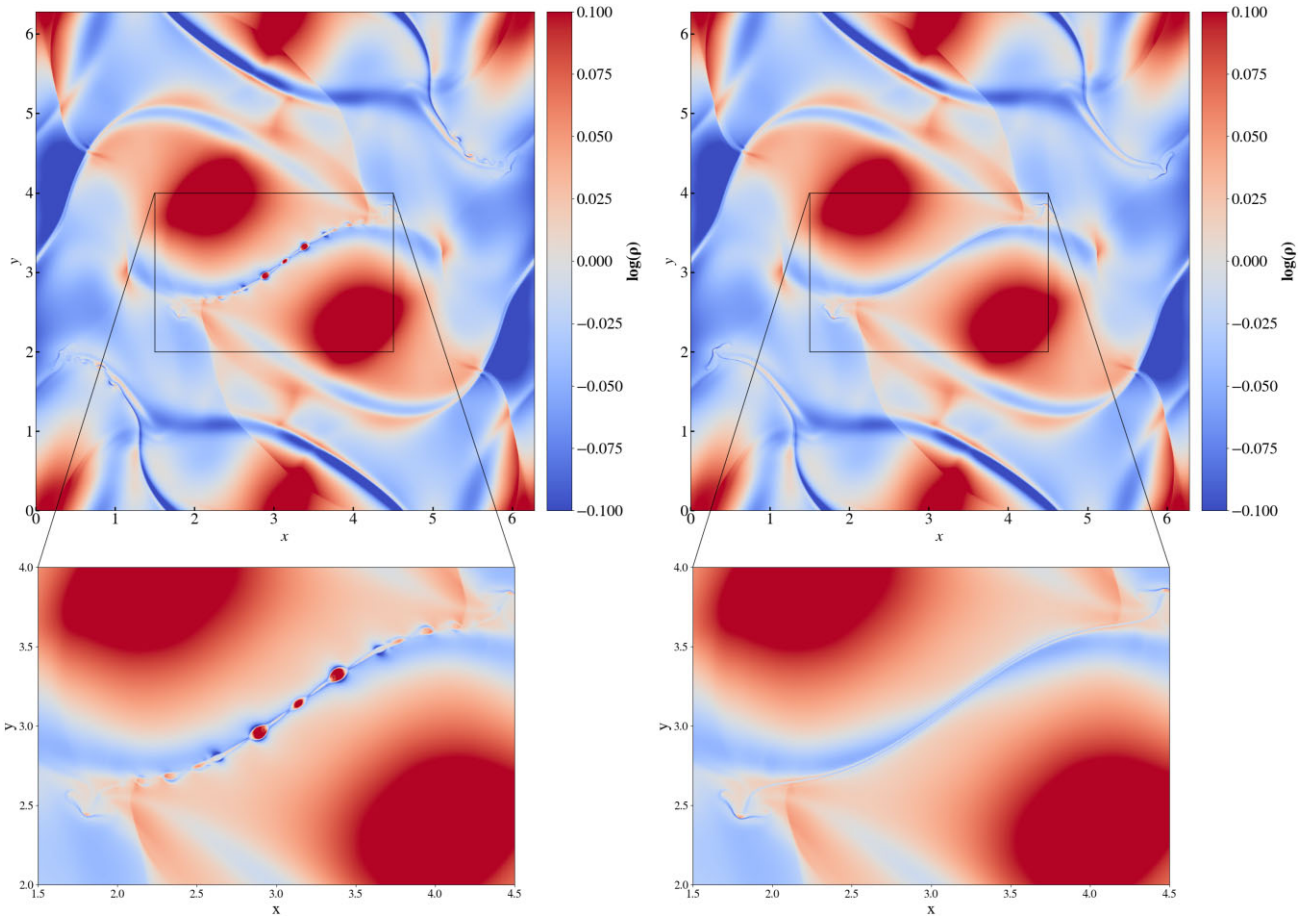

Figure 2. The rest mass density at $t = 2.5t_c$ in the resolution of 4096^2 with PLUTO in the Ideal-MHD simulations (*left panels*) and Res-MHD simulations with physical resistivity $\eta = 10^{-4}$ (*right panels*). Plasmoids, zoomed-in in the bottom panels, form only in a case with sufficiently low resistivity, corresponding to a Lundquist number larger than $S \sim 10^4$.

4096^2. In the left panel (Ideal-MHD), we have identified plasmoids (regions of higher density and lower magnetization relative to their surroundings), these are the substructures located in the central region of the simulation box. In the right panel (Res-MHD), the chain of plasmoids does not appear. Similarly, we see no such chain in the simulations with a resistivity larger than 10^{-4}. The resistivity of 10^{-4} corresponds to the Lundquist number $S = Lv_A/\eta \approx 10^4$, with the typical length-scale of the system $L \approx 1$ and Alfvén velocity $v_A \approx 1$. This result matches theoretical studies which confirm that the current sheet is plasmoid unstable[3] at $S > 10^4$ (Loureiro, Schekochihin & Cowley 2007; Ripperda, Bacchini & Philippov 2020). We also confirm that with a smaller physical resistivity ($\eta < 10^{-5}$, $S > 10^5$) some substructures are resolved in the Res-MHD simulations.

We compare the different terms in energy distribution (magnetic energy $\overline{E_B}$, kinetic energy $\overline{E_K}$, internal energy $\overline{U_{\rm int}}$, and electric energy $\overline{E_E}$, respectively) in the Res-MHD simulations with $\eta = 5 \times 10^{-3}$ and $\eta = 10^{-4}$ (Fig. 3). The first row of this figure shows magnetic energy where the horizontal dashed line, located at $\overline{E_B} = 0.5$, shows the initial value of magnetic energy. We see that with decreasing physical resistivity (from the left panel to the right panel) the rate of magnetic energy decrease becomes smaller. The dissipated magnetic energy converts to the internal energy and heats up plasma as shown in the third row of this plot. We will discuss the energy components in Rel-MHD and Ideal-MHD simulations in the next section.

[3]Plasmoid unstable current sheet involves a dynamic process where plasmoids merge and split within a sheet-like structure of magnetized plasma.

4.2 Ideal-MHD and Rel-MHD simulations

We compare the results of non-relativistic (Ideal-MHD) and relativistic (Rel-MHD) non-resistive MHD simulations in the PLUTO code. The different terms in energy distribution (magnetic energy $\overline{E_B}$, kinetic energy $\overline{E_K}$, internal energy $\overline{U_{\rm int}}$, and electric energy $\overline{E_E}$, respectively) are shown in Fig. 4. Panels in the left column show the results for Rel-MHD and in the right column for Ideal-MHD.

The magnetic energy evolution, shown in the first row of panels in Fig. 4, indicates that in simulation Rel-MHD the magnetic energy increases fivefold from the initial value of 0.5 (shown by the black dashed line in both left and right top panels). In the non-relativistic simulation Ideal-MHD, there is only a minor initial increase of the magnetic energy followed by a slow decay.

The kinetic energy evolution is presented in the second row of Fig. 4, where a black dashed line is also drawn for reference at the value of 0.5. The kinetic energies were computed using equations (27) and (30) for the Rel-MHD and Ideal-MHD simulations,

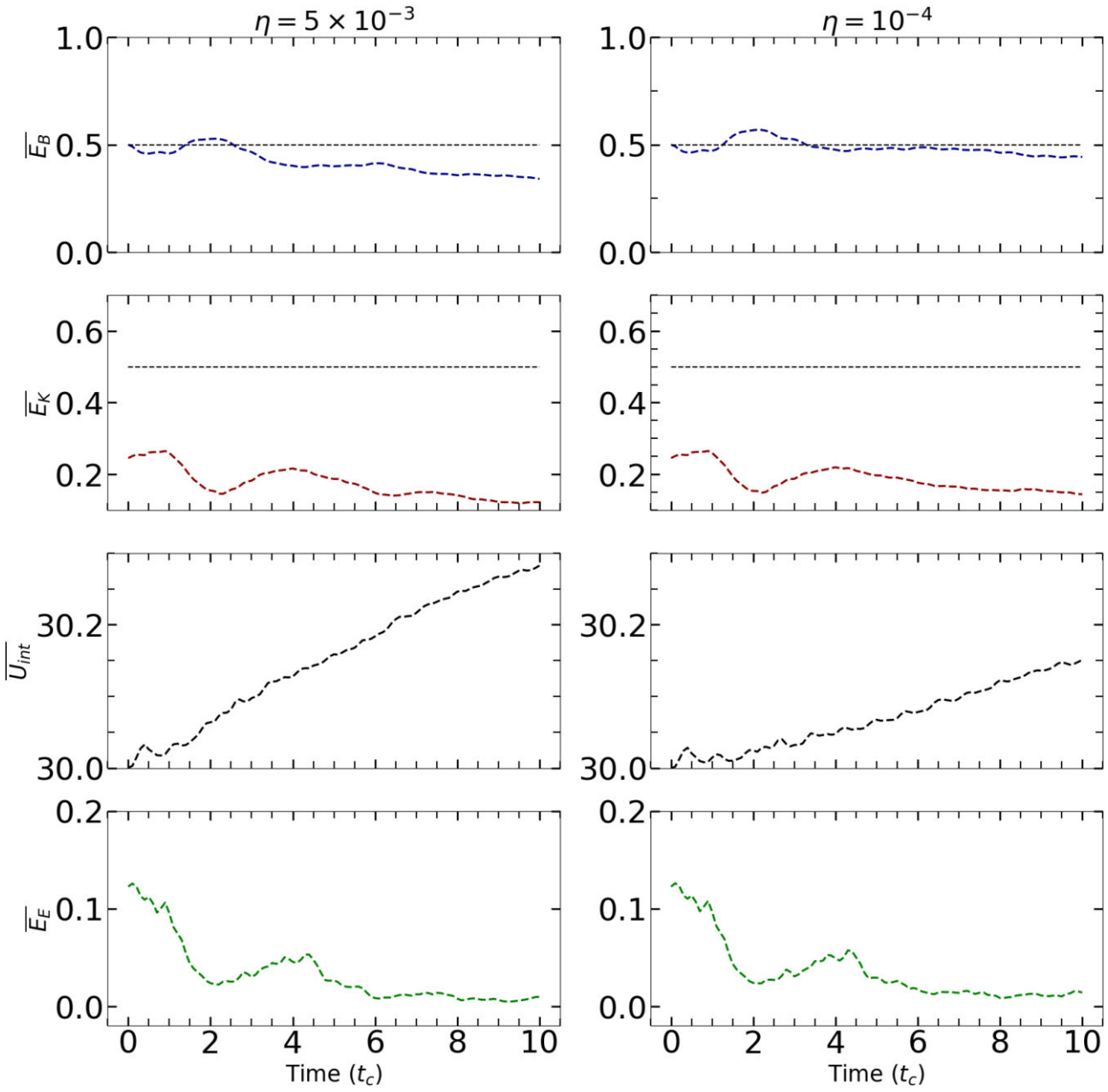

Figure 3. Energy distribution in Res-MHD simulations with physical resistivities $\eta = 5 \times 10^{-3}$ (*left panels*) and $\eta = 10^{-4}$ (*right panels*) at the resolution of 512^2 grid cells. The horizontal black dashed lines in the $\overline{E_B}$ and $\overline{E_K}$ panels indicate the initial value (0.5) of the magnetic energy $\overline{E_B}$ (see the detailed discussion in Section 4.1). The dissipated magnetic energy heats up the plasma.

respectively. In Rel-MHD, the effect of the Lorentz factor on the kinetic energy leads to an initial value of approximately 0.62, which is higher than the magnetic energy. In contrast, for the Ideal-MHD simulations, the initial value of the kinetic energy is approximately 0.25, half the value of the magnetic energy. Initially, in Rel-MHD the kinetic energy amplifies the magnetic field, while in the non-relativistic Ideal-MHD case the low value of $\overline{E_K}$ is not enough to amplify the magnetic energy. Thus, in Rel-MHD the effect of kinetic energy on the magnetic energy evolution in the second half of the simulation is significant, causing a secondary increase of $\overline{E_B}$. In the Ideal-MHD, no such effect is observed.

In the third row of panels in Fig. 4, we show the internal energy as computed from equations (28) and (29). Comparison with the first row of panels shows the conversion between magnetic energy and internal energy.

In Rel-MHD, after $t \simeq 5t_c$, the large amount of the internal and kinetic energy amplifies the magnetic field. This is visible as the second increase ('hump') in the $\overline{E_B}$ curve. Such an outcome in the Rel-MHD simulation offers an explanation for the energy reservoir in magnetized systems like relativistic jets in active galactic nuclei, accretion discs of black holes, and magnetized neutron stars in high-energy astrophysics. In the non-relativistic Ideal-MHD case, shown in the right panel, the released magnetic energy converts to internal energy and heats up the plasma. In contrast with the relativistic case, the amount of energy in the system is not enough to re-amplify the magnetic field.

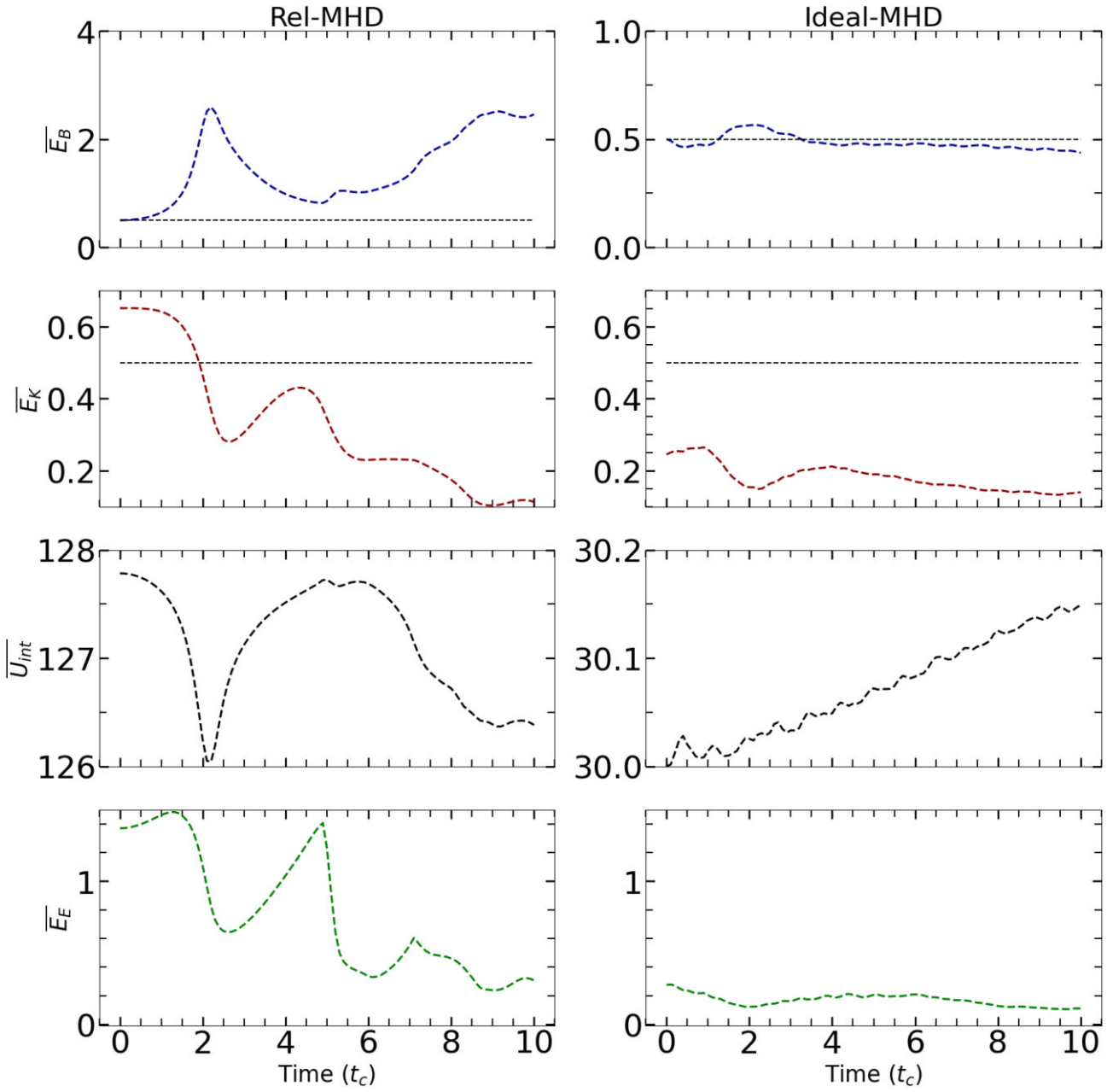

Figure 4. Energy distribution in Rel-MHD and Ideal-MHD PLUTO simulations at the resolution of 512^2 grid cells are shown in the (*left*) and (*right*) panels, respectively. The horizontal black dashed lines in the panels with $\overline{E_B}$ and $\overline{E_K}$ indicate the initial value of the magnetic energy $\overline{E_B} = 0.5$. See the detailed discussion in Section 4.2.

The final row of panels in Fig. 4 displays the electric energy, which exhibits a significant evolution in the Rel-MHD simulation. The electric field is a function of magnetic field and velocity (equation 19). Consequently, when the magnetic field is increased around $\sim 2t_c$, the electric energy $\overline{E_E}$ also increases. Furthermore, as the system evolves, there is another subsequent increase in $\overline{E_E}$, coinciding with an increase in kinetic energy after $4t_c$.

The sum of all energy components in each of the simulations is conserved over time, as shown in Fig. 5. The residuals in the total energy, $\overline{|E_{\rm resid}(t)|} = |E_{\rm tot}(t) - E_{\rm tot}(0)|/E_{\rm tot}(0)$, are displayed for the simulations Ideal-MHD, Res-MHD (with $\eta = 5 \times 10^{-3}$), and Rel-MHD. Here, $E_{\rm tot}$ is the sum of the magnetic, electric, kinetic, and internal energies displayed in Fig. 5. The residuals in the Ideal-MHD and Res-MHD in PLUTO simulation are $\approx 3 \times 10^{-3}$, in KORAL Rel-MHD $\sim 10^{-4}$, whereas, in the Rel-MHD case in PLUTO they are $\approx 10^{-9}$. This indicates that the numerical dissipation in the relativistic simulation is significantly lower than in the non-relativistic simulations. Also, the results indicate that Rel-MHD simulation in PLUTO is less dissipative than in KORAL.

Space averaged magnetization in both simulations, Rel-MHD and Ideal-MHD, with the fixed resolution of 512^2 grid cells, is shown as a function of time in Fig. 6. This shows once again how the relativistic system is strongly magnetized and the magnetization increases by the end of the simulation time, while in a non-relativistic simulation, the magnetization does not evolve significantly.

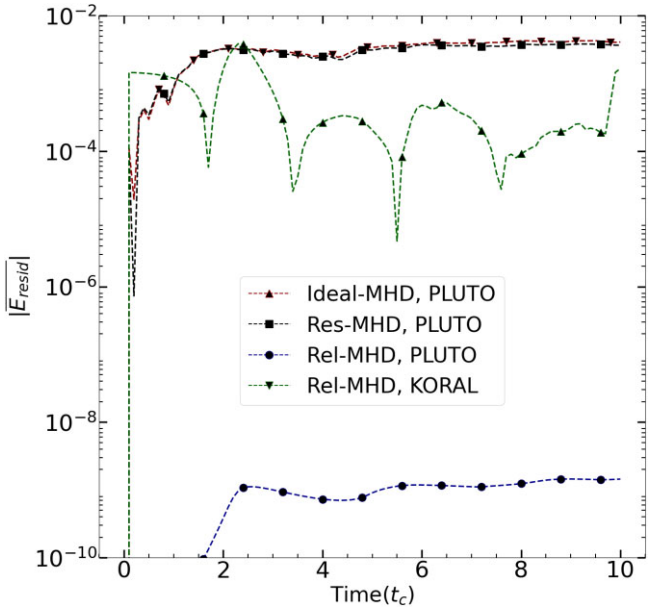

Figure 5. Residuals of total energy $\overline{|E_{\rm resid}|} = |E_{\rm tot}(t) - E_{\rm tot}(0)|/E_{\rm tot}(0)$ in the Ideal-MHD and Res-MHD ($\eta = 5 \times 10^{-3}$) simulations with PLUTO (top two, nearly coinciding curves) and Rel-MHD simulations with PLUTO (bottom curve) and KORAL, with the resolution 512^2 grid cells. The conservation of energy is significantly more accurate in the Rel-MHD simulation, particularly in PLUTO.

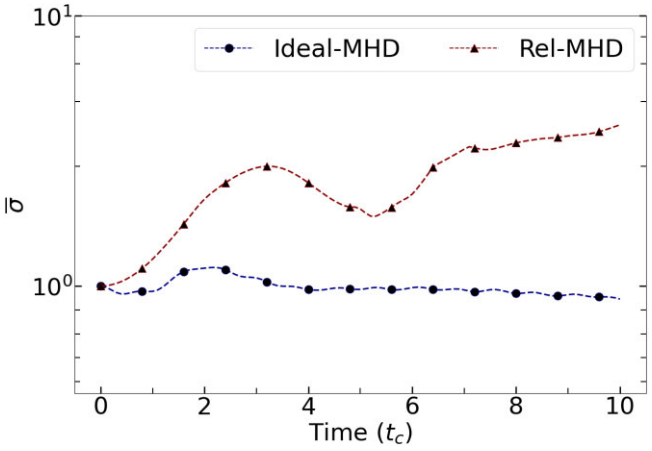

Figure 6. Magnetization ($\sigma = B^2/\rho$ in code units) in Ideal-MHD and Rel-MHD simulations with PLUTO at the resolution 512^2 grid cells.

4.3 3D simulations

We perform the OT test problem simulations in three dimensions in PLUTO and KORAL with the initial conditions of equations (23) and (24) in Rel-MHD simulations and with the initial conditions of equations (25) and (26) in Ideal-MHD and Res-MHD simulations.

The time evolution of $\overline{B^2}$ in the Ideal-MHD simulations is shown in the left panel of Fig. 7. We expect the current sheet to be resolved at time $t \simeq 1.5t_c$, because of the increase in magnetic energy discussed in the previous section. We search for the reconnection layers and plasmoids in different slices of the simulation domain at this simulation time. An example of a resulting rest-mass density plot is shown in Fig. 8, which is a slice at $z = \pi/2$. The plasmoid (in the left panel) is shown at the center of the simulation box, which is zoomed-in at the bottom panel.

We estimate the numerical resistivity at each resolution in Ideal-MHD simulations in 3D by comparing with Res-MHD simulations for different values of η. The plot of $\overline{B^2}$ with different physical resistivities $\eta = 0$, 10^{-4}, 10^{-3}, 5×10^{-3}, in the resolution of 512^3 grid cells is shown in Fig. 9 (the method is discussed in Section 4.1). It is shown that the curves corresponding to $\eta = 10^{-4}$ resistive simulations and the non-resistive Ideal-MHD cases are convergent, so the numerical resistivity in Ideal-MHD simulations with PLUTO at the given resolution is estimated to be $\lesssim 10^{-4}$. We expect that at this resolution the current sheets are well resolved.

The rest-mass density plots in the Ideal-MHD simulations (left panel) and resistive Res-MHD simulations with $\eta = 10^{-3}$ (right panel) with the resolution of 512^3 are shown in Fig. 8. The zoomed-in frames in the bottom panels show the substructure at the centre of each simulation box. From the configuration of the magnetic field which is not shown in this figure, we found that there is a thick current sheet containing a plasmoid in the Ideal-MHD simulation, which is not resolved in the Res-MHD simulation.

The right panel in Fig. 7 shows the time evolution of $\overline{B^2}$ in the Rel-MHD simulation. It shows that $\overline{B^2}$ increases to the time $t \simeq 7t_c$. At the low resolutions, the magnetic energy drops after this time, but at the high resolution 512^3, the peak is flattened. We found that at the smaller resolutions, due to the high numerical dissipation, the current sheets are compressed and plasmoids are not resolved. At the high resolution 512^3, we can see the plasmoid unstable current sheets at different slices in the simulated cubic computational domain.

We show the slice in the rest-mass density at $z = \pi/2$ in the Rel-MHD simulation with the resolution 512^3 in Fig. 10, with a few magnetic islands in the simulation box.[4] We check the profile of magnetic field components and magnetization in that region. For instance, we take a closer look at one plasmoid located at $(x, y) = (4.7, 3.68)$. In the right panel, we show the profile of magnetic field components, magnetization, and mass density along the dashed line at $y = 3.68$ with $x \in [4, 5.6]$. The mass density ρ reaches a local maximum at the position of the plasmoid, while the parallel magnetic field component B_x, and magnetization σ have a minimum local value. Such a profile confirms that there is a plasmoid at this point (Nathanail et al. 2020; Čemeljić et al. 2022). In the same Rel-MHD simulation, we made another slice, shown in Fig. A1, through the same simulation box in the xz plane at $y = 3.68$ (where the black dashed line is in Fig. 10). In the top panel, we show the reconnection layer and plasmoids. The zoomed plots show the magnetization of the selected reconnection layer. In the next section, we estimate the reconnection rate at this chosen layer.

Using the same method (just described for the 3D Rel-MHD simulation in the last paragraph), we choose the layer shown in Fig. A2 in the 3D Ideal-MHD run.

5 RECONNECTION RATE

Magnetic reconnection might occur spontaneously due to the internal MHD instability in a resistive model (Sweet 1958; Petschek 1964) or in the ideal MHD as a kink mode (Baty 2000). In a turbulent system, the external perturbation can cause magnetic reconnection in a so-called forced reconnection, where the plasma is in a state of chaotic and unpredictable motion. The magnetic field lines can become distorted and twisted, leading to reconnection (Vekstein & Jain 1998).

[4]Magnetic islands are 2D slices through the structures that are plasmoids in 3D.

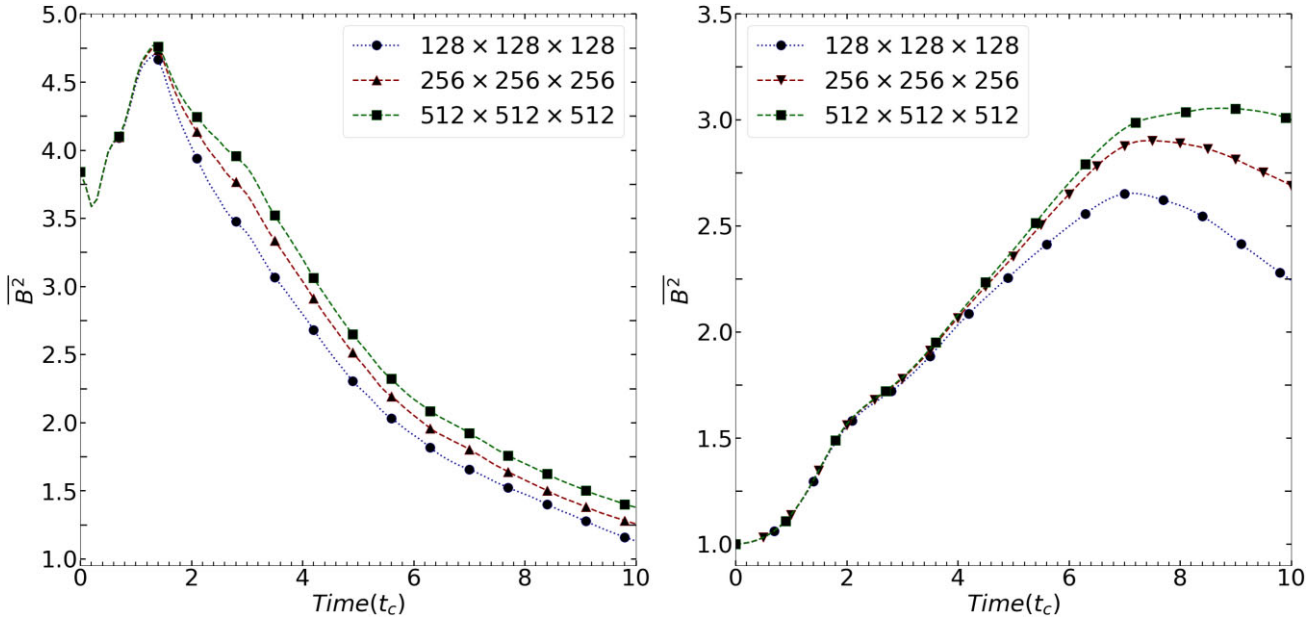

Figure 7. The time evolution of $\overline{B^2}$ in 3D simulations with PLUTO for the simulations Ideal-MHD (*left panel*) and Rel-MHD (*right panel*).

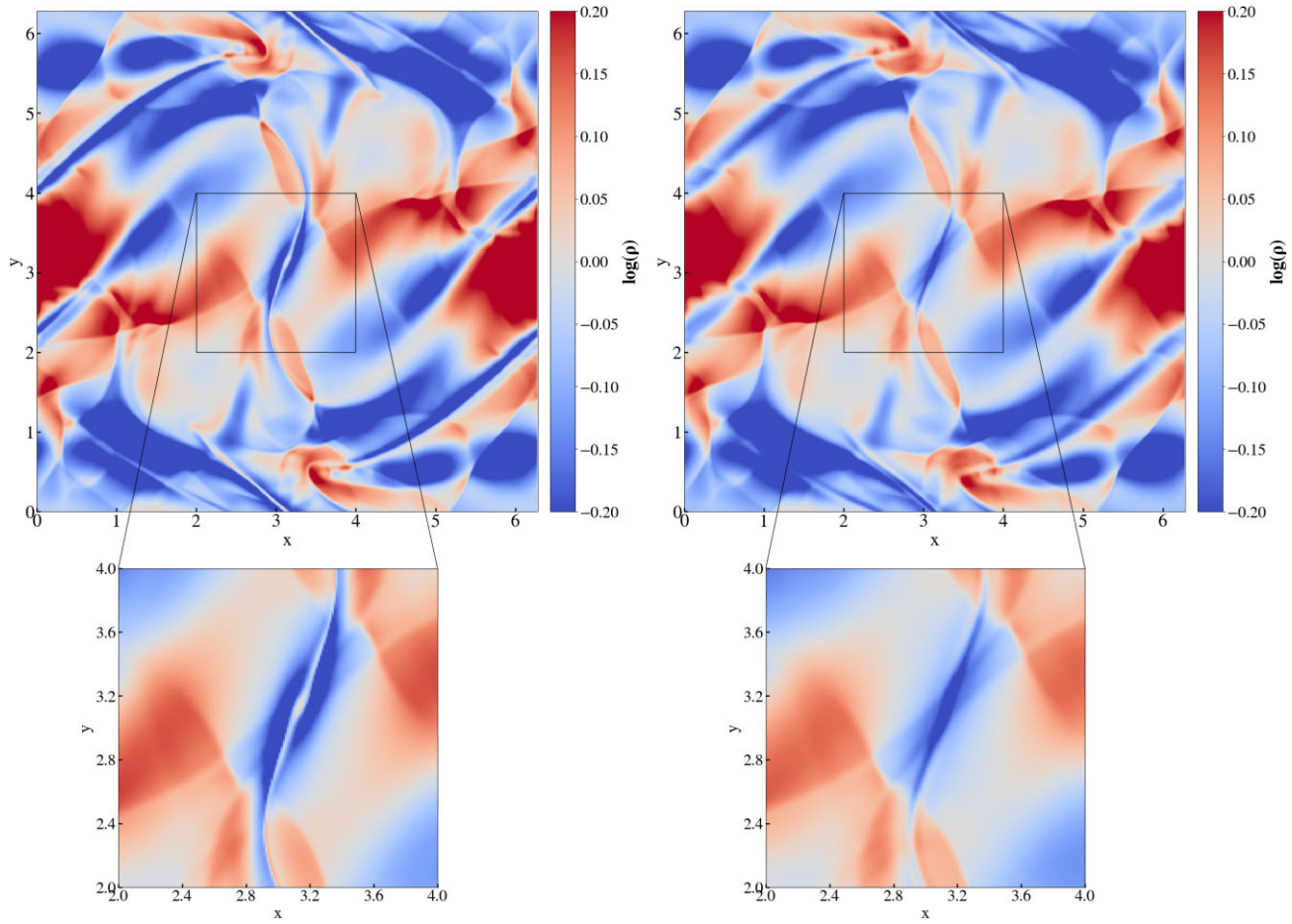

Figure 8. The slice in $z = \pi/2$ in the simulation box of the rest-mass density ρ for a vortex at $t = 1.5t_c$ at the resolution of 512^3 in PLUTO. *Left panel*: Ideal-MHD. *Right panel*: Res-MHD with $\eta = 10^{-3}$. The zoomed-in panels show the current layer in the middle of the simulation boxes. Plasmoids form only in the cases with sufficiently low resistivity, corresponding to a Lundquist number larger than 10^4 ($\eta \lesssim 10^{-4}$).

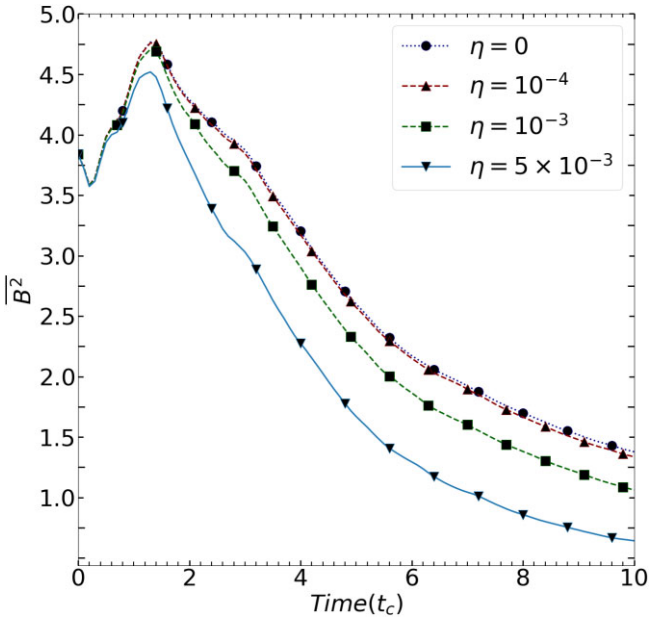

Figure 9. The time evolution of $\overline{B^2}$ in 3D Res-MHD simulations with PLUTO, at the resolution 512^3 with different physical resistivities.

Turbulent systems can be found in various environments, such as in the solar wind, in the interstellar medium, and in the accretion disks of black holes and neutron stars. In these environments, magnetic reconnection can lead to a variety of phenomena, such as the acceleration of particles to high energies, the formation of jets and flares, and the heating of the plasma. An external perturbation in turbulent plasma can accelerate the formation of the X-point, causing a reconnection one order of magnitude faster than spontaneous reconnection. Such a reconnection process is complex and still not well understood, and is an active area of research in astrophysics and plasma physics. There are analytical and numerical studies on forced magnetic reconnection including perturbation in the isolated current sheet (Vekstein & Jain 1998; Potter, Browning, & Gordovskyy 2019), and a study searching for the observational signatures of simulated forced reconnection in solar flares (Srivastava et al. 2019).

The OT is a vortex problem, for which turbulence develops during evolution. It is shown in the rest-mass density plots (Figs A3 and A4) that the current sheets are not formed in isolation, but are a result of evolution of high-density regions, which are driven together by the evolution of the system. Therefore, fast reconnection is expected in our simulations.

Fig. A5 in the Appendix shows selected reconnection layers in the chosen 2D simulations Ideal-MHD and Rel-MHD. When magnetic field lines reconnect, the magnetic tension acts to shorten the field lines and make a magnetic slingshot, which drives the outflow (plasmoids ejection) from both sides of the layer in the parallel direction (Dahlburg & Norton 1995; Linton, Dahlburg & Antiochos 2001).

For a steady-state reconnection, the outflow (from the reconnection area) should be balanced with the inflow (towards the reconnection layer) which is shown with the white arrows in the figure. The ratio of inflow and outflow velocity (v_{in} and v_{out}, respectively) is called the reconnection rate $v_r = v_{in}/v_{out}$.

The outflow propagates along the background magnetic field lines with the Alfvén speed $v_A = c\sqrt{\sigma/(\sigma+1)}$, in conventional units. When $\sigma \simeq 10$, $v_A \simeq c$, the reconnection rate can be approximated with $v_r = v_{in}/c$. The magnetization values on both sides of the reconnection layer in all simulations are greater than 8, as demonstrated in the Appendix (Figs. A1, A2, and A5). To compute the reconnection rate, we average the inflow velocity of 6 grid cells located on both sides of the layer. The structure of the layer is found by the Harris equilibrium method (Harris 1962; Ripperda, Bacchini & Philippov 2020).

According to analytical and numerical studies, the reconnection rate in 3D might be both lower or higher than in 2D. The reconnection rate depends on different parameters such as the initial set-up, strength of the magnetic field, and turbulence of the system. Čemeljić & Huang (2014) studied magnetic reconnection in 2D and 3D geometries using resistive MHD simulations and found that the reconnection rate in 3D was approximately twice as fast as in 2D. Huang & Bhattacharjee (2016) found that in some cases the 3D reconnection rate can be lower than the 2D reconnection rate due

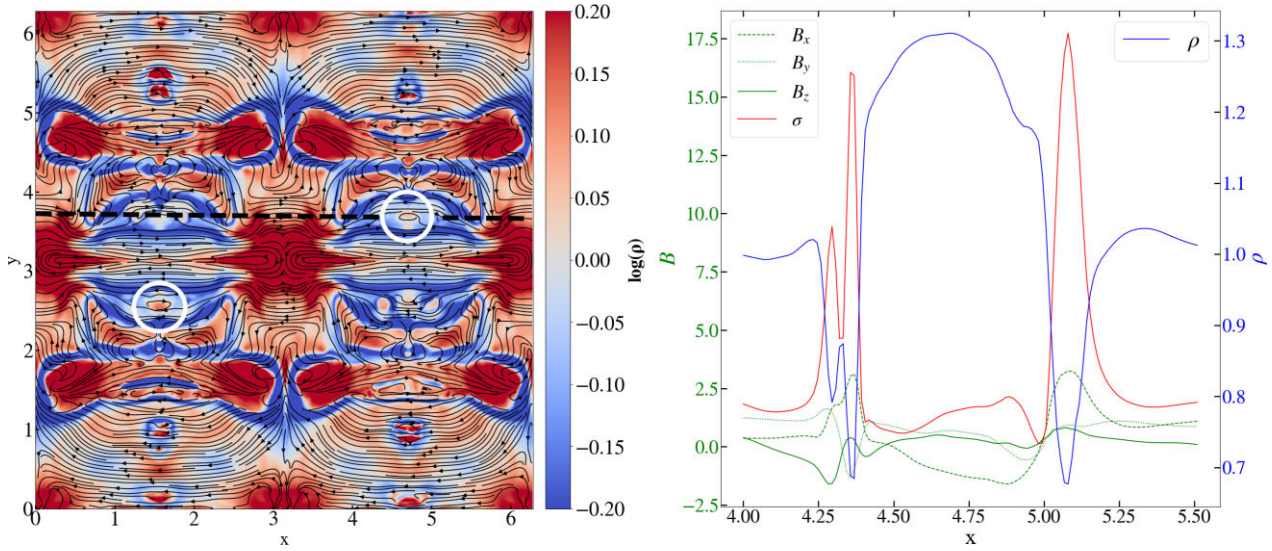

Figure 10. *Left panel*: A slice of the rest-mass density at $z = \pi/2$ in the Rel-MHD simulation in 3D at a resolution 512^3 with PLUTO. The streamlines indicate the magnetic field lines and the white circles show plasmoids. *Right panel*: The magnetic field components, magnetization, and density profile along the black dashed line at $y = 3.68$, shown in the left panel.

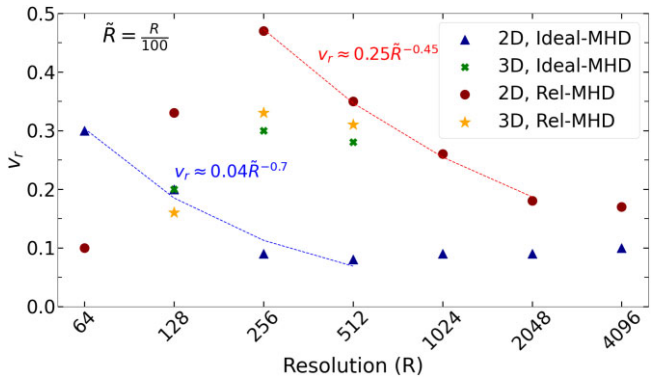

Figure 11. The reconnection rate as a function of resolution in the simulations Ideal-MHD and Rel-MHD with KORAL.

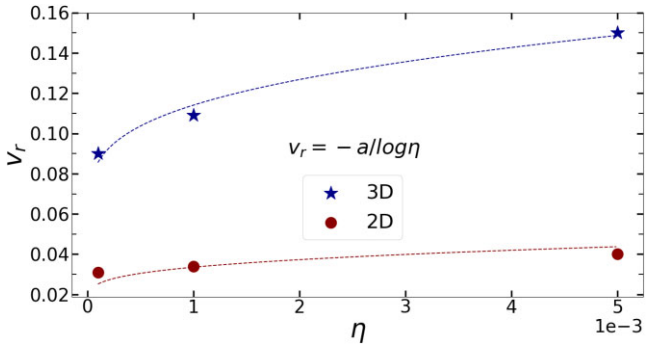

Figure 12. The reconnection rate as a function of resistivity for resistivities $\geq 10^{-4}$ (*Sweet* , 1958) in 2D (red circles) and 3D (blue stars) Res-MHD simulations with PLUTO. The change is cosistent with $1/\log S$ dependence, S being the Lundquist number.

to the complex interplay between the plasmoid instability and the turbulent background.

Our study presents various initial set-ups in both two and three dimensions (Section 3) that affect the magnetization on both sides of the connection region, which in turn influences the reconnection rate. Our Ideal-MHD simulations result in faster reconnection in 3D than in 2D, while the opposite is observed in the Rel-MHD simulations, where the reconnection rate is slower in 3D. In Fig. 11, we show $v_{\rm r}$ as a function of resolution in the simulations with KORAL simulations. We summarize the results of Fig. 11 as follows.

In 2D set-ups:

(1) Results of the Ideal-MHD simulations show that the resolution does not affect the reconnection rate in the resolutions $\geq 256^2$. We confirm that in the non-relativistic simulations, the current sheet is well resolved in the resolutions $\geq 256^2$ (It is also shown in the top panels of Fig. 13 at $t \simeq 2.5t_c$ that the curves of $\overline{B^2(t)}$ at higher resolutions are convergent). In the lower resolutions, the reconnection rate changes as a function of resolution $v_{\rm r} \approx 0.04\tilde{R}^{-0.7}$ ($\tilde{R} = R/100$).

(2) Results of the Rel-MHD simulations show that the reconnection rate changes as a function of the resolution as $v_{\rm r} \approx 0.25\tilde{R}^{-0.45}$ in the resolutions $\leq 2048^2$. The current sheets and plasmoids are well resolved in the two highest resolutions.

In both Ideal-MHD and Rel-MHD simulations in the lowest resolutions (64^2 and 128^2), the numerical resistivity is much higher than 10^{-4}, and the current layer is not resolved. The reconnection rate converges to a constant value at a lower resolution in the Ideal-MHD than in the Rel-MHD simulations. Therefore, in Rel-MHD, it is necessary to increase the resolution with respect to the non-relativistic case to reach a reconnection rate limit that is resolution independent.

In 3D set-ups, the current sheets are not resolved in the resolution 128^3. With the higher resolutions 256^3 and 512^3, we do not see a significant effect of the resolution. In KORAL, the lowest value of reconnection rate in 2D simulations at the highest resolution is about 0.1 in the Ideal-MHD and about 0.16 in the Rel-MHD. In 3D simulations, the value of the reconnection rate in the highest resolutions is around 0.3 in both Ideal-MHD and Rel-MHD simulations.

Turning to the resisitive simulations, in Fig. 12 we plot the reconnection rates of Res-MHD runs with $\eta = 10^{-4}$, 10^{-3}, and 5×10^{-3} in the resolution 512^2 in 2D and 512^3 in 3D. The reconnection rate changes as a function of resistivity, increasing by a factor of about 60 per cent in the 3D case and 30 per cent in the 2D one, as the resistivity changes from 10^{-4} to 5×10^{-3}. This increase is much smaller than the factor 7.07 expected from the Sweet–Parker law ($v_r \propto \eta^{1/2}$). The dependence seems to be consistent with $1/\log \eta$, instead.

Given our fairly low resolution and the small number of points, we cannot make definite claims about the functional form of the reconnection rate. However, the reconnection rate we find is consistent with the dependence on the Lundquist number predicted in Petschek reconnection ($v_r = a/\log S$, Petschek 1964). The proportionality constant is $a = 0.34$ for the 3D simulations[5], and $a = 0.10$ for the 2D simulations. Here, we assumed $v_{\rm A}L = 1$ and we take logarithms to the base 10 ($\log \equiv \log_{10}$). Since our flow is not strongly magnetized nor highly turbulent, the reconnection rate in our resistive simulations is below the rates from Lazarian & Vishniac (1999).

6 CODE COMPARISON

The codes we used in our simulations, PLUTO and KORAL, rely on solving the MHD equations (given in Section 2) employing the finite volume method. The initial equations are typically formulated in terms of the primitive variables, which include the fluid density, pressure, and velocity, as well as the magnetic field (given in Section 3). To solve the equations using the finite volume method, the computational domain is divided into a grid of cells, each of which contains a set of conserved quantities. These conserved quantities are related to the primitive variables through a set of conversion equations, which are typically derived from the conservation laws of mass, momentum, and energy. Although both PLUTO and KORAL employ the same scheme to calculate conserved quantity fluxes at the boundary of each grid cell, the conversion of primitive to conserved quantities differs between the two codes. PLUTO employs the inversion scheme provided by Mignone et al. (2007), while KORAL uses the $1D_W$ inversion scheme outlined in Noble et al. (2006).

We perform simulations of the OT test problem with PLUTO and KORAL codes in the simulations Ideal-MHD and Rel-MHD. The same initial conditions are used in both codes. Here, we compare the energy components in the results, the ability of the codes to capture substructures, and the reconnection rates. In Fig. 13, we present the time evolution results for the magnetic energy in the Ideal-MHD and Rel-MHD simulations in PLUTO and KORAL. The value of $\overline{B^2}$ in the simulations Ideal-MHD slightly increases in KORAL with respect to PLUTO. This difference in the value of $\overline{B^2}$ is more obvious in the

[5]For the 3D simulation, v_r is within ~ 10 per cent of $\pi/(8\log_{10}S)$, assuming $v_{\rm A}L = 1$. An accurate fit to this formula can be found if we allow values of the characteristic scale $v_{\rm A}L$ to be slightly larger than unity.

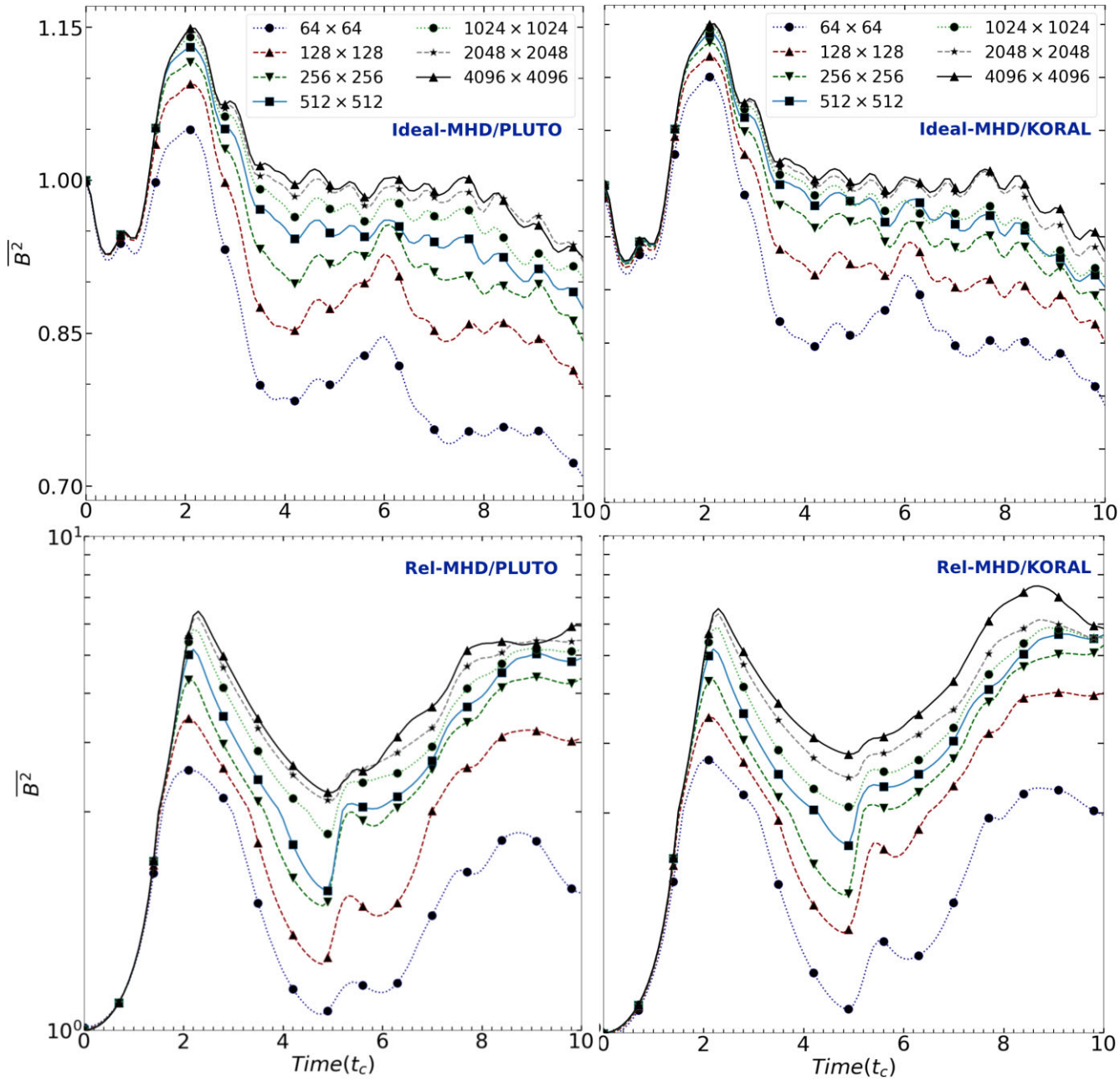

Figure 13. Time evolution of $\overline{B^2}$ in simulations with different resolutions using PLUTO (*left panels*) and KORAL (*right panels*) for the simulations Ideal-MHD (*top panels*) and Rel-MHD (*bottom panels*). The value of $\overline{B^2}$ is slightly higher in the simulations with KORAL. Note: The *y*-axis is common between left and right panels, and the legend is the same for all panels.

lower resolutions and in the later time steps. In addition, in Fig. 5, we showed that at the identical time steps of Rel-MHD simulation, the residual of the total energy in Rel-MHD in KORAL is typically slightly higher than the one in PLUTO.

To investigate the difference between the codes, we plot in Fig. A6 of Appendix A relative differences between KORAL and PLUTO of various quantities. In the Ideal-MHD simulations with sufficient resolution for the small numerical resistivity, both PLUTO and KORAL show almost the same numerical dissipation. In the Rel-MHD simulations, the difference between the codes is more pronounced. Also, by comparing the results in Ideal-MHD and Rel-MHD simulations in Fig. 13, we find that the numerical resistivity is negligible at the largest resolution 4096^2 in the Ideal-MHD simulations (the curves of two larger resolutions overlapping) while in the Rel-MHD simulations, one should increase the resolution to obtain a negligible numerical error.

As mentioned in Secton 4.1, we expect the plasmoid unstable current sheets when there is a hump in $\overline{B^2}$ plot. We show the rest-mass density plot at $t = 2.5t_c$ in the simulation Ideal-MHD and $t = 9t_c$ in the simulation Rel-MHD at the highest resolution 4096^2 in Appendix A, Figs A3 and A4. These density plots confirm that KORAL is more precise than PLUTO in capturing the substructures.

We compare the reconnection rate in the simulation Rel-MHD in PLUTO and KORAL in Fig. 14. In Fig. A6, we show that the

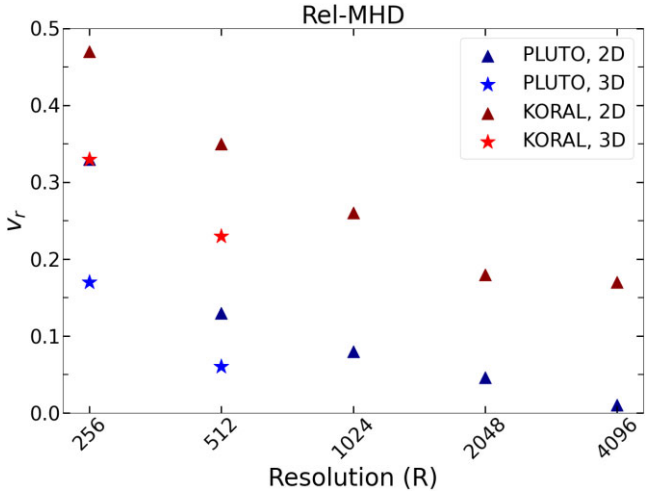

Figure 14. The reconnection rate as a function of resolution in simulations Rel-MHD in 2D and 3D. Red symbols indicate simulations with KORAL and blue symbols with PLUTO.

residual relative difference between various quantities in the Ideal-MHD simulation is at the level below 1 per cent, so we only compare v_r in the Rel-MHD simulation.

We observe that in both 2D and 3D set-ups the reconnection rate in KORAL simulations is higher than in PLUTO simulations. The magnetization on both sides of the reconnection layer directly affects the reconnection rate (which is discussed in Section 5), and we showed that in KORAL simulations the magnetic energy (and corresponding magnetization) is higher than in PLUTO simulations. This causes a higher reconnection rate in KORAL simulations compared to PLUTO simulations, as shown in Fig. 14.

7 SUMMARY AND CONCLUSIONS

We investigate how the resolution and dimensionality of the simulation set-up affect the energy dissipation, substructure formation, and reconnection rate, all of which are critically dependent in astrophysical simulations on the onset of reconnection. We study these effects by performing the Orszag–Tang test problem in the numerical simulation codes PLUTO and KORAL. We perform a quantitative comparison between the results obtained from various set-ups, including relativistic, non-resistive MHD (Rel-MHD), non-relativistic, non-resistive MHD (Ideal-MHD), non-relativistic, resistive MHD (Res-MHD), in 2D as well as 3D simulations.

First of all, we estimated the numerical resistivity of the simulations in each resolution to find a sufficient resolution in which we can resolve the substructures and study the energy conversion in our simulations. We used PLUTO code in resistive and non-resistive modes (Res-MHD and Ideal-MHD, respectively) in non-relativistic simulations. We show that the numerical resistivity in the resolution 512^2 in both 2D and 3D set-ups is $\eta \approx 10^{-4}$, which is also the limit of the formation of a plasmoid unstable current sheet.

After finding the sufficient resolution for overcoming the effects of numerical resistivity, we study energy conversion in Ideal MHD, Rel-MHD, and Res-MHD simulations. We showed that in Ideal-MHD and Res-MHD simulations magnetic energy converts into internal energy and heats up the plasma. In Ideal-MHD simulation a part of magnetic energy converts to kinetic energy which accelerates the plasmoids out of the reconnection layer. We also show that in Res-MHD simulations, as expected, the magnetic energy dissipation increases with increasing physical resistivity. In higher resistivity cases, there is a corresponding increase in internal energy.

In relativistic simulations, Rel-MHD, we find that the relativistic shocks amplify the magnetic field with the magnetic energy $\overline{E_B}$ increasing by a factor of 5 at $t = 20$ per cent of total simulation time. It is also shown that magnetic energy converts into internal and kinetic energies which amplify the magnetic field for the second time during our simulation. The second increase in magnetic energy at $t =$ 90 per cent of total simulation time is coincident with the formation of a set of plasmoid unstable current sheets.

We also compare two state-of-the-art codes, PLUTO and KORAL, in both non-relativistic and relativistic simulations. Our findings indicate that in both Ideal-MHD and Rel-MHD simulations, KORAL simulations show higher magnetic energy, $\overline{B^2}$, (implying less magnetic dissipation) compared to PLUTO with the difference more prominent at low resolutions. We show that in resolution 1024^2, in the Ideal-MHD simulations, the relative difference of relevant quantities in PLUTO and KORAL is less than 10^{-2}, while in the Rel-MHD simulations, for some quantities the residual reaches 0.1. In the highest resolution run (4096^2), we found that KORAL captures more substructures than PLUTO in both Ideal-MHD and Rel-MHD simulations. We show that the reconnection rate in all simulations in KORAL is higher than that in PLUTO – it is caused by higher magnetization in the reconnection layer region in KORAL.

We study the effect of resolution on the reconnection rate v_r in our simulations. As expected, numerical resistivity influences the reconnection rate. Increasing the resolution leads to a decrease in both numerical dissipation and reconnection rate. In 2D simulations, v_r is initially a function of scaled resolution ($\tilde{R} = R/100$) as $v_r \approx 0.04\tilde{R}^{-0.7}$ (Ideal-MHD) and $v_r \approx 0.25\tilde{R}^{-0.45}$ (Rel-MHD). In each set of simulations, we find a resolution beyond which the reconnection rate is no longer affected by the resolution, and we find the limiting reconnection rate in this limit: in 2D simulations in KORAL, in the Ideal-MHD runs, $v_r = 0.1$ for resolutions $\geq 512^2$; in the Rel-MHD, $v_r \approx 0.18$ for resolutions $\geq 2048^2$. In PLUTO simulations, the reconnection rate is lower than that in KORAL simulations. In PLUTO, in Ideal-MHD $v_r \approx 0.03$, in Rel-MHD $v_r \approx 0.05$.

We infer that the Rel-MHD simulations should be performed at resolutions at least four times larger than in the non-relativistic Ideal-MHD simulations, to reach a negligible effect of the resolution on the reconnection rate.

In 3D simulations in KORAL, the Ideal-MHD and Rel-MHD simulations are not directly comparable since we initialized the velocity and magnetic fields differently. Still, in both set-ups, the results are remarkably similar, with the effect of resolution on v_r not significant in higher resolutions. In both Ideal-MHD and Rel-MHD simulations with resolution 512^3 the reconnection rate $v_r \simeq$ 0.3 (Fig. 11).

When comparing the reconnection rate in 2D and 3D set-ups, it is crucial to consider several parameters, such as the initial set-up, the strength and topology of the magnetic field, and the turbulence of the system. In set-ups with the equivalent magnetization and turbulence levels, we show that the reconnection rate in 3D ideal MHD simulations is lower than that observed in 2D simulations. This trend is particularly notable in relativistic simulations when comparing the 2D and 3D set-ups. However, in the resistive runs (Res-MHD) the trend is the opposite, the reconnection rate is about a factor of 3 smaller in 2D simulations than in 3D ones. We also show that in the resistive simulations, the reconnection rate seems to be well approximated by a $v_r \propto 1/\log \eta$ dependence, reminiscent of Petschek's fast reconnection (Petschek 1964).

The results presented here add to the information needed to evaluate the behavior of numerical MHD codes in different set-ups. The performance of the codes can be evaluated and compared only with a detailed account of the relation between the substructure formation and the amount of energy in each component. By using the standard Orszag–Tang test, we provided detailed quantitative information on energy components, reconnection rates and substructure formation. Our approach can be followed – and the results compared – for other codes.

A caveat in our work here is that, because of the computational expense, we did not follow the convergence of the results in 3D up to the same resolutions as we did in the 2D set-ups. The new generation of simulations will unavoidably need such an update in benchmarking. The convergence of vorticity will be addressed in future work.

ACKNOWLEDGEMENTS

This project was funded by the Polish NCN grant No. 2019/33/B/ST9/01564. MČ acknowledges the Czech Science Foundation (GAČR) grant No. 21-06825X. MW was supported by the European Research Council advanced grant 'M2FINDERS – Mapping Magnetic Fields with INterferometry Down to Event hoRizon Scales' (grant No. 101018682). High-resolution computations in this work were performed on the Prometheus and Ares machines, part of the PLGrid infrastructure. We thank K. Nalewajko and B. Ripperda for inspiring discussions and suggestions.

DATA AVAILABILITY

The data underlying this article will be shared on reasonable request to the corresponding author.

REFERENCES

Abarca D., Parfrey K., Kluzniak W., 2021, ApJ, 917, L31
Akasofu S.-I., 1968, Magnetospheric Substorm. Springer Netherlands, Dordrecht, p. 212
Baty H., 2000, A&A, 353, 1074
Bell A., 1978, MNRAS, 182, 147
Biskamp D., 2003, Magnetohydrodynamic Turbulence, Cambridge University Press, Cambridge
Blandford R. D., Ostriker J. P., 1978, ApJ, 221, L29
Čemeljić M., 2019, A&A, 624, A31
Čemeljić M., Huang R. Y., 2014, Phys. Plasmas, 21, 032121
Čemeljić M., Vlahakis N., Tsinganos K., 2014, MNRAS, 442, 1133
Čemeljić M., Yang H., Yuan F., Shang H., 2022, ApJ, 933, 55
Chael A., Narayan R., Johnson M. D., 2019, MNRAS, 486, 2873
Chen G., Armstrong T. P., 1975, in Acceleration of charged particles in oblique MHD shocks, International Cosmic Ray Conference, Munich, p. 1814
Colombo S. et al., 2019, A&A, 629, L9
Coppi B., Laval G., Pellat R., 1966, Phys. Rev. Lett., 16, 1207
Dahlburg R. B., Norton D., 1995, in Meneguzzi M., Pouquet A., Sulem P.-L., eds, Small-Scale Structures in Three-Dimensional Hydrodynamic and Magnetohydrodynamic Turbulence. Springer, Berlin, p. 331
Dahlburg R. B., Picone J. M., 1989, Phys. Fluids B, 1, 2153
Del Zanna L., Papini E., Landi S., Bugli M., Bucciantini N., 2016, MNRAS, 460, 3753
Dexter J. et al., 2020, MNRAS, 497, 4999
Flock M., Dzyurkevich N., Klahr H., Turner N. J., Henning T., 2011, ApJ, 735, 122
Gammie C. F., McKinney J. C., Toth G., 2003, ApJ, 589, 444
Giannios D., Uzdensky D. A., Begelman M. C., 2009, MNRAS, 395, L29
Giovanelli R. G., 1946, Nature, 158, 81
Harris E. G., 1962, Nuovo Cimento, 23, 115
Huang Y.-M., Bhattacharjee A., 2016, ApJ, 818, 20
Jiang C. et al., 2021, Nat. Astron., 5, 1126
Komissarov S. S., Barkov M., Lyutikov M., 2007, MNRAS, 374, 415
Lančová D. et al., 2019, ApJ, 884, L37
Lazarian A., Vishniac E. T., 1999, Apj, 517, 700
Linton M., Dahlburg R., Antiochos S., 2001, ApJ, 553, 905
Loureiro N. F., Schekochihin A. A., Cowley S. C., 2007, Phys. Plasmas, 14, 100703
van Marle A. J., Casse F., Marcowith A., 2017, MNRAS, 473, 3394
McPherron R. L., 1979, Rev. Geophys., 17, 657
Mehlhaff J. M., Werner G. R., Uzdensky D. A., Begelman M. C., 2020, MNRAS, 498, 799
Mignone A., Bodo G., Massaglia S., Matsakos T., Tesileanu O., Zanni C., Ferrari A., 2007, ApJS, 170, 228
Mininni P. D., Pouquet A. G., Montgomery D. C., 2006, Phys. Rev. Lett., 97, 244503
Nathanail A., Fromm C. M., Porth O., Olivares H., Younsi Z., Mizuno Y., Rezzolla L., 2020, MNRAS, 495, 1549
Noble S. C., Gammie C. F., McKinney J. C., Zanna L. D., 2006, ApJ, 641, 626
Olivares Sánchez H., Porth O., Mizuno Y., 2018, J. Phys. Conf. Ser., 1031, 012008
Orszag S. A., Tang C.-M., 1979, J. Fluid Mech., 90, 129
Petschek H. E., 1964, in Vol. 50, The Physics of Solar Flares, NASA Special Publication. p. Goddard Space Flight Center, Greenbelt 425
Potter M. A., Browning P. K., Gordovskyy M., 2019, A&A, 623, A15
Ripperda B., Bacchini F., Philippov A. A., 2020, ApJ, 900, 100
Ripperda B., Liska M., Chatterjee K., Musoke G., Philippov A. A., Markoff S. B., Tchekhovskoy A., Younsi Z., 2022, ApJ, 924, L32
Sądowski A., Narayan R., Tchekhovskoy A., Zhu Y., 2013, MNRAS, 429, 3533
Sądowski A., Narayan R., McKinney J. C., Tchekhovskoy A., 2014a, MNRAS, 439, 503
Sądowski A., Narayan R., Tchekhovskoy A., Abarca D., Zhu Y., McKinney J. C., 2014b, MNRAS, 447, 49
Sądowski A., Wielgus M., Narayan R., Abarca D., McKinney J. C., Chael A., 2017, MNRAS, 466, 705
Srivastava A. K. et al., 2019, ApJ, 887, 137
Stepanovs D., Fendt C., 2014, ApJ, 793, 31
Strugarek A., Brun A. S., Matt S. P., Réville V., 2014, ApJ, 795, 86
Sweet P. A., 1958, 6, 123
Tzeferacos P., Ferrari A., Mignone A., Zanni C., Bodo G., Massaglia S., 2009, MNRAS, 400, 820
Varela J., Réville V., Brun A. S., Zarka P., Pantellini F., 2018, A&A, 616, A182
Vekstein G. E., Jain R., 1998, Phys. Plasmas, 5, 1506
White C. J., Stone J. M., Gammie C. F., 2016, ApJS, 225, 22
Wielgus M. et al., 2022, A&A, 665, L6
Zanni C., Ferreira J., 2009, A&A, 508, 1117

APPENDIX A: FORMATION OF PLASMOIDS

In this Appendix, we provide additional figures to support the findings and conclusions presented in the main text. In particular, the plots presented here are intended to help visualizing the plasmoids in 2D and 3D simulations, the reconnection layer and magnetization of the upstream region of the reconnection layer, and the comparison of numerical codes. The zoomed panels in Figs A1 and A2 correspond to the Ideal-MHD and Rel-MHD simulations, respectively, in 3D, and show a magnetization of $\sigma \approx 10$ on both sides of the reconnection layer.

The rest-mass density in the Ideal-MHD simulations with the resolution 4096^2 at $t = 2.5t_c$ is shown in Fig. A3. The zooms in the frames at the bottom panels show the chain of plasmoids in the

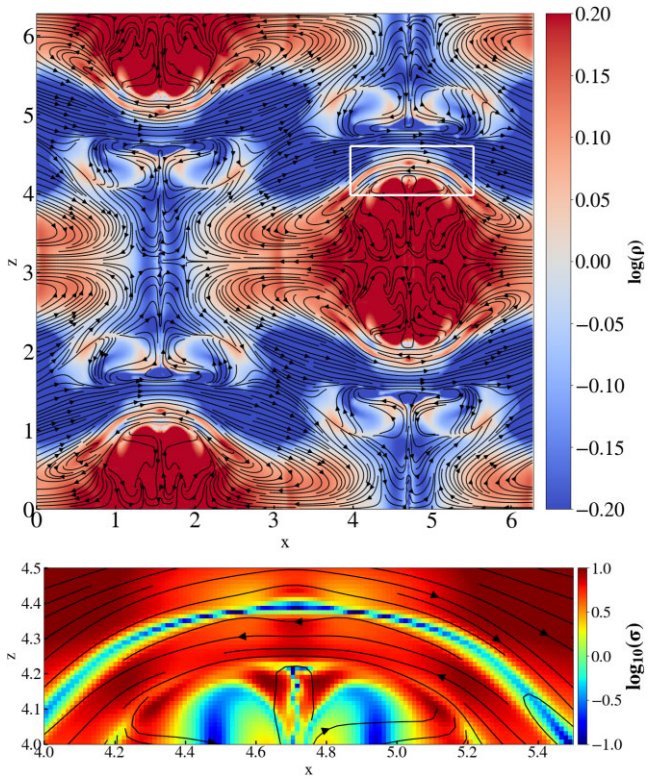

Figure A1. In the *top panel* is shown a slice in the rest-mass density at $y = 3.68$ in the Rel-MHD simulation in 3D with PLUTO, at the resolution 512^3. The white box shows the reconnection layer contains a plasmoid. The streamlines indicate the magnetic field. In the *bottom panel* we plot the magnetization of the selected region (white box).

centre of the simulation boxes. In the KORAL simulation, there are more X-points, probably because of the lower numerical resistivity. The rest-mass density plot of the Rel-MHD simulation with the resolution 4096^2 is shown in Fig. A4. This figure shows the result at a time $t = 9t_c$, with the second hump in $\overline{B^2}$ (discussed in Section 4.2). There are two plasmoid unstable current sheets in the PLUTO simulation box, along the $(0, \pi)$–$(\pi, 2\pi)$ and $(\pi, 0)$–$(2\pi, \pi)$ lines. In the KORAL simulation, two more current sheets are resolved in the bottom and top of the box, along $(\pi, 0)$–$(0, \pi)$ and $(\pi, 2\pi)$–$(2\pi, \pi)$. The zoomed frames at the bottom of this figure show the same regions in PLUTO and KORAL simulation boxes.

Fig. A5 shows reconnection layers, the so-called magnetic diffusion region, in the Ideal-MHD simulation (top panel) and the Rel-MHD simulation (bottom panel). The colour bar indicates the magnetization. The solid lines with arrows represent the streamlines of the magnetic field, pointing in opposite directions around the reconnection layer. The reconnected line (slingshot) can be seen in the plasmoid region at $(0, \pi)$ in the Rel-MHD simulation in the bottom panel. This plot shows that the magnetization σ in the upstream region of the current sheet in the Ideal-MHD simulations in 2D is $\approx$8 and in the Rel-MHD simulations in 2D it is $\approx$10.

In Fig. A6, we plot the residual quantities $R_Q = |Q_{\rm KORAL} - Q_{\rm PLUTO}|/Q_{\rm KORAL}$ (Q represents the compared quantity) to clarify the difference between PLUTO and KORAL simulations. The black dashed curves correspond to the Ideal-MHD simulation and the blue solid curves correspond to the Rel-MHD simulation. We compute R_Q in

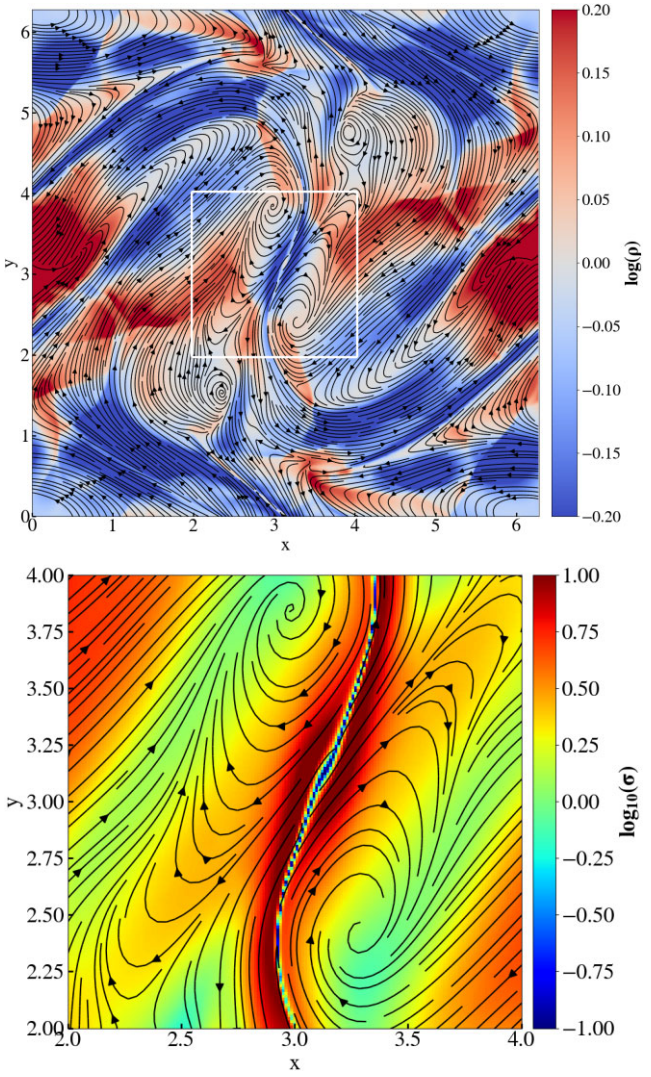

Figure A2. In the *top panel* is shown a slice in the rest-mass density at $z = \pi$ in the Ideal-MHD simulation in 3D with PLUTO, at the resolution 512^3. The white box shows the reconnection layer contains a plasmoid. The streamlines indicate the magnetic field. In the *bottom panel* , we plot the magnetization of the selected region (white box).

the results with the resolution of 1024^2, at which the numerical dissipation is small. In the Ideal-MHD simulation, the residuals of magnetic energy $\overline{E_B}$ and magnetization $\overline{\sigma}$ are less than 10^{-2} while in the Rel-MHD simulation, the residuals reach 0.1. In the Ideal-MHD simulation, the residual of kinetic energy $\overline{E_k}$ is less than 10^{-2}, while in the Rel-MHD simulation, it is less than 10^{-1}. The residuals of internal energy $\overline{U_{\rm int}}$ and density $\overline{d} \equiv \overline{\Gamma\rho}$ in the Ideal-MHD simulation are of the order of 10^{-4} and in the Rel-MHD simulation they are of the order of 10^{-2}. We conclude 10 per cent level code consistency for Rel-MHD and 1 per cent level consistency for non-relativistic Ideal-MHD simulations.

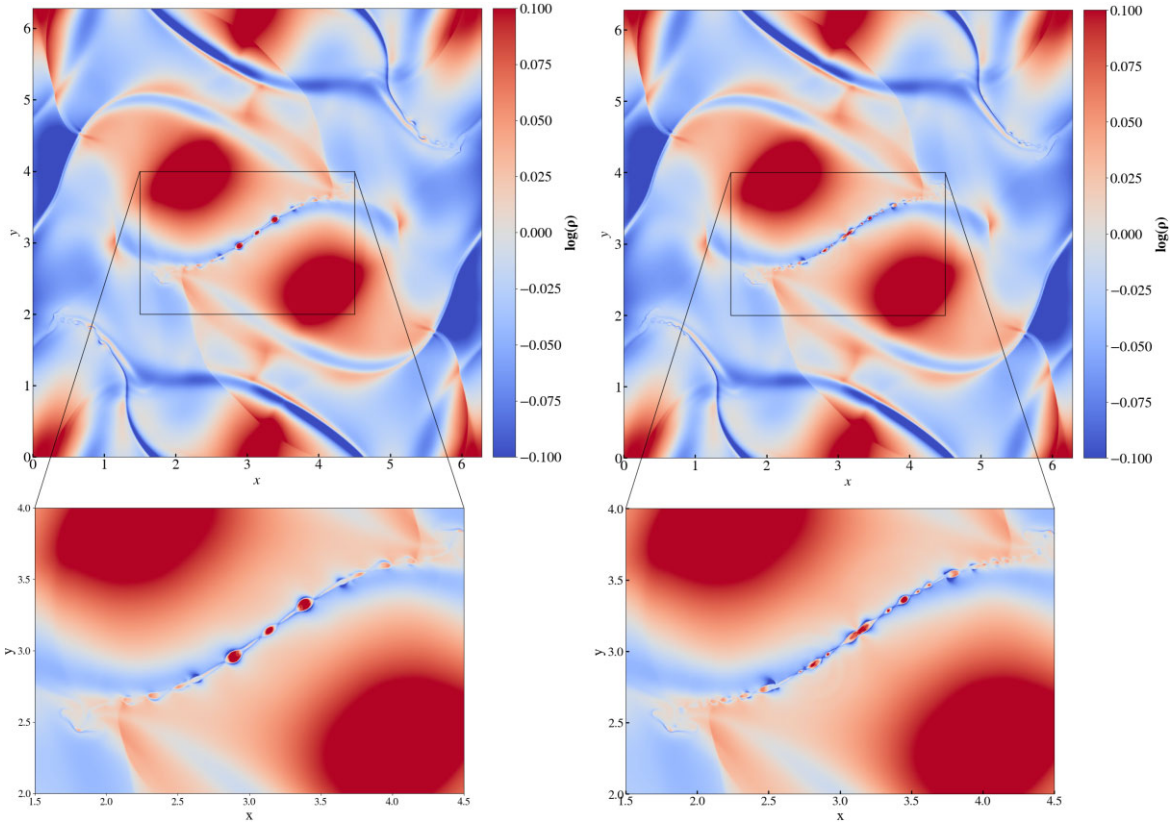

Figure A3. The rest-mass density ρ for a vortex at $t = 2.5t_c$ in the Ideal-MHD simulation at the resolution of 4096^2 in PLUTO (*left panels*) and KORAL (*right panels*). Due to lower numerical dissipation, KORAL is more precise in capturing the substructure in the simulations.

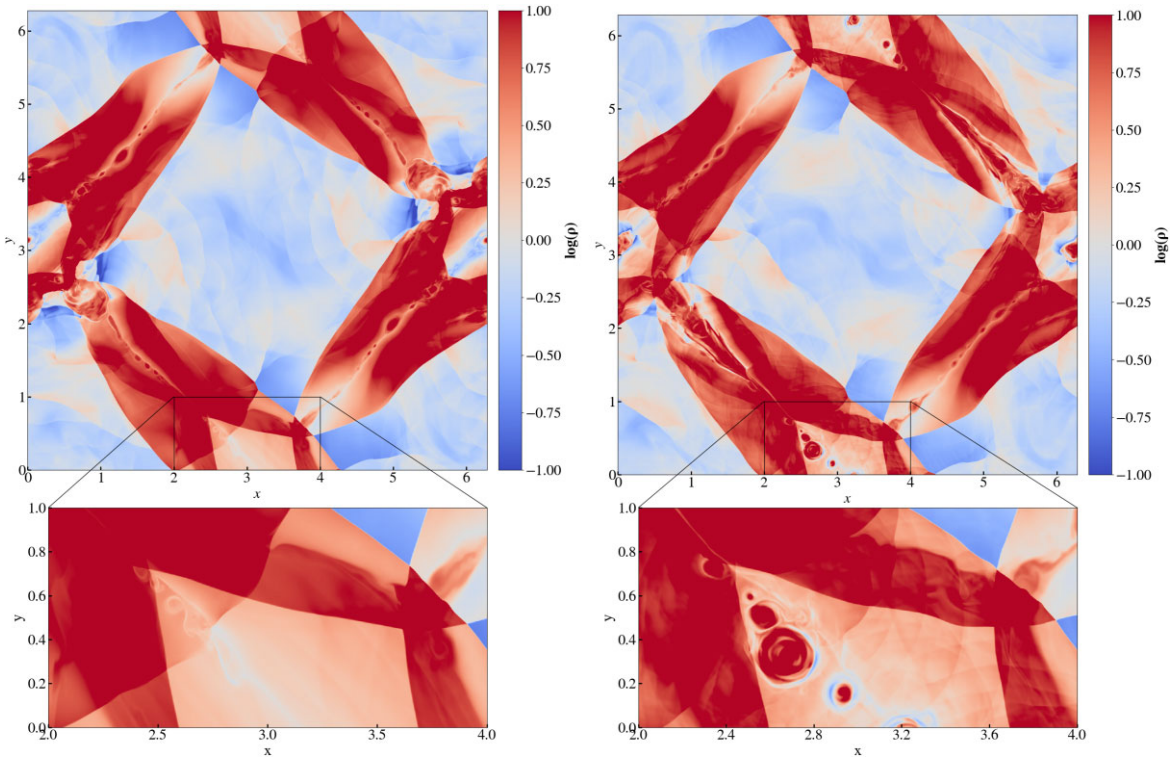

Figure A4. Rest-mass density ρ for a vortex at $t = 9t_c$ of the Rel-MHD simulation with the resolution 4096^2 in PLUTO (*left panels*) and KORAL (*right panels*). Due to lower numerical dissipation, KORAL is more precise in capturing the substructure.

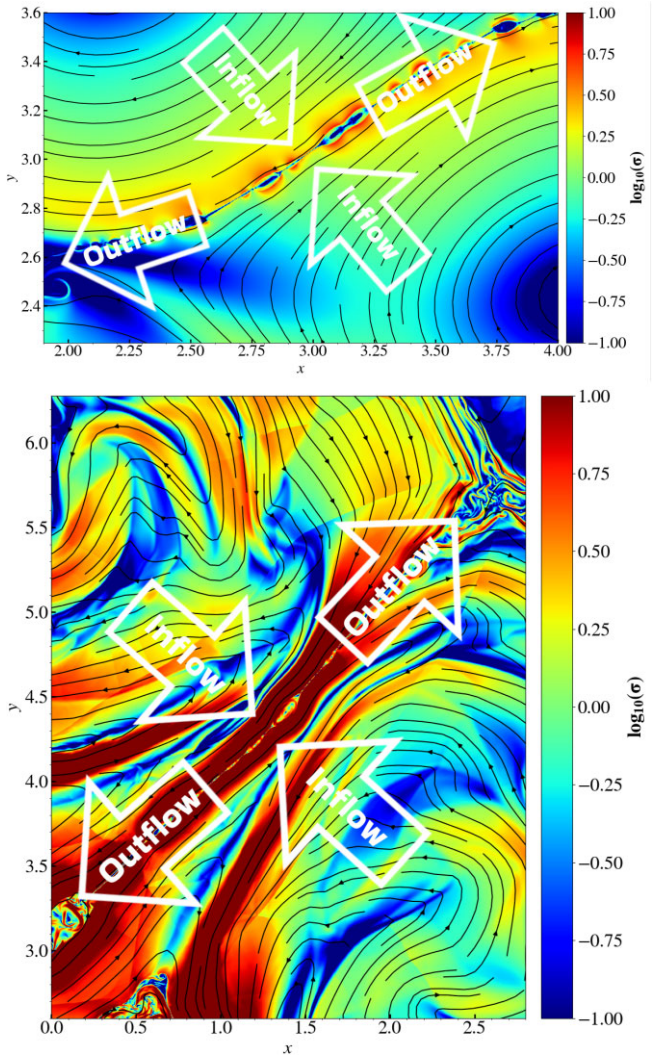

Figure A5. The reconnection layer is visible in the magnetization in simulations with KORAL at the resolution 4096^2 grid cells in the centre of the simulation box in the Ideal-MHD simulation (*top panel*) and along the (0, π)–(π, 2π) line in the simulation box in the Rel-MHD simulation (*bottom panel*). The streamlines show the magnetic field.

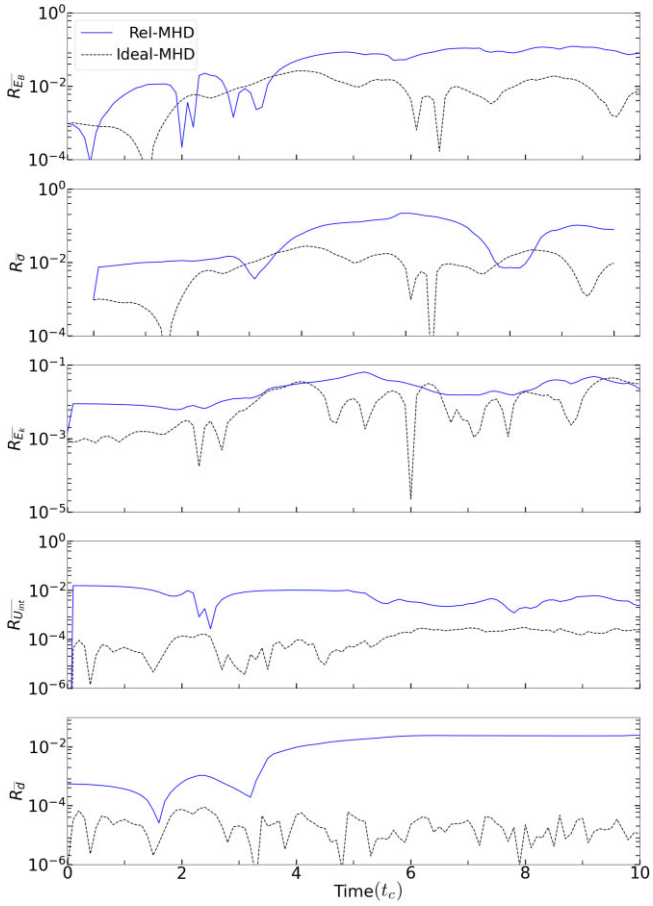

Figure A6. The residual of quantities Q, $R_Q = |Q_{\rm KORAL} - Q_{\rm PLUTO}|/Q_{\rm KORAL}$, in KORAL and PLUTO with the resolution 1024^2. We show (from *top* to *bottom*) the residuals for the magnetic energy, $R_{\overline{E_B}}$, magnetization, $R_{\overline{\sigma}}$, kinetic energy, $R_{\overline{E_k}}$, internal energy, $R_{\overline{U_{\rm int}}}$ and density, $R_{\overline{d}}$.

This paper has been typeset from a TEX/LATEX file prepared by the author.

Chapter 3

Study of Super-Eddington accretion onto neutron stars with moderate magnetic field

In this chapter, I present the numerical simulations of super-Eddington accretion onto neutron stars with dipolar magnetic fields. The simulations are initialized with an equilibrium torus with the loop magnetic field lines oriented in the opposite direction of the dipolar magnetic field lines. The magnetic reconnection, during the simulations, facilitates the accretion along the field lines to the surface of the neutron star in the presence of a strong dipole field. The new interesting aspect of this study is the dynamic evolution of radiation throughout the simulations.

I conduct two sets of simulations to study the impact of dipole strength and super-Eddington accretion rate on the accretion structure and luminosity of neutron star ULXs. In the first set of simulations, based on the KLK model (King, Lasota, & Kluźniak, 2017), I vary the strength of the magnetic field of the neutron star in the range from 10^{10} G to 10^{11} G, maintaining an accretion rate exceeding $200\,L_{\rm Edd}c^{-2}$. In the second set of simulations, I fix the magnetic field of the neutron star and vary the accretion rate in the range of about $\dot{M} = 100 - 1000\,L_{\rm Edd}c^{-2}$ for two distinct magnetic field strengths, 1×10^{10} G and 3×10^{10} G. The objective is to characterize an accreting neutron star system that exhibits apparent luminosity comparable to that of ULXs. The key information of models is shown in Table. 3.1.

This chapter is organized into sections as follow. In Section 1.3.5, I introduce the numerical methods used for the simulations, including the initial and boundary conditions, computational resources, and relevant physical adjustments. In Section 3.2, I discuss the first set of simulations with variation of the magnetic field strength of the neutron star. Next in Section 3.3 are discussed the simulations which examine the impact of the accretion rate. In the final section of this chapter, I summarize and conclude the results.

The results of the study that address the impact of dipole strength on outflows and beaming emission are prepared for submission to the *"Astrophysical Journal Letters"* (ApJL). The remaining results will be compiled into a comprehensive paper to be prepared after the submission of this thesis.

Table 3.1: Models with different neutron star magnetic field B and accretion rates $\dot{M}$. The accretion rate is computed at the steady-state radius of $20\,r_{\rm g}$, and the outflow rate $\dot{M}_{\rm out}$ at $100\,r_{\rm g}$. The apparent luminosity $L_{\rm iso}$ and minimum beaming factor $b_{\rm min}$ are computed at distance $500\,r_{\rm g}$. The maximum simulation time of each model is denoted by $t_{\rm max}$.

B [G]	$\dot{M}$ $[L_{\rm Edd}c^{-2}]$	$\dot{M}_{\rm out}$ $[L_{\rm Edd}c^{-2}]$	$L_{\rm iso}$ $[L_{\rm Edd}]$	$b_{\rm min}$	$t_{\rm max}$ $[t_{\rm g}]$
1×10^{10}	257	325	115	0.016	50 000
2×10^{10}	320	317	100	0.020	50 000
3×10^{10}	345	250	90	0.023	50 000
5×10^{10}	355	150	68	0.026	50 000
7×10^{10}	430	190	45	0.045	50 000
1×10^{11}	490	80	39	0.083	50 000
1×10^{10}	120	65	42	0.05	40 000
1×10^{10}	900	4000	220	0.008	40 000
3×10^{10}	144	30	40	0.05	40 000
3×10^{10}	1000	3600	185	0.010	40 000

3.1 Simulations details

I conducted simulations of accretion onto a neutron star with a dipolar magnetic field in GRRMHD code `Koral`. This section details the initial setup and boundary conditions of the simulations.

3.1.1 Initial conditions

The simulations in this thesis are initialized with the equilibrium torus based on the solution from Penna, Kulkarni, & Narayan (2013). The torus is initialized with a polytropic equation of state. Outside of the torus the background atmosphere is defined with density and internal energy of a few orders smaller than the initial torus. As the torus solution given by Penna, Kulkarni, & Narayan (2013) is not radiative, re-distribution of pressure is necessary, so that the pressure is divided between gas and radiation, with the assumption of local thermal equilibrium (more details are given in Abarca, Parfrey, & Kluźniak, 2021).

The torus has a single loop magnetic field defined with vector potential, A_ϕ. The MRI mechanism is utilized for angular momentum transfer during the simulation. Since MRI requires a weak magnetic field, the torus is initialized with the ratio of the total pressure of gas and radiation to the magnetic pressure $\beta = (p_{\rm gas}+p_{\rm rad})/p_{\rm mag} = 10$.

The initial stellar magnetic field is set up using the dipole potential from Wasserman & Shapiro (1983) and is adjusted to achieve various maximum surface field strengths. The dipole and torus loops are oriented in opposite directions so that when the simulation starts they converge and reconnect. This allows the material to flow along the field lines and accrete onto the neutron star.

3.1.2 Boundary conditions

The boundary conditions of the simulations are identical to that in Abarca, Parfrey, & Kluźniak (2021) and are as follows:

Azimuthal boundary. The simulations in this thesis are in 2D axisymmetry coordinates, meaning that there is only one grid cell in the ϕ dimension. In the entire simulation, all quantities copy into the ghost cell of each direction.

Polar boundary. In the polar direction, the simulations are set in the angles between zero and π. At the upper and lower boundaries (polar regions), all the vectors and the factor $\sin(\theta)$ of the metric will get zero value near the poles. To address this problem we set the first two cells in the polar region to be ghost cells to which we copy all quantities from the third cell.

Radial boundary. The outer boundary refers to the outer edge of the simulation domain. In the r direction, gas, radiation, and magnetic fields are taken to flow out of the simulation domain, with their quantities conserved across the boundary.

The inner radial boundary is the most difficult and challenging part. I use the energy-reflecting boundary implemented in `Koral` by Abarca, Parfrey, & Kluźniak (2021). First, we treat the gas following the method given by Parfrey & Tchekhovskoy (2017), where gas slides along magnetic field lines and falls smoothly onto the surface of the neutron star. This is similar to setting an absorbing boundary. Next, we treat the influx of kinetic, thermal, and radiative energy. The radiation flux[1] $R^t{}_r$ is set to be equal to the negative value of the sum of the fluxes in two ghost cells above the surface of the neutron star. This way the in-going energy fluxes convert to out-going radiation flux. Then, we multiply $R^t{}_r$ by the albedo which indicates the percentage of the energy flux to be reflected from the surface of the neutron star. In this study, I choose an albedo equal to 0.75. We then scale $R^t{}_t$ by $R^t{}_r$ so that the energy is conserved across the inner boundary.

It is important to mention that the actual radiation flux at the inner boundary is computed using a Riemann solver. In the ghost cells, the flux is defined to reflect 75% of the radiation. However, the HLL Riemann solver computes the flux at the midpoint, with the left half taken from the ghost cell and the right half from the domain cell. As a result, the actual reflection is expected to be less than the defined value. So that, numerical artifacts in conditions of extremely high accretion rates and strong magnetic fields may dominate the inner boundary conditions.

3.1.3 Simulation setup

The simulations are set on 2D grid with $N_r \times N_\theta \times N_\phi \equiv 510 \times 512 \times 1$ cells. The resolution is defined using the logarithmic spacing in the radial direction. The computational domain in the radial direction is from the surface of the neutron star at $5\,r_{\rm g}$ to $1000\,r_{\rm g}$ where $r_g = GM/c^2$ is the gravitational radius. In the polar direction, the domain is from 0 to π as mentioned earlier.

[1]The radiation flux $R^t{}_r$ is evolved in the code using Eqs. 1.14 and 1.15. In the diagonal metric that is used in the computations of this chapter $R^r{}_t = R^t{}_r g^{rr} g_{tt}$.

The simulations are run longer than $40\,000\,t_g$ where $t_g = GM/c^3$ is gravitational time. The simulations are sufficiently long to allow the disk to reach a steady state. Most of the results presented in this thesis are based on the time-averaged data.

3.1.4 Computational resources and tools

I performed the simulations on the Polish Grid Infrastructure PLGRID [2] with Prometheus, and Ares supercomputers using 960 cores at a time running for three or four days each, approximately one million hours of the computational time for all simulations of this study including the test runs. To optimize computational resources, I carefully selected the resolution in each direction for our simulations, e.g. the grid-cells in radial direction change logarithmically so that we define higher resolution closer to the accretor to study the accretion column, outflows, and radiation flux.

The data analysis and post-processing have been done on high-performance computers with 16 processors. Python, along with libraries such as Numpy (van der Walt, Colbert, & Varoquaux, 2011; Harris, Millman, et al., 2020), Scipy (Gommers, Virtanen, et al., 2024), Matplotlib (Hunter, 2007), and Pandas (McKinney et al., 2010), was employed for data analysis. Additionally, I have used the software Visit[3] for initial data visualization and on-the-run checking.

3.1.5 Physical adjustment

The neutron star has a mass of $1.4\,M_\odot$ and radius $5\,r_g$. The spin of the neutron star is neglected because of the maximum simulation time $50\,000\,t_g$ where $t_g = GM/c^3 \simeq 6.90 \times 10^{-6}\,s$ which gives the physical time $\sim 0.35\,s$ i.e. less than the spin period observed for ULXs. Considering that the star is not rotating in our model, I use the Schwarzschild metric:

$$ds^2 = g_{\mu\nu}dx^\mu dx^\nu = -\left(1 - \frac{2GM}{c^2 r}\right)dt^2 + \left(1 - \frac{2GM}{c^2 r}\right)dr^2 + r^2\left(d\theta^2 + \sin^2\theta\, d\phi^2\right). \tag{3.1}$$

The equations are in the units of $G = c = 1$. For the plots, I use units with accretion rate and luminosity in the Eddington unit $L_{\rm Edd}/c^2$ and $L_{\rm Edd}$, respectively. The radius is shown in the units of gravitational radius $r_g = GM/c^2$.

3.2 Study of the impact of dipole strength

I conducted six simulations of accreting neutron stars with dipole magnetic fields, with maximum strengths on the surface of $B_{\rm max} = [1, 2, 3, 5, 7, 10] \times 10^{10}$ G. The simulations were initialized with a torus with the accretion rate exceeding $200\,L_{\rm Edd}/c^2$.

Most of the results presented in this section are based on time-averaged data from $15\,000 - 50\,000\,t_g$. I specify where snapshot data at a specific time are used.

A snapshot of simulations at time $35\,000\,t_g$ is shown in Fig. 3.1, and the time-averaged data is shown in Fig. 3.2. The magnetic field of each simulation is labeled on each frame. The colormaps show the radiation energy density $\hat{E}$ [erg cm^{-3}] in the

[2]Supported by computational grants no. PLG/2023/016648 and no. PLG/2022/015997 and PLG/2021/015167

[3]https://www.visitusers.org/

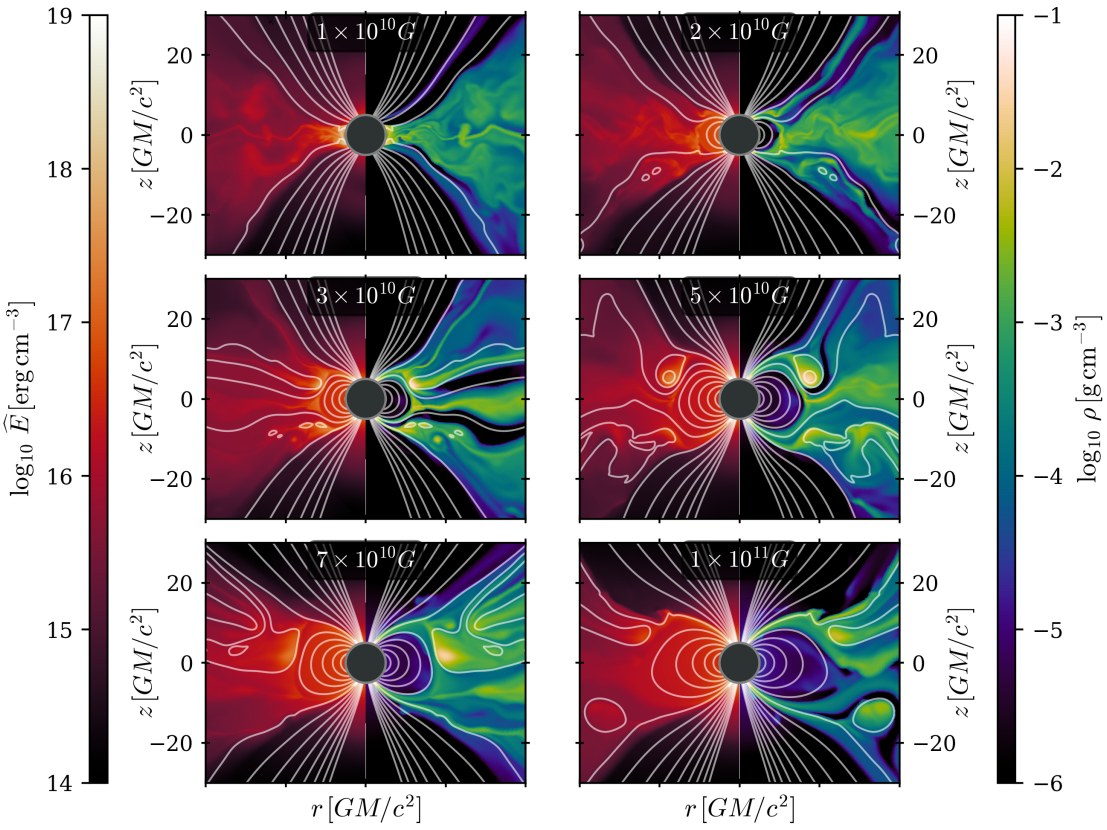

Figure 3.1: Snapshots in the results at time $35\,000\,t_{\rm g}$. The left-half of each panel shows the radiation energy density $\hat{E}$ and the right-half the rest-mass density ρ. Magnetic field lines are plotted as contours of the vector potential, A_ϕ.

left-half panels and the rest-mass density $\rho\,[\mathrm{g\,cm^{-3}}]$ in the right-half panels. The gray contours show the ϕ component of the vector potential, A_ϕ.

As mentioned before, the dipole and magnetic field of the torus are initialized with opposite orientations. During the simulation, the field lines converge and reconnect. Reconnection allows the gas to accrete onto the surface of the neutron star, as shown in the snapshot plots (Fig. 3.1). The magnetic field of the torus is initialized similarly for all simulations. The strength of the dipole determines the radii in which the reconnection occurs. In the simulations with a weak dipole (10^{10} G), most of the dipole lines break, and matter gets very close to the neutron star surface before it follows the field lines. As the dipole strength increases, reconnection happens further from the star. The dipole lines near the star remain unchanged, and matter channels along these lines falls on the neutron star surface close to the polar region. The stream of the dense matter in the midplane and accretion column can be seen in both snapshot and time-averaged plots Figs. 3.1 and 3.2, respectively.

The time-averaged data shown in Fig. 3.2, indicate the trend in the radius where the accretion disk is truncated by the neutron star dipole. The truncation location moves farther away from the neutron star surface as the dipole strength increases. This radius is known as magnetospheric (Alfvén) radius $R_{\rm m}$. I compute $R_{\rm m}$ using the time-averaged data of each simulation where the magnetic and ram pressures are equal in midplane $\theta \sim 90°$. I estimate $R_{\rm m}$ by including the radiation energy density,

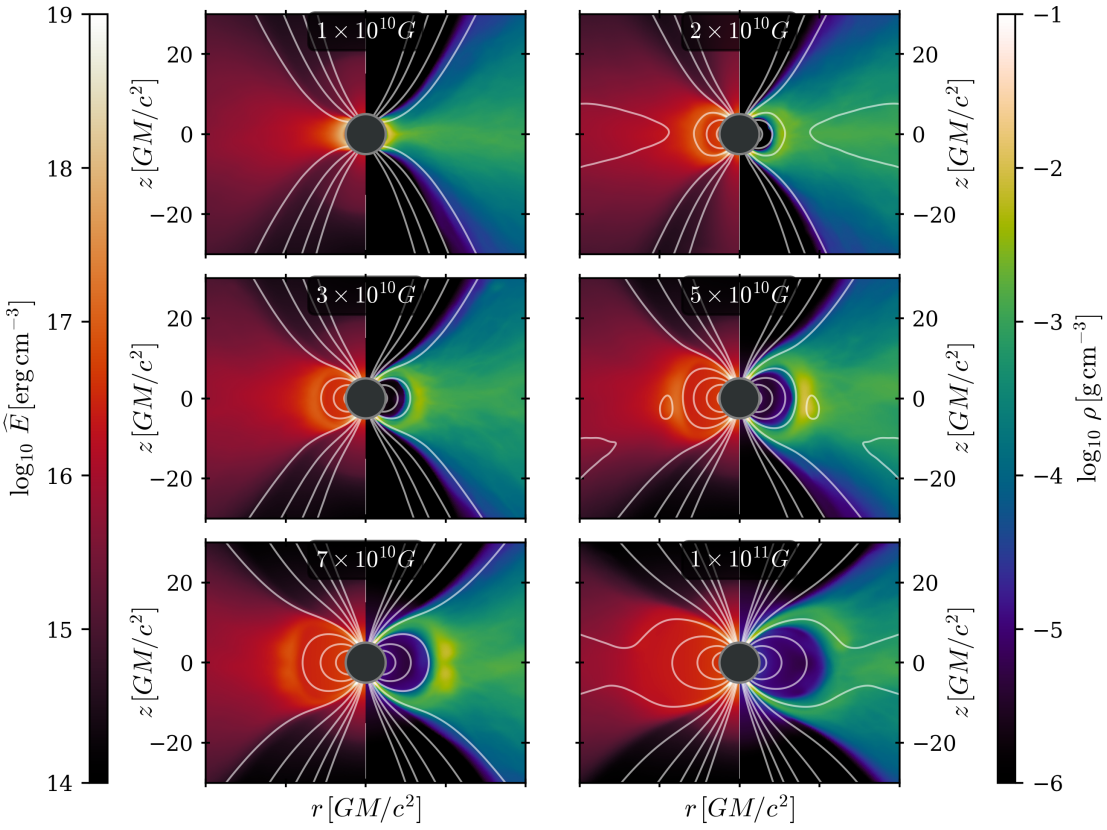

Figure 3.2: The time-averaged data. The left-half of each panel shows the radiation energy density $\hat{E}$ and the right-half the rest-mass density ρ. Magnetic field lines are plotted as contours of the vector potential, A_ϕ.

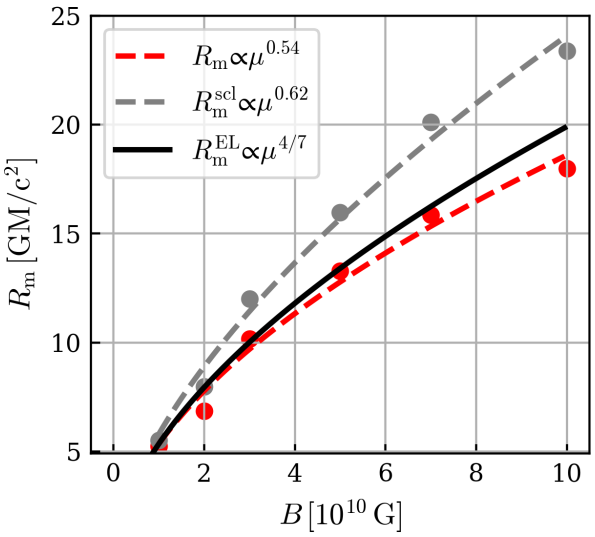

Figure 3.3: The magnetospheric radius as a function of the dipole strength. The red circles are the computed radii in each magnetic field simulation. The gray circles are computed radii of each magnetic field simulation scaled by $\dot{M}^{2/7}$. The red dashed line shows the fitted function on the computed data and the black solid curve corresponds to the analytical solution of Elsner & Lamb (1977).

$$(\rho + \frac{5}{3}u_{\rm int})v^2 + \hat{E} = \frac{B^2}{2}, \tag{3.2}$$

where the Lorentz–Heaviside units are used, i.e. a factor of $1/\sqrt{4\pi}$ is absorbed into the electromagnetic fields.

The magnetospheric radius $R_{\rm m}$ as a function of dipole strength is shown in Fig. 3.3. In this plot, the red circles are the magnetospheric radius, $R_{\rm m}$ is computed from Eq. 3.2. The accretion rate gradually increases with the strength of the dipole of the neutron star (discussed in Section 3.2.1), therefore, I scale $R_{\rm m}$ with $\dot{M}^{2/7}$ based on the analytical solution that shows the magnetospheric radius is proportional to $\dot{M}^{-2/7}$ (see Eq. 1.1). The gray circles in Fig. 3.3 are the scaled values $R_{\rm m}^{\rm scl} = R_{\rm m}\dot{M}^{2/7}$ where $\dot{M}$ is accretion rate in the units of Eddington luminosities. The red and gray dashed lines are the fitted functions on computed values $R_{\rm m}$ and $R_{\rm m}^{\rm scl}$, respectively. I also plot $R_{\rm m}^{\rm EL} \propto \mu^{4/7}$ (Eq. 1.1). According to time-averaged data from six magnetic field simulations, $R_{\rm m}$ as a function of the magnetic field follows the analytical solution $R_{\rm m}^{\rm EL}$ to a good approximation. I previously mentioned that the analytical solution is based on certain assumptions, such as spherical accretion of material along the field lines. However, in my simulations, the accretion process is more complex. The accretion rate is high and the additional source of radiation pressure in the inner part of the accretion disk has an impact on the magnetospheric radius.

Next, I estimate the spherization radius is given by $R_{\rm sph} = 15\dot{m}r_{\rm g}$ ($\dot{m}$ is the accretion rate in Eddington units), which varies between about $240-500\,r_{\rm g}$ from the weakest to the strongest magnetic field simulations. As mentioned in Section 1.1.1, $R_{\rm sph}$ is defined for the geometrically thin accretion disk which is not comparable with the model in my study. Additionally, $R_{\rm sph}$ in my model is located at the torus

in which the accretion is not converged in the simulation time. However, I show that in my simulations at the radii larger than $R_{\rm m}$ there are outflows as it was expected in the KLK model.

3.2.1 Accretion and energy flow

I compute the accretion rate $\dot{M}(r)$, inflow rate $\dot{M}_{\rm in}(r)$, and outflow rate $\dot{M}_{\rm out}(r)$ by integrating momentum density [4] ρu^r over the sphere at each radius of the accretion disk and accretion column. The inflow rate is computed where u^r is negative (flows towards the accretor) and the outflow rate in the opposite direction. The equations are as follows,

$$\dot{M}(r) = -2\pi \int_0^\pi \rho u^r \sqrt{-g} d\theta, \tag{3.3}$$

$$\dot{M}_{\rm in}(r) = -2\pi \int_0^\pi \rho u^r \sqrt{-g} d\theta \Big|_{u^r<0}, \tag{3.4}$$

$$\dot{M}_{\rm out}(r) = 2\pi \int_0^\pi \rho u^r \sqrt{-g} d\theta \Big|_{u^r>0}, \tag{3.5}$$

where we can write $\dot{M} = \dot{M}_{\rm in} - \dot{M}_{\rm out}$, and $\sqrt{-g} = r^2 \sin(\theta)$ is the square root of the metric determinant.

The accretion, inflow, and outflow rates are shown in the top, middle, and bottom panels of Fig. 3.4, respectively. The results of each magnetic field simulation are shown with different colors and line-styles. The radius at which the accretion rate is constant is called the steady-state radius. The time-averaged data of my simulations indicate that within radii less than $50\,r_{\rm g}$, the accretion rate $\dot{M}$ is approximately constant across almost all magnetic fields. However, the steady-state radius moves closer to the star as the magnetic field strength increases. This is likely due to the convergence time in the simulation, with stronger dipoles requiring a longer time for the disk to reach stability. This issue can be addressed by computing the time-averaged data over a longer period in the stronger magnetic field simulations. To compare the simulations and show differences, I used the same length of time-averaged data for all simulations presented here.

In my simulations, the accretion rate increases as the dipole strength increases. This can be addressed by checking inflow and outflow plots. In the presence of the strong dipole, matter is channeled to the strong field lines and most of the material accumulates in the inner radii so that the outflow is not significant. As the magnetic field weakens, more outflows are driven and there is a thick outflow at radii larger than $40\,r_{\rm g}$ that gradually increases to larger radii. However, close to the neutron star, outflow diminishes to zero in all simulations.

Energy flow

The energy flux F^r is computed from plasma energy flux $T^r{}_t$ and radiation energy flux $R^r{}_t$:

$$F^r = -(T^r{}_t + R^r{}_t). \tag{3.6}$$

[4] I remind that ρ is rest-mass density and u^r is the radial component of 4-velocity

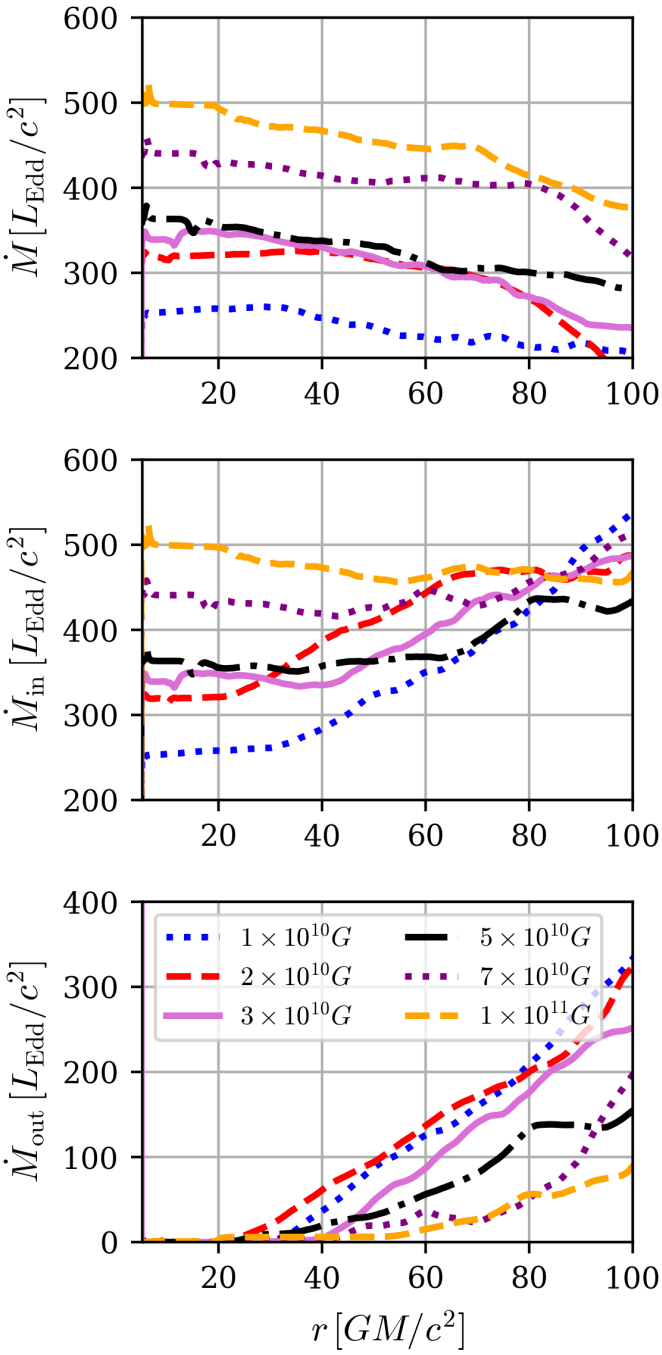

Figure 3.4: The accretion, inflow, and outflow rates are shown in the top, middle, and bottom panels, respectively. Each magnetic field simulation is shown in a different color and line-style.

From the observational point of view, the total flux given in Eq. 3.6 is not an interesting quantity because the gas energy-momentum tensor contains the rest-mass density. To remove the rest-mass density, we add ρu^r to the total energy flux, noting that the lower time index of tensors introduces a negative sign. Thus, the total flux is written as

$$F^r_{\rm tot} = -(T^r{}_t + \rho u^r) - R^r{}_t. \tag{3.7}$$

The radiation flux, denoted with $F^r_{\rm rad} = -R^r{}_t$, reflects the energy carried by radiation which either propagates freely or advects with the gas. The plasma energy flux $T^r{}_t + \rho u^r$ decomposes to different forms of energy flux as follows,

$$\begin{aligned} T^r{}_t + \rho u^r &= (\rho + p + u_{\rm int} + b^2)u^r u_t - b^r b_t + \rho u^r \\ &= \gamma u_{\rm int} u^r u_t + (b^2 u^r u_t - b^r b_t) + \rho u^r (1 + u_t), \end{aligned} \tag{3.8}$$

where pressure is $p = (\gamma - 1)u_{\rm int}$, internal energy is $u_{\rm int}$, $\gamma = 5/3$ is the adiabatic index, u^μ is velocity 4-vector and b^μ is magnetic four-vector (for definition of b^μ see Eq. 1.17). Eq. 3.8 is split into the following equations (Sądowski, Lasota, et al., 2016): the internal energy flux,

$$F^r_{\rm int} = -\gamma u_{\rm int} u^r u_t, \tag{3.9}$$

the magnetic energy flux (for definitions see Section 1.3.3),

$$F^r_{\rm mag} = -(b^2 u^r u_t - b^r b_t), \tag{3.10}$$

and the remaining term in Eq. 3.7 which is called binding energy flux (Sądowski, Lasota, et al., 2016):

$$F^r_{\rm bin} = -\rho u^r (1 + u_t), \tag{3.11}$$

the binding energy flux contains the information about the gravitational and kinetic energy fluxes, respectively, as follows,

$$F^r_{\rm grav} = -\rho u^r (1 - \sqrt{-g_{tt}}), \tag{3.12}$$

$$F^r_{\rm ke} = -\rho u^r (u_t + \sqrt{-g_{tt}}). \tag{3.13}$$

One can also compute the non-relativistic limit of the energy fluxes e.g. the kinetic flux in the Newtonian limit is $\rho v^r v^2/2$, where v^r is the radial component of three-velocity and v^2 is the square of three-velocity.

Next, I compute the luminosity of each energy flux by integrating the corresponding flux over the sphere at each radius,

$$L_{\rm EN} = 2\pi \int_0^\pi F^r_{\rm EN} \sqrt{-g} d\theta, \tag{3.14}$$

where the form of energy flux is defined by index EN. The total luminosity decomposes into the gravitational, kinetic, thermal, magnetic, and radiation luminosity,

$$L_{\rm tot} = L_{\rm grav} + L_{\rm ke} + L_{\rm therm} + L_{\rm mag} + L_{\rm rad}. \tag{3.15}$$

I compute the efficiency of each form of energy output by dividing each luminosity by $\dot{M}c^2$ at the radius $20\,r_{\rm g}$, where the accretion rate in all simulations reaches remains constant. The dimensionless efficiency $\eta = L_{\rm EN}/(\dot{M}c^2)$ for the simulations

with dipole magnetic fields of 10^{10} G and 10^{11} G is shown in Fig. 3.5. From this plot one can infer the radii up to $50\,r_{\rm g}$ where the simulations have converged and the accretion disk is stable. Within these radii, the total energy should remain constant, meaning that energy does not accumulate at any radius of the disk. The blue-solid line in each frame indicates the efficiency of the total luminosity. The total efficiency with a magnetic field of 10^{10} G is approximately ~ 0.08, while in the simulation with a magnetic field of 10^{11} G, it is reduced to approximately ~ 0.03. This suggests that in my simulations, in the presence of a strong dipole magnetic field, accretion is less efficient. This can be attributed to the geometry of the magnetic field in each simulation.

To clarify lower efficiency in the presence of the stronger dipole, I step back and show the snapshots of both magnetic field simulations in Fig. 3.6. Similar to Fig. 3.1, the colormap is the rest-mass density and white contours are vector potential, A_ϕ. Each row corresponds to one magnetic field simulation, with 10^{10} G and 10^{11} G depicted at the top and bottom rows, respectively. Progressing from left to right within each row, snapshots are presented at times $[0, 10\,000, 20\,000, 30\,000\,]\ t_{\rm g}$. The red solid line in each frame is a guideline showing the propagation of the density in each magnetic field simulation. As mentioned in the description of Fig. 3.1, when the simulation starts, dipole and torus field lines interact and reconnect. In the weak dipole, almost all dipole field lines break, and outflows can propagate to high latitudes, as shown in the first row of Fig. 3.6. In contrast, in the presence of a strong dipole, the dipole lines close to the surface remain unchanged material flows along field lines. After reconnection, the strong magnetic field lines close to the neutron star surface keep the outflow at low latitudes and reduce the turbulence. It causes a small efficiency in the presence of a strong dipole.

As material flows toward the accretor, it releases binding energy, while closer to the star the gas becomes more bound. The binding luminosity, represented by the violet-dotted curve in Fig. 3.5, demonstrates this phenomenon. It was shown in Eqs. 3.11 - 3.13, where the gravitational flux is decomposed into binding and kinetic fluxes, shown by the red-dotted and green-dashed lines in Fig. 3.5, respectively.

The negative values in each curve indicate that the proportion of the flux advected inward with the gas is larger than the proportion that is released. This is evident in the curve depicting kinetic efficiency. In radii close to the star, the kinetic efficiency is negative, indicating that the kinetic energy of Keplerian motion is brought inward by the gas. As the radius increases, the kinetic energy diminishes to zero, where the proportions of advected and released kinetic energy are nearly equal. I note that at larger radii, the kinetic efficiency increases to positive values, corresponding to a significant amount of outflows (discussed in Section 3.2.2).

The gray dashed-dotted lines represent the efficiency corresponding to the magnetic luminosity $L_{\rm mag}$. Magnetic energy facilitates the transfer of released energy from the innermost part of the disk and column outward and redistributes this energy to the outer region. In the weak magnetic field simulation, the magnetic luminosity surpasses that of simulations with stronger magnetic fields. In the simulations with a strong magnetic field ingoing and outgoing magnetic fluxes are balanced resulting in a net value that diminishes to zero as depicted in the frame of strong magnetic field simulation (10^{11} G).

Internal energy in each simulation is negligible (brown dashed-dotted line along zero) since radiation cools down the accretion disk. The radiation luminosity, shown

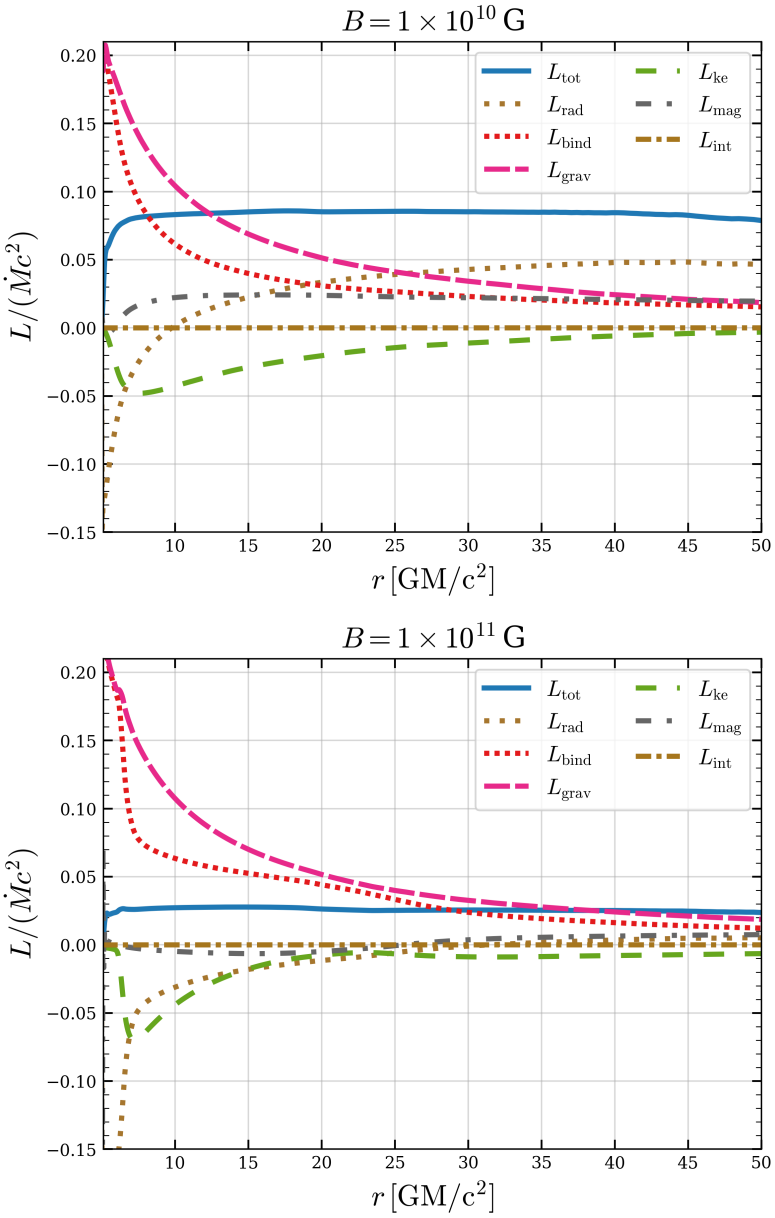

Figure 3.5: The efficiency $L/(\dot{M}c^2)$ of total luminosity and its components for two simulations with dipole 10^{10} G (*top*) and 10^{11} G (*bottom*). Each efficiency is denoted by a different color and line-style.

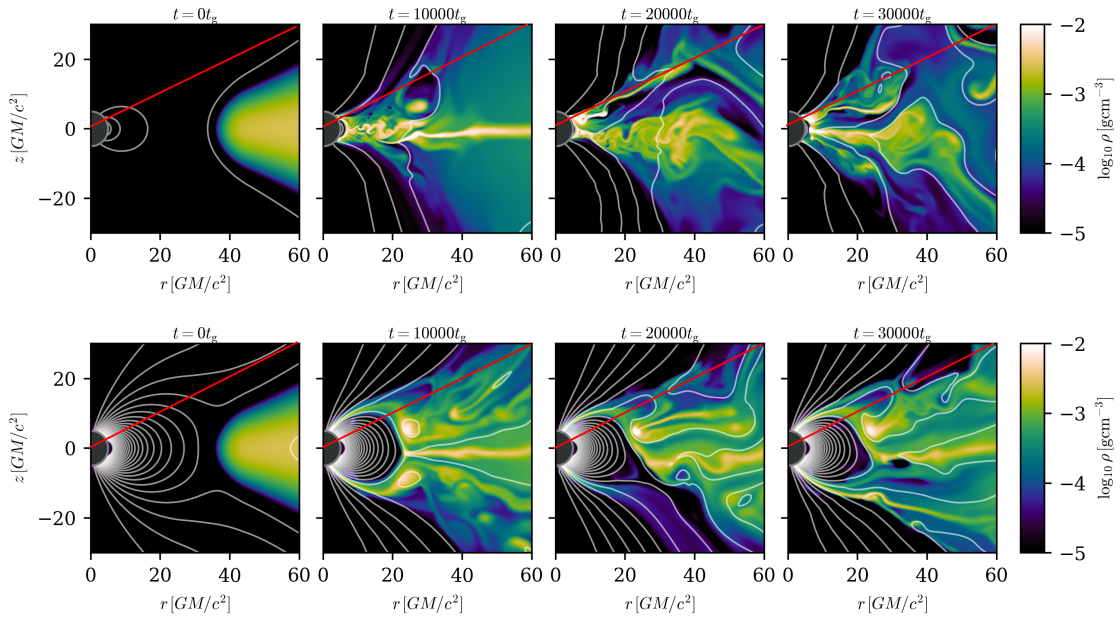

Figure 3.6: The rest-mass density in colormaps and magnetic potential, A_ϕ as contours. Each column shows one snapshot of the labeled time and the top and bottom rows show 10^{10} G and 10^{11} G simulations, respectively. The red solid lines are a guideline to show how material propagates to the higher latitudes in the lower magnetic field simulation.

by the brown dotted curve, reaches negative values close to the neutron star, indicating that most of the radiation is advected with the gas, this is caused by the well-known photon-trapping phenomena (detailed study by Ohsuga, Mineshige, et al., 2002; Sądowski & Narayan, 2016). Radiation luminosity is discussed in detail in Section 3.2.3. However, in the case of the accreting neutron star, the advected radiation is expected to be released on the surface of the neutron star. Here, I use energy-reflective boundary conditions (Abarca, Parfrey, & Kluźniak, 2021) at the surface of the neutron star, despite the numerical challenges inherent in modeling these extreme conditions in this thesis (see the discussions of radial boundary conditions in Section 3.1.2).

3.2.2 Power of the outflow

The outflow of matter is an important phenomenon in the study of ULXs. Early computational predictions were discussed in Section 1.2. Super-Eddington accretion onto the neutron star drives a powerful outflow which causes the collimation of radiation flux and extraordinary apparent luminosity. In this section, I study the kinetic energy carried out by the outflowing gas. The impact of outflow on luminosity is discussed in Section 3.2.3.

In Fig. 3.7 are shown the momentum density, ρu^r multiplied by $2\pi r \sin(\theta)$ in the units of $[L_{\rm Edd} c^{-2} r_{\rm g}^{-1}]$ for three dipole simulations. The streamlines show the direction of the flow. The red dashed line is the zero Bernoulli ($Be = 0$) surface. The relativistic Bernoulli parameter is computed as:

$$Be = -\frac{T^t{}_t + R^t{}_t + \rho u^t}{\rho u^t}, \tag{3.16}$$

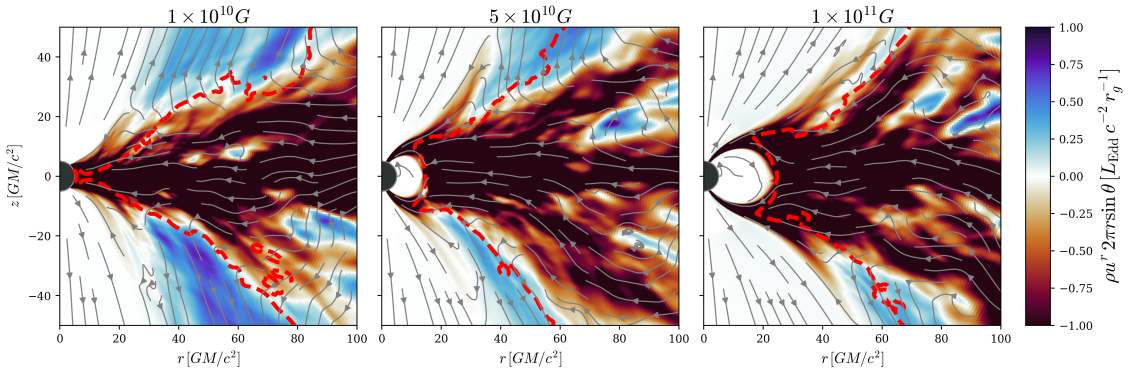

Figure 3.7: The momentum density ρu^r multiplied with $2\pi r \sin(\theta)$ in the units of $[L_{\rm Edd} c^{-2} r_{\rm g}^{-1}]$. The negative values represent inflow and the positive values represent outflow. The red dashed line is the zero Bernoulli surface. The streamlines show the direction of the flow. The magnetic field is labeled above each frame.

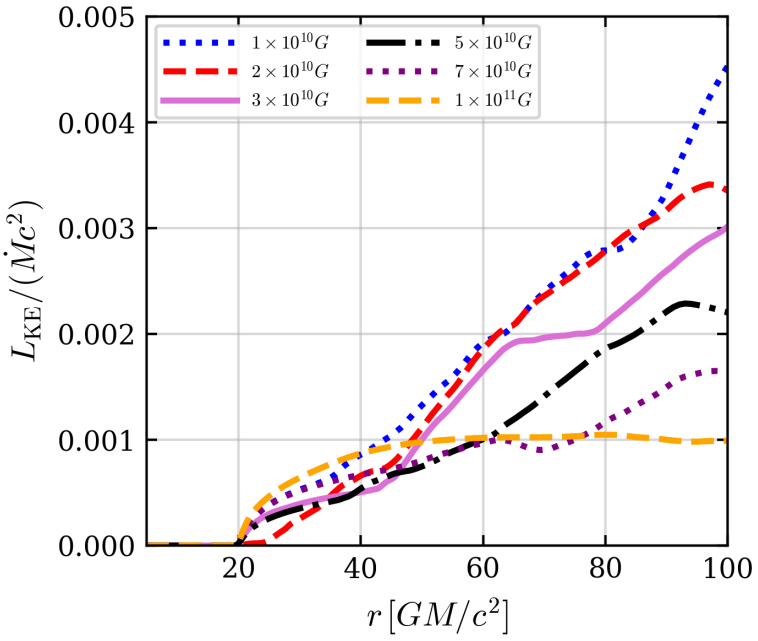

Figure 3.8: The efficiency of outgoing kinetic luminosity computed in outflow region ($Be > 0$, $u^r > 0$). The strength of the dipole in each simulation is shown in a different color and line-style.

with ${T^t}_t$ and ${R^t}_t$ being the MHD and radiation energy densities, respectively. In steady-state Be is zero along the red-dashed line in Fig. 3.7. Above this surface $Be > 0$ the gas is energetic enough to reach infinity on its own. The gas within the zero Bernoulli surface $Be < 0$ is bounded energetically. However, the outgoing gas within this surface still may impact the luminosity.

In Fig. 3.7, the negative values represent in-falling gas, while positive values represent outgoing gas. From left to right panels, the dipole strength increases. In the simulation with a magnetic field of 10^{10} G, the outflow propagates to angles close to the polar axis, resulting in a narrow cone-like optically thin region. The radiation flux escapes towards the observer freely through this region. It is shown that with increasing the strength of the dipole by one order of magnitude (10^{11} G), the outflow decreases, and the cone-like region widens.

The kinetic luminosity of outflows is computed by integrating the outgoing kinetic flux with $Be > 0$,

$$L_{\rm KE} = -2\pi \int (u_t + \sqrt{-g_{tt}})\rho u^r \sqrt{-g} d\theta \Big|_{Be>0,\, u^r>0}. \tag{3.17}$$

The kinetic efficiency of outflows is shown in Fig. 3.8. At the radii $r \geq 60\, r_{\rm g}$, the efficiency of kinetic luminosity increases as the magnetic field weakens. Close to the star, at $r \leq 20\, r_{\rm g}$, there is no outflow and outgoing kinetic energy is zero.

In summary, my simulations show that the power of outflow increases as the dipole weakens. At a radius of $100\, r_{\rm g}$, the efficiency of kinetic luminosity reaches 0.5% for a dipole strength of 10^{10} G. This value is reduced to 0.1% for a dipole of 10^{11} G. In the weak dipole simulation, a thick outflow propagates towards the polar axis of the neutron star, creating a narrow cone-like, optically thin region. This region widens as the dipole strength increases. The impact of dipole strength on the radiation luminosity is discussed in the following section.

3.2.3 Radiative luminosity and beaming emission

The main subject of this thesis is a study of the radiation luminosity. In this section, I compute the radiation luminosity in different regions of the system to clarify how the radiation luminosity is affected by the outflow. Then, I discuss the radiation luminosity in optically thin region that can reach the observer. Finally, I compute the apparent luminosity, which is of interest from the observation point of view.

I start with computing the optical depth in two directions of r and θ, $\tau_{\rm r}$ and τ_θ, respectively, to separate the optically thin and optically thick regions in each direction. The optical depth in r direction is computed as follows,

$$\tau_{\rm r}(r) = \int_r^{r_{\rm out}} \rho \kappa_{\rm es} \sqrt{g_{\rm rr}} dr, \tag{3.18}$$

where $r_{\rm out}$ is the outer boundary of simulations and the optical depth in θ direction is computed as,

$$\tau_\theta(\theta) = \int_0^{\theta} \rho \kappa_{\rm es} \sqrt{g_{\theta\theta}} d\theta, \tag{3.19}$$

where $\kappa_{\rm es} = 0.34\,{\rm cm^2\,g^{-1}}$ is the electron scattering opacity for solar composition and $r_{\rm out}$ the outer boundary of the simulation.

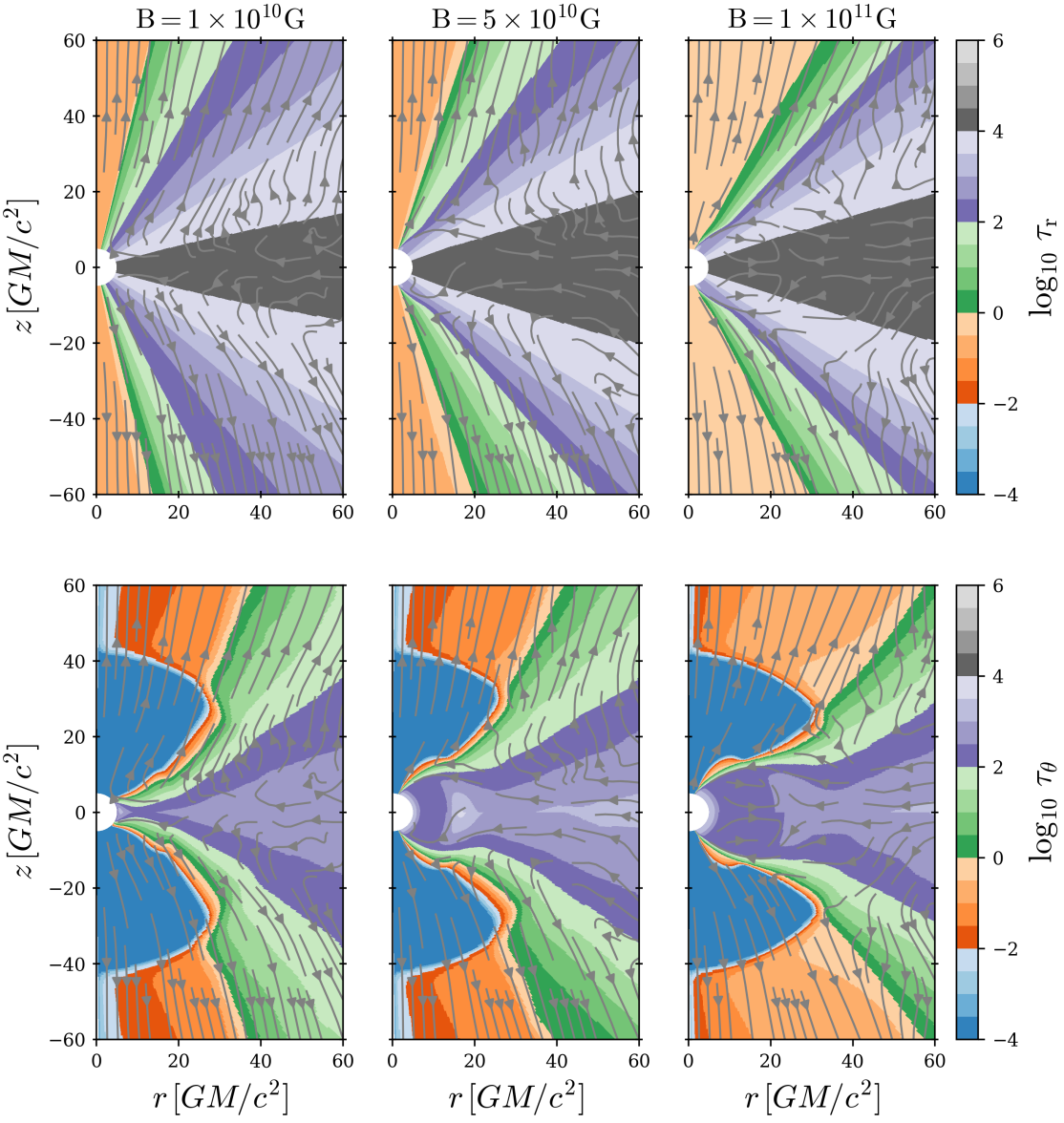

Figure 3.9: The colormaps show optical depth $\tau_{\rm r}$ (*top panels*) and τ_θ (*bottom panels*). Each column shows the simulation results with one dipole strength. The streamlines show the direction of the radiation.

In Fig. 3.9, the optical depth $\tau_{\rm r}$ and τ_θ are shown for three different magnetic field simulations. In the first row, we find that the optical depth $\tau_{\rm r}$ decreases from the equator (along the accretion disk) towards the polar axis. The dark green color in the colormap indicates the value $\tau_{\rm r} = 1$ (photosphere in the radial direction). As discussed in Section 3.2.2, strong outflows create a cone-like optically thin region near the polar axis. This region, depicted in orange in Fig. 3.9, is narrow in the presence of a weak dipole (10^{10} G) and gradually widens as the dipole strength increases. The streamlines illustrate the direction of radiation flux, indicating that in the cone-like, optically thin region, radiation propagates radially outward toward the observer.

In the second row of Fig. 3.9, τ_θ indicate that in the region above the accretion column up to the radius of about $20\,r_{\rm g}$, where there is no outflow (as described in Section 3.2.2) the optical depth is about 10^{-4} (shown with the blue color). This means that radiation can escape from the accretion column freely. The dark-green color in this plot shows the photosphere in the polar direction $\tau_\theta = 1$. The geometry of this line depends on the accretion disk/column structure. From the weak dipole (10^{10} G) to the strong dipole (10^{11} G) polar photosphere widens. The radiation flux direction depicted by streamlines that in the weak dipole (10^{10} G) most of the radiation moves from the optically thick (disk and accretion column) to the optically thin region at each radius while with the strong dipole (10^{11} G) most of the radiation flux at $r \gtrsim 20 r_{\rm g}$ is advected with gas and moves towards the neutron star.

The total luminosity is computed by integrating radiation flux over the polar domain ($0 < \theta < \pi$). The luminosity above the zero Bernoulli surface ($Be > 0$) and luminosity within the photospheres where $\tau_\theta < 1$ and $\tau_{\rm r} < 1$ are computed by integrating radiation flux in each region, respectively,

$$L_{\rm tot} = -2\pi \int_0^\pi R^r{}_t \sqrt{-g} d\theta, \tag{3.20}$$

$$L_{\rm Be} = -2\pi \int R^r{}_t \sqrt{-g} d\theta|_{Be>0}, \tag{3.21}$$

$$L_\theta = -2\pi \int R^r{}_t \sqrt{-g} d\theta|_{\tau_\theta<1}, \tag{3.22}$$

$$L_{\rm r} = -2\pi \int R^r{}_t \sqrt{-g} d\theta|_{\tau_{\rm r}<1}. \tag{3.23}$$

The radiation luminosities for two dipole simulations (1×10^{10} and 1×10^{11} G) are shown in Fig. 3.10. Each simulation is shown in a separate frame, with different colors and line styles representing the various luminosities. $L_{\rm tot}$, L_θ and $L_{\rm Be}$ show negative values at radii close to the neutron star due to the inclusion of radiation flux advected with the gas which is a large proportion of the radiation flux. This is related to the photon-trapping phenomenon (Ohsuga, Mineshige, et al., 2002; Sądowski & Narayan, 2016). The negative values of $L_{\rm tot}$ and $L_{\rm Be}$ occur at a larger radius for the stronger dipole simulation. In the strong magnetic field simulation, along the accretion column at radii $\lesssim 10\,r_{\rm g}$, the magnetic field lines and the stream of accreting material are very dense so that radiation flux is mostly advected with accreting material while in the weak magnetic field simulation, accreting material reaches to the radius very close to the surface of the neutron star. The density of

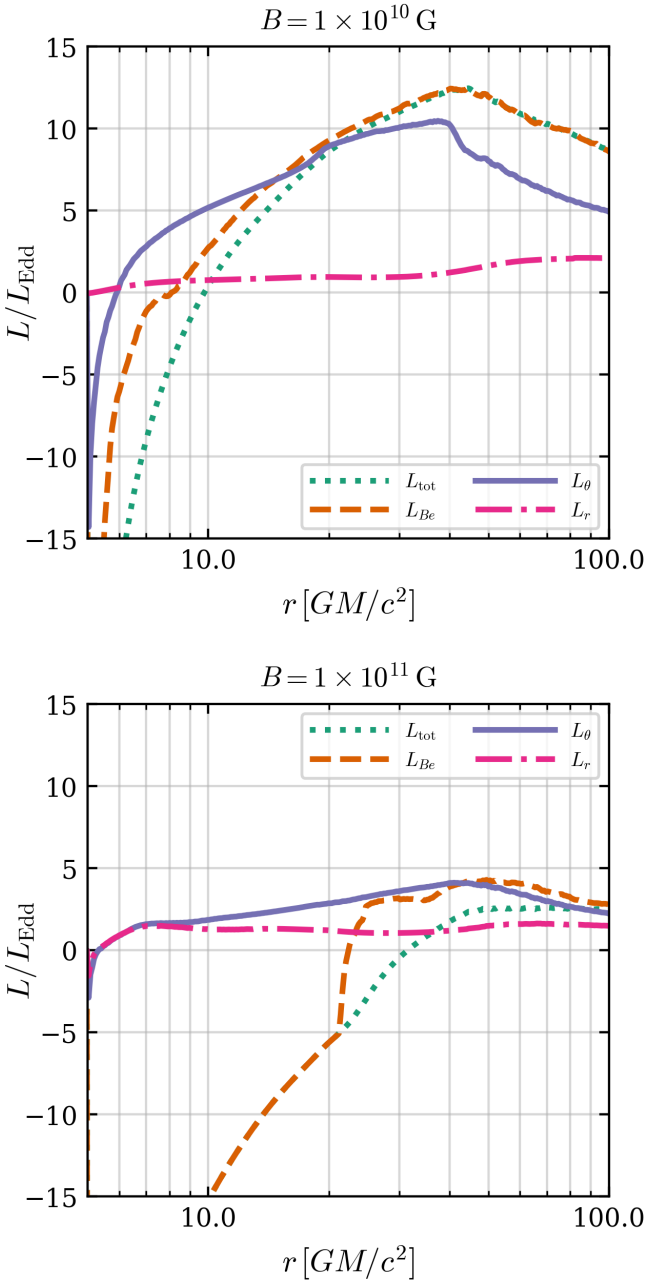

Figure 3.10: The radiation luminosities in two dipole simulations in different regions as introduced in Eq. 3.20 - 3.23. Each luminosity is shown in a different color and line-style. The dipole strength in each simulation is labeled.

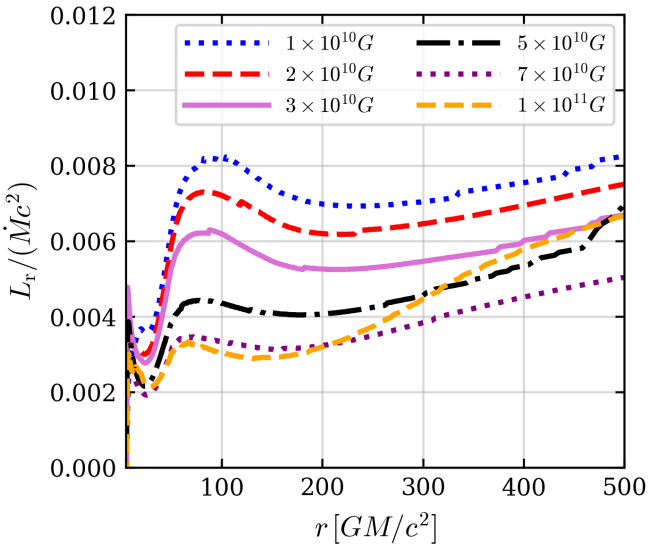

Figure 3.11: Efficiency of radial radiation luminosity $L_r/(\dot{M}c^2)$. L_r is radiation luminosity in the optically thin region $\tau_r < 1$. Each dipole simulation is shown in different colors and line-styles.

accreting material in each magnetic field simulation is shown from snapshot data in Fig. 3.1 and from time-averaged data in Fig. 3.2.

Fig. 3.10 shows that in the innermost radii close to the neutron star, there is a steep rise with radius in luminosities L_r and L_θ, resulting from the radiation shock. L_θ increases up to a radius of $\sim 40\,r_g$, because of the added radiation flux from the accretion disk and column. Beyond $40\,r_g$, where there is an outflow, L_θ decreases. This reduction can be attributed to the momentum transfer of photons to the outflowing gas. Photons interact with the outflowing gas when they pass the outflow region. This process converts the radiation energy into the kinetic energy of the outflows (see the rise in kinetic energy of outflows in Fig. 3.8).

Fig. 3.10 shows that L_r flattens out in both dipole simulations. L_r represents the maximum radiation released from each dipole simulation and is expected to reach the observer depending on their viewing angle (neglecting cosmological effects). The value of L_r is approximately $2.5\,L_{Edd}$ in the simulation with a dipole strength 10^{10} G and about $1\,L_{Edd}$ in the simulation with a dipole strength 10^{11} G. The reason for the low luminosity in the strong dipole simulation is discussed in the description of Fig. 3.6 in the subsection of 'Energy flow', where I discussed the low efficiency of simulation with the strong dipole.

As shown in Fig. 3.9, radiation in the optically thin cone-like region ($\tau_r < 1$) moves out of the accretion disk and column. This radiation may reach the observer depending on their viewing angle. I have already demonstrated that this luminosity decreases with increasing dipole strength in Fig. 3.10. However, the accretion rate in each simulation is different. To illustrate the trend of luminosity variation with respect to dipole strength, I have plotted $L_r/(\dot{M}c^2)$ for each magnetic field simulation in Fig. 3.11. There we see that the efficiency of radiation in the optically thin region ($\tau_r < 1$) reaches a maximum of about 0.08% in the weak dipole (10^{10} G) and decreases with increasing dipole strength to slightly less than 0.04% for the strong dipole (10^{11} G), at a radius of about $40\,r_g$. The curves then flatten out at a

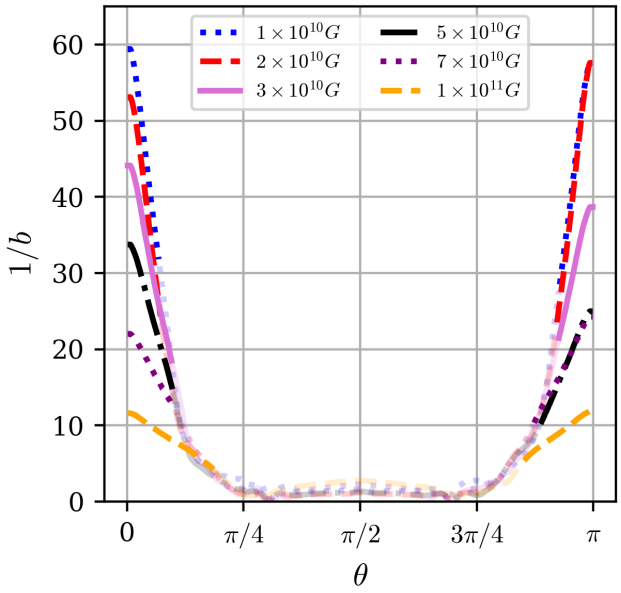

Figure 3.12: Parameter $1/b$ as a function of the viewing angle. Each dipole simulation is shown in different colors and line-styles. The faded color indicates the optically thick region within the disk.

radius depending on the dipole strength of each simulation. Beyond radii of about $200\,r_{\rm g}$, the radiation increases, most likely due to the curvature of the photosphere at larger radii, at which more radiation flux sinks to the optically thin region. This increase in radiation is significant in the strong dipole simulation 10^{11} G resulting in the efficiency of radiation rising to $\sim 0.07\%$.

The most interesting parameter from an observational perspective is the apparent or isotropic luminosity, $L_{\rm iso}$. We can compute $L_{\rm iso}$ using the formula $L_{\rm iso}(\theta) = 4\pi d^2 F^r_{\rm rad}$, where d is the distance between the observer and the object, and $F^r_{\rm rad}$ is the radiation flux in the optically thin region ($\tau_{\rm r} < 1$). In numerical simulations, $L_{\rm iso}$ can be calculated at arbitrary distances. In this thesis, I compute this parameter up to the outer radius of the initial torus, $500\,r_{\rm g}$. As I mentioned in Section 1.2, the isotropic luminosity is a factor of $1/b$ of the true luminosity, L: $L_{\rm iso} \sim L/b$. When $b \ll 1$, the observer overestimates the true luminosity and the accreting X-ray source might appear as an ULX.

In Fig. 3.12, I plot $L_{\rm iso}(\theta)/L_{\rm r} \equiv 1/b(\theta)$ versus θ for each magnetic field simulation. The beaming b reaches its minimum values at angles close to the polar axis (0 and π). At large viewing angles (approximately $\pi/4 \leq \theta \leq 3\pi/4$) the faded color lines indicate the optically thick region within the disk where the radiation flux cannot reach the observer. The beaming factor increases with dipole strength. The minimum beaming factor is approximately $1/60 \simeq 0.017$ for the dipole strength 10^{10} G, and is about $1/12 \simeq 0.08$ for the dipole 10^{11} G. These values are comparable to the beaming factor estimated in KLK model (King & Lasota, 2020), which ranges from 0.009 to 0.6. However, my model here is not directly comparable with the analytical model of KLK because of the distance between the magnetospheric and spherization radius as discussed in Section 1.2.1.

In Fig. 3.13, is shown the apparent (isotropic) luminosity $L_{\rm iso}(\theta)$ in the unit of $L_{\rm Edd}$ for each magnetic field simulation. The left and bottom axes display the

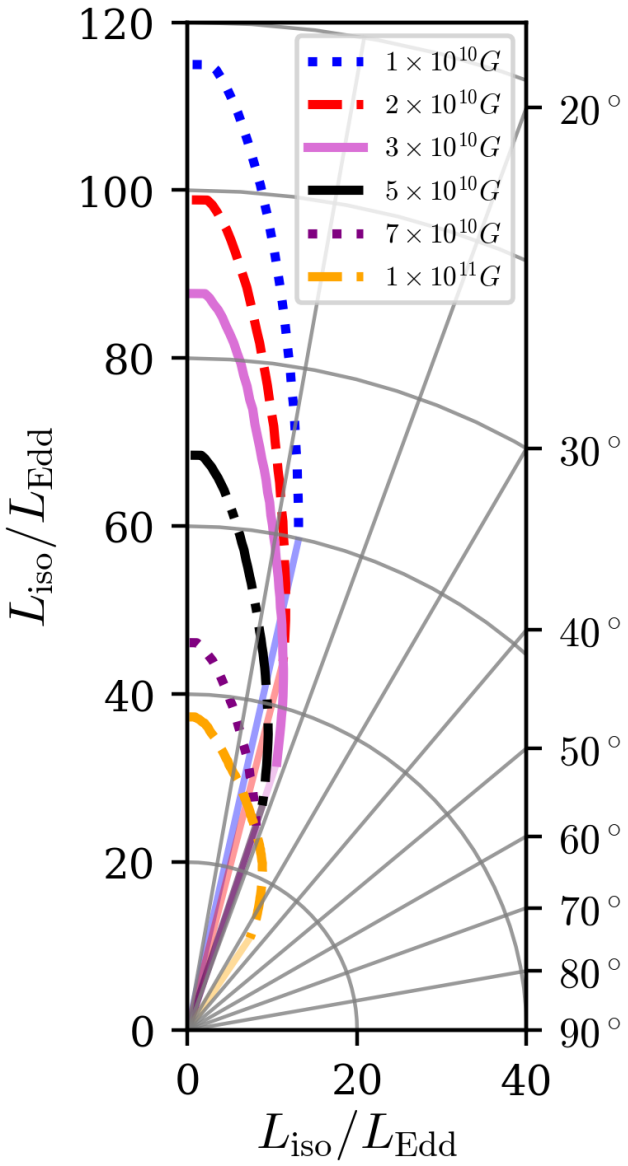

Figure 3.13: Isotropic luminosity in the unit of $L_{\rm Edd}$ in polar coordinates. With right axis show viewing angles. The straight gray solid lines correspond to particular viewing angles. The faded straight line in each magnetic field curve represents the optically thick region at which the radiation flux diminishes to zero.

value of $L_{\rm iso}$ and viewing angles are shown with gray solid straight lines. Most of the radiation flux is concentrated at angles less than $\sim 15°$, with the isotropic luminosity peaking at the polar axis. A weak dipole magnetic field causes the high isotropic luminosity due to collimation by the strong outflow, which creates a narrow cone-like optically thin region near the polar axis (see Fig. 3.9). Along the angle of the optically thick region within the disk, where radiation flux cannot reach the observer, $L_{\rm iso}$ drops to zero. This angle varies with the dipole strength, e.g. for the weak dipole simulation (10^{10} G), it is about 15°, while for the strong dipole simulation (10^{11} G), it is about 35°. Following the faded color solid lines, one can find the angle for each magnetic field simulation.

The main takeaway of this section is that weakly magnetized neutron stars with dipole strengths in the order of 10^{10} G accreting above the Eddington limit can produce isotropic luminosities consistent with those observed in ULXs. Notably, the simulation with the weakest dipole (10^{10} G) results in the highest apparent luminosity while the accretion rate in the presence of this magnetic field is lower than the one in the stronger magnetic field simulations. This result has been prepared as *"Astrophysical Journal Letter"* and the paper is attached to this thesis in Chapter 4.

It is challenging to perform simulations with 10^9 G magnetic field and to determine whether they would lead to a beamed emission consistent with ULXs. Some improvements in the code are required for such confirmation. Abarca, Kluźniak, & Sądowski (2018) showed that in non-magnetized neutron stars the radiation is not beamed even when accreting at super-Eddington rates. With stronger magnetic fields ($> 10^{11}$ G), the beaming factor decreases.

3.3 Study of the impact of accretion rate

In this section, I discuss the impact of super-Eddington accretion rate on the luminosity and beamed emission of accreting neutron stars. I vary the accretion rate for two dipole strengths of neutron stars presented in the previous section (10^{10} G and 3×10^{10} G). These strengths were chosen based on the results of Section 3.2.3, where the apparent luminosities with such magnetic fields exceed $90\,L_{\rm Edd}$ and the minimum beaming factor was ~ 0.02. I compare simulations with accretion rates of $\sim [100, 300, 1000]\,L_{\rm Edd}c^{-2}$.

In this section, most of the results are computed using the time-averaged data from $15\,000 - 40\,000\,t_{\rm g}$. I will specify instances where snapshots at specific times are used. In the line plots the magnetic field is denoted by line-style and accretion rates are labeled as $\dot{M}_{100}$, $\dot{M}_{300}$, and $\dot{M}_{1000}$ using different colors.

In Fig. 3.14 are plotted the radiation energy density in the left-half panels and the rest-mass density in the right-half panels using the snapshot data at time $30\,000\,t_{\rm g}$. Each column shows the results with one magnetic field, 3×10^{10} G and 1×10^{10} G on the left and right panels, respectively. Each row represents one accretion rate increasing from top to bottom as labeled. It is shown that the plasma propagates to higher latitudes with increasing accretion rates. The stream of gas in the accretion disk and column increases in density with respect to the accretion rate from the top to the bottom. From left to right panels in each row, it is obvious that in the stronger magnetic field simulation (left column) more dipole lines remain unchanged after the interaction of field lines and reconnection. Additionally, in the weaker magnetic field, gas propagates to "slightly" higher latitudes compared to the stronger magnetic

field. As a result, the high accretion rate $\dot{M}_{1000}$ in the presence of the weak dipole (10^{10} G) causes the radiation energy to be strongly collimated in comparison to the other simulations.

In Fig. 3.15 are shown the time-averaged data in the range of $15\,000 - 40\,000\,t_{\rm g}$. Consistent with the findings from Fig. 3.14, the radiation becomes more collimated as the accretion rate increases and the dipole strength decreases. Fig. 3.15 also illustrates the impact of both accretion rate and dipole strength on the radius at which the disk is truncated. In each dipole simulation, the truncation radius decreases with increasing accretion rate.

3.3.1 Accretion disk and column

I compute the magnetospheric radius $R_{\rm m}$ using Eq. 3.2. Fig. 3.16 shows the $R_{\rm m}$ versus the accretion rate in each magnetic field simulation presented in this section. The red circles show the results of the simulation with dipole strength 3×10^{10} G, and the blue circles indicate the results of the simulations with dipole strength 1×10^{10} G. The gray dashed lines are the fitted functions to the results of each magnetic field simulation. With the stronger magnetic field $R_{\rm m} \propto \dot{M}^{-0.17}$ and in the weaker magnetic field $R_{\rm m} \propto \dot{M}^{-0.02}$. The black solid line shows $R_{\rm m}^{\rm EL} \propto \dot{M}^{-2/7}$ that corresponds to the analytical solution (see Eq. 1.1 in Section 1.1.1). $R_{\rm m}$ in each magnetic field simulation decreases with respect to the accretion rate. In the stronger magnetic field simulation, $R_{\rm m}$ changes less steeply than the analytical solution. One reason that may explain this difference between the analytical solution and numerical simulation is the additional source of pressure from radiation. This pressure is more significant with higher accretion rates. In the weak magnetic field simulation (10^{10} G), at these high accretion rates, the magnetosphere is very close to the surface of the neutron star and can not be smaller with increasing the accretion rate, i.e. $R_{\rm m}$ remains nearly constant as a function of accretion rate.

The accretion, inflow, and outflow rates are computed using Eqs. 3.3 to 3.5 and are presented in the top, middle, and bottom panels in Fig. 3.17. The plot indicates that the accretion rate is slightly higher in stronger magnetic field simulation, as discussed in Section 3.2.1. The figure shows that simulations reach the steady-state at the radius $100\,r_{\rm g}$, except for the simulations with a high accretion rate ($1000\,L_{\rm Edd}c^{-2}$), where the steady-state radius is approximately $60\,r_{\rm g}$ (as shown in the top panel). The outflow rate strongly increases with the accretion rate. Additionally, the figure illustrates that the location of outflows moves farther from the neutron star as the accretion rate decreases.

3.3.2 Power of the outflow

In Fig. 3.18 is displayed the momentum density ρu^r multiplied by $2\pi r \sin(\theta)$ in units of $[L_{\rm Edd}c^{-2}r_{\rm g}^{-1}]$. The top row corresponds to the simulations with a stronger magnetic field (3×10^{10} G) and the bottom row corresponds to the simulations with a weaker magnetic field (1×10^{10} G). The streamlines show the direction of flow. In the colormaps the negative values denote ingoing flow and the positive values indicate the opposite direction. The red dashed line in each panel is the zero Bernoulli surface. Each column presents the results of a different accretion model labeled. From left to right, increasing the accretion rate results in enhanced outflows. High

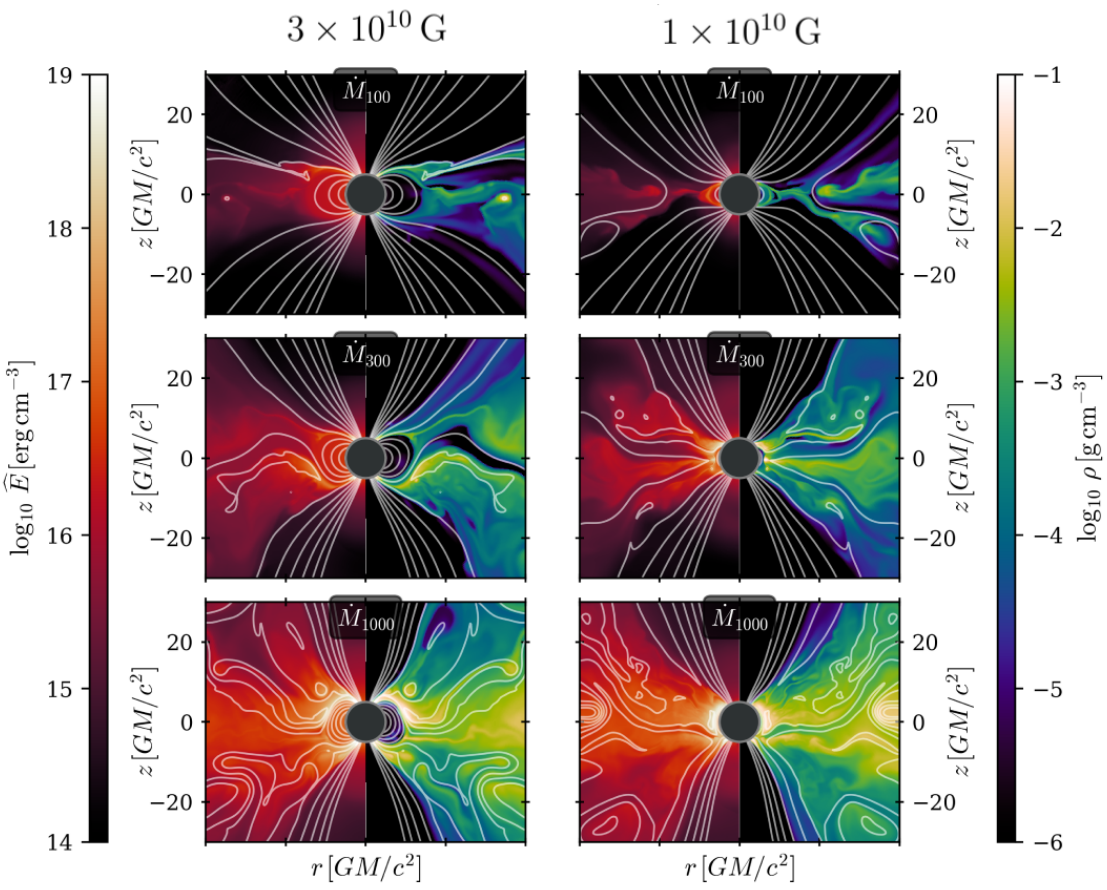

Figure 3.14: Snapshot in simulations at time $30\,000\,t_{\mathrm{g}}$. The left-half of each panel shows the radiation energy density $\hat{E}$ and the right-half the rest-mass density ρ. Magnetic field lines are plotted as contours of the vector potential, A_ϕ. The left column shows the simulation with 3×10^{10} G and the right column with 1×10^{10} G.

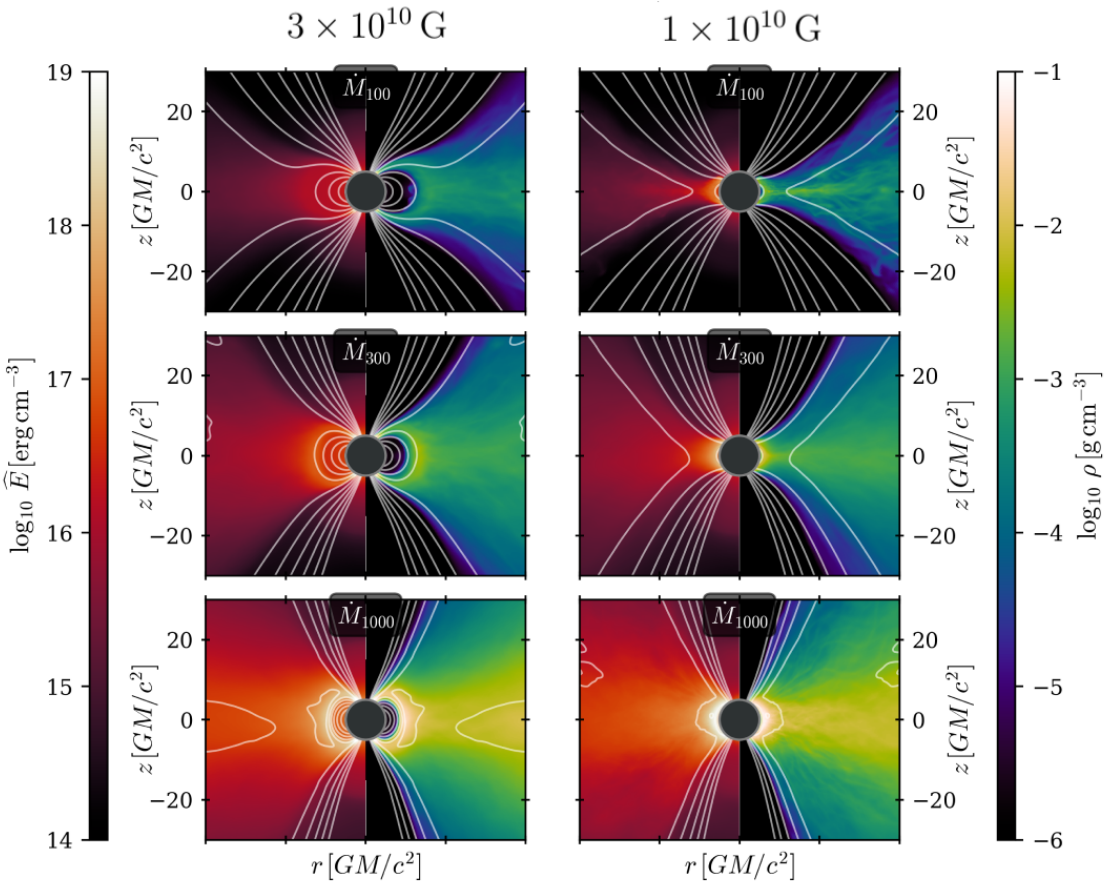

Figure 3.15: The time-averaged data. The left-half of each panel shows the radiation energy density $\hat{E}$ and the right-half the rest-mass density ρ. Magnetic field lines are plotted as contours of the vector potential, A_ϕ. The left column shows the simulation with 3×10^{10} G and the right column with 1×10^{10} G.

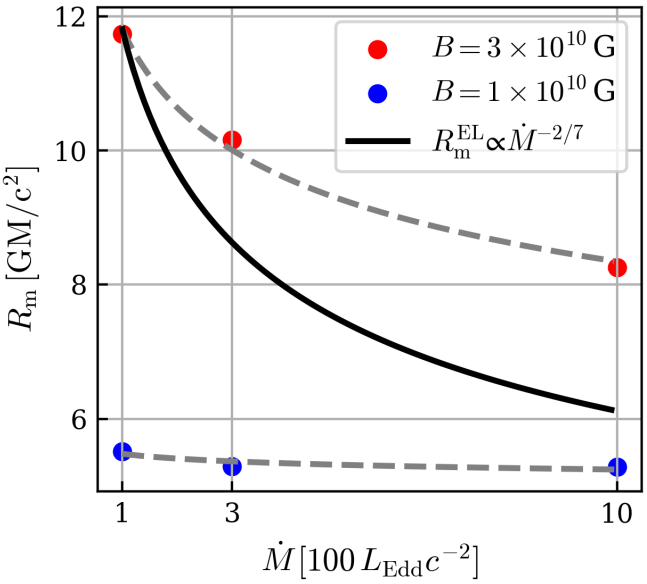

Figure 3.16: The magnetospheric radius of each simulation with different magnetic field and accretion rate. Each color represents one magnetic field simulation. The dashed gray lines are fitted functions and the solid black line corresponds to the Elsner-Lamb analytical solution, Eq. 1.1.

accretion rate $\dot{M}_{1000}$ simulations exhibit strong outflows. Additionally, a weaker magnetic field correlates with stronger outflows.

In Fig. 3.19, the radiation flux is presented in the left-half panel, and the kinetic flux is displayed in the right-half panel for three different accretion rates in a simulation with 10^{10} G. The radiation fluxes are multiplied with $2\pi \sin(\theta)$ and shown in the units of $[L_{\rm Edd} r_{\rm g}^{-1}]$. The solid green contour represents the photosphere, calculated using Eq. 3.18 ($\tau_{\rm r} = 1$). The red-dashed lines indicate the zero Bernoulli surface, while the gray-dashed lines denote the viewing angles that are labeled. This figure illustrates the increasing power of the outflow with respect to the accretion rate, as shown in the right-half panels. The outflows propagate towards angles close to the polar axis. The angle is approximately 12° in the model with the highest accretion rate ($\dot{M}_{1000}$). The surface of the photosphere cone ($\tau_{\rm r} = 1$) is positioned at the same angle relative to the axis. The photosphere broadens as the accretion rate decreases. Additionally, it is evident that the higher accretion rate model shows a greater radiation flux compared to the lower accretion rate model.

Fig. 3.20 shows the efficiency of the kinetic luminosity in each simulation computed by Eq. 3.17. As expected, the kinetic efficiency decreases with increasing magnetic field and with decreasing the accretion rate. The efficiency of kinetic luminosity reaches 0.7% in the highest accretion rate ($\dot{M}_{1000}$) in the presence of a weak dipole (10^{10} G). In the lowest accretion rate ($\dot{M}_{100}$) it is below 0.2% in both magnetic field simulations.

3.3.3 Radiative luminosity and beaming emission

Before computing the luminosity, the optical depth in r and θ directions are computed using Eqs. 3.18 and 3.19, respectively. In Section 3.2.3 is explored the impact

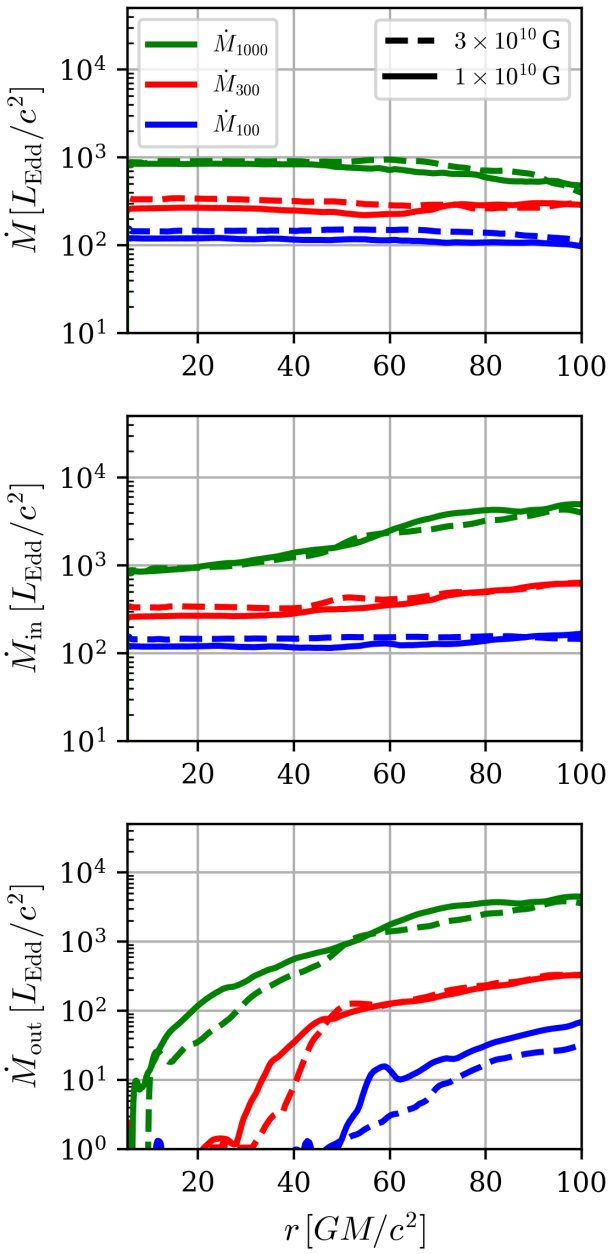

Figure 3.17: Net accretion rate (*top panel*), inflows rate (*middle panel*) and outflows rate (*bottom panel*).

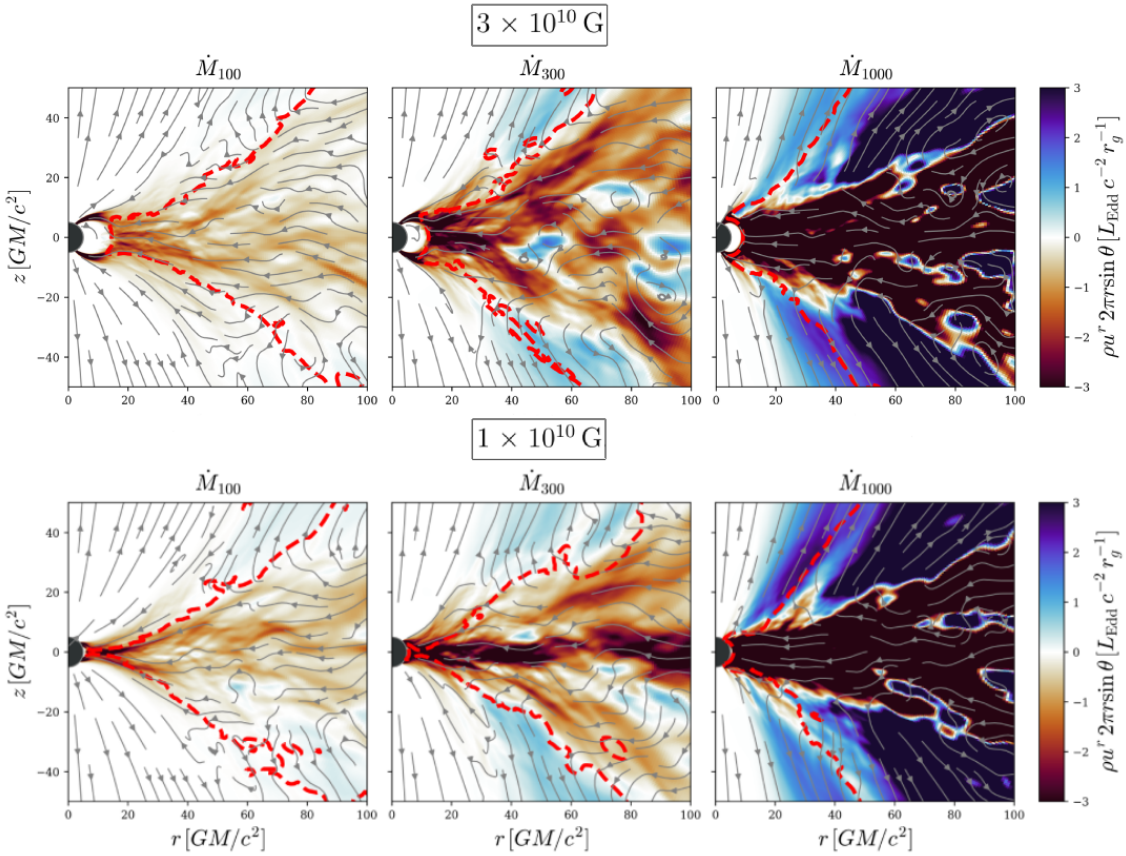

Figure 3.18: The momentum density times $2\pi r \sin(\theta)$ in the units of $[L_{\rm Edd}c^{-2}r_{\rm g}^{-1}]$. The negative values are inflow and the positive values are outflow. The red dashed line is the zero Bernoulli surface. The first row represents the results of 3×10^{10} G and the second row 1×10^{10} G. Each column represents the momentum density of one accretion rate simulation as labeled.

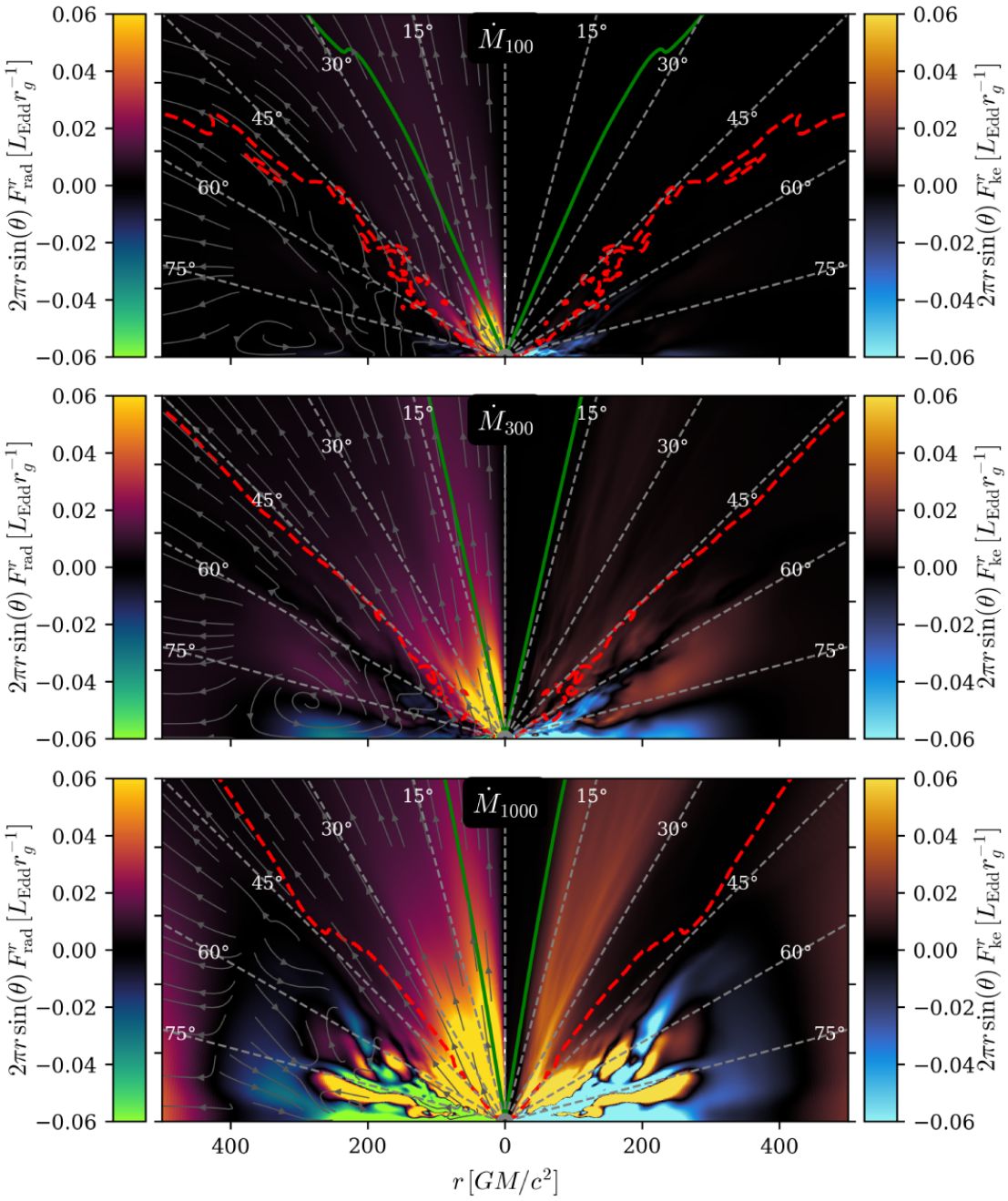

Figure 3.19: The radiation flux (*left*) and kinetic flux (*right*) for three different accretion rates which are labeled for the simulations of the dipole strength 10^{10} G. The gray dashed lines show the viewing angles and the red-dashed line and green solid lines are zero Bernoulli surface and photosphere ($\tau_{\rm r} = 1$), respectively.

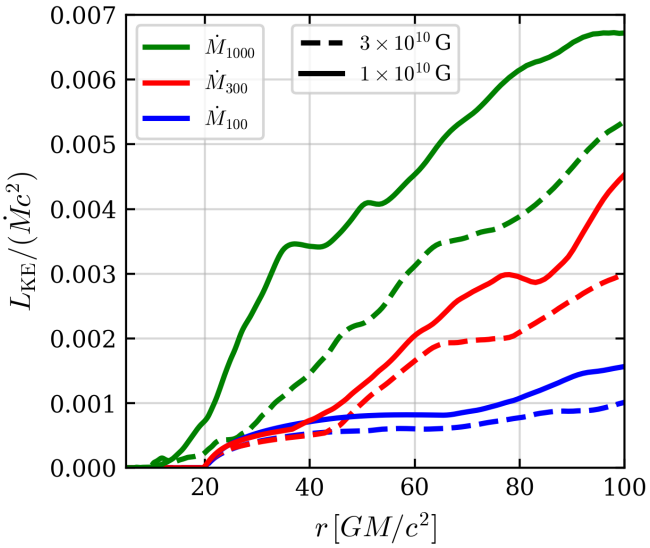

Figure 3.20: The efficiency of outgoing kinetic luminosity computed in the outflow region ($Be > 0$, $u^r > 0$).

of magnetic fields on optical depth due to outflows. Here I discuss the impact of the accretion rate on the optical depths.

The computed optical depths for each accretion rate in the simulation of 10^{10} G are depicted in Fig. 3.21. Increasing the accretion rate results in an increase in $\tau_{\rm r}$ within the disk. The optically thick regions with $\tau_{\rm r} > 1$ extend to higher latitudes in simulations with higher accretion rates. The dark green color in each panel of the first row indicates an optical depth $\tau_{\rm r} = 1$, which is shifted by increasing the accretion rate towards the polar axis from the left panel to the right panel. Consequently, the optically thin cone-like region (shown in orange color) becomes more narrow with increasing accretion rate, as also shown in Fig. 3.19. The polar optical depth is shown in the second row of Fig. 3.21. The dark green color demonstrates that the position of the photosphere ($\tau_\theta = 1$) changes with the accretion rate. The figure demonstrates the optically thin region above the accretion funnel (shown with the blue color) widens with a decrease in the accretion rate as a result of the decrease in outflows.

In Fig. 3.21 we trace the streamlines to determine the direction of radiation flux. It is observed that in simulations with high accretion rates, where the optical depth within the disk is high, the radiation flux primarily advects with the flow towards the neutron star. Conversely, in simulations with low accretion rates, at each radius, the radiation flux moves out to the optically thin region.

The radiation fluxes within the optically thin region $\tau_{\rm r} < 1$ may be detectable by the observer. To analyze the simulations, the radiation luminosity in the optically thin region is computed using Eq. 3.23. The efficiency of radiation is $L_{\rm r}/(\dot{M}c^2)$ with $\dot{M}$ computed at radius $50\,r_{\rm g}$. In Fig. 3.22 is illustrated the radiation efficiency of each magnetic field and accretion rate simulation. As it is also discussed in Section 3.2.3, weaker dipole fields (10^{10} G) result in higher radiation efficiency. It is observed that a high accretion rate corresponds to low efficiency. In the high accretion rate there is a significant outflow, when photons pass through the tick outflow, they interact with outflowing material and transfer their momentum. This interaction lowers the

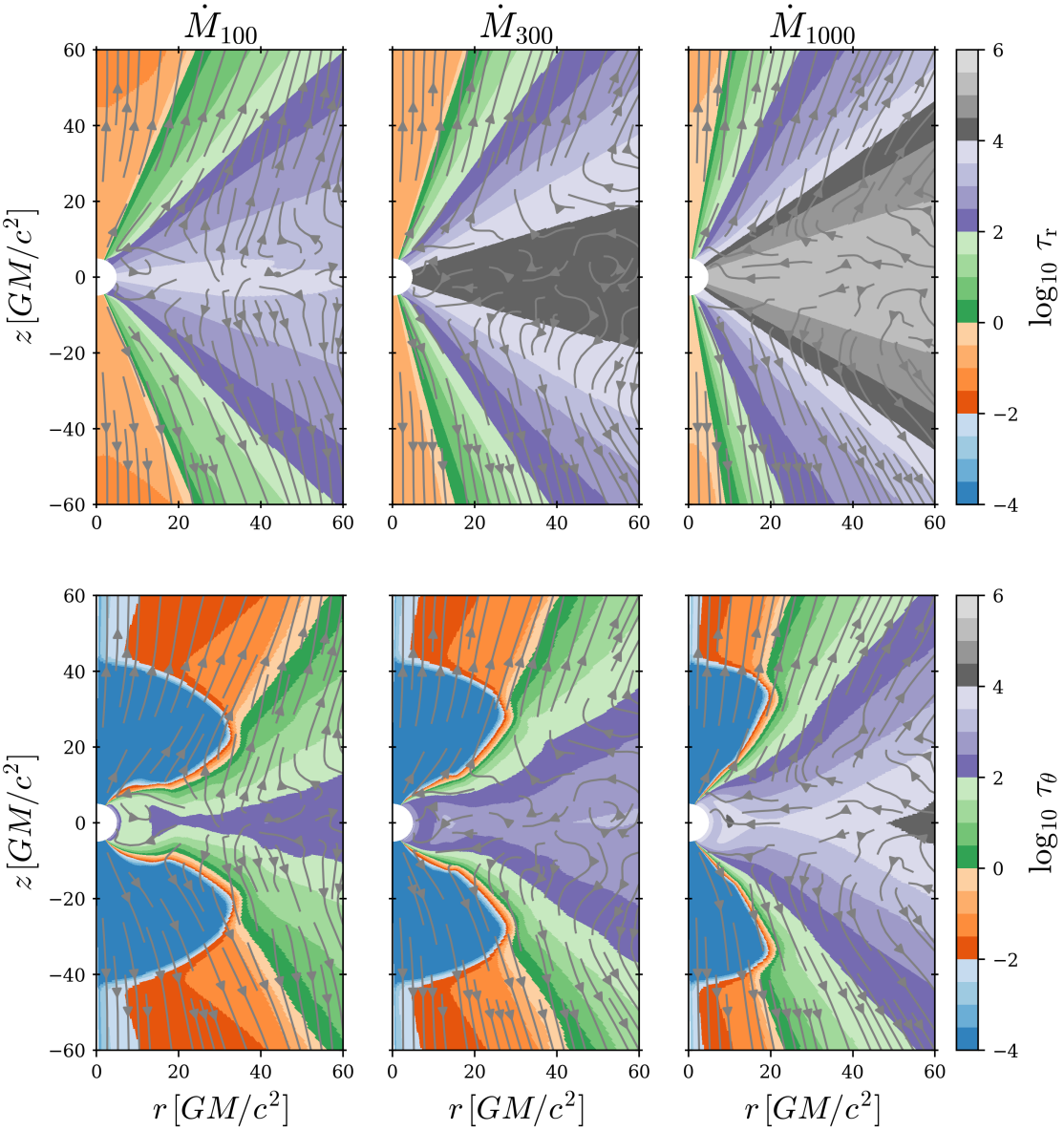

Figure 3.21: The colormaps show optical depth $\tau_{\rm r}$ (*top panels*) and τ_θ (*bottom panels*) for magnetic field 10^{10} G. The streamlines show radiation direction. Each column represents one accretion rate which is labeled.

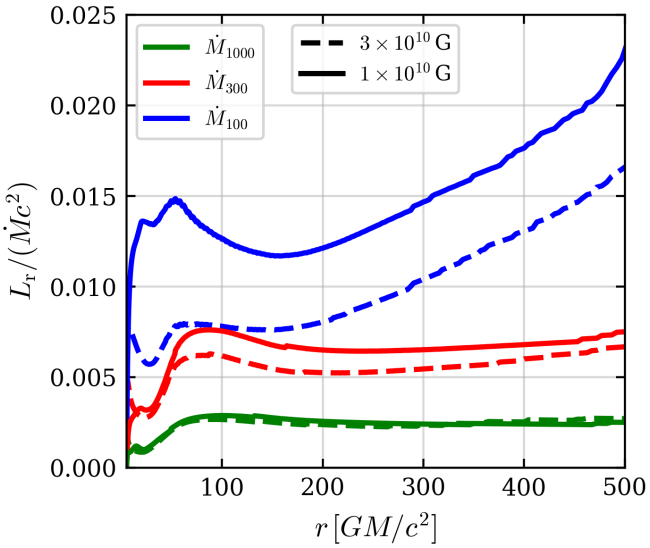

Figure 3.22: Efficiency of radiation luminosity $L_r/(\dot{M}c^2)$. L_r is radiation luminosity in the optically thin region $\tau_r < 1$.

radiation efficiency and increases the kinetic efficiency (see Fig. 3.20).

In Fig. 3.22, radiation efficiency increases up to radii of approximately $50\,r_g$, including the radiation flux released from the accretion column and disk. Subsequently, it decreases up to radii approximately $200\,r_g$, attributed to the interaction of photons with the outflows, resulting in reduced radiation energy and increased kinetic energy of the outflowing gas. With low accretion rate simulations $\dot{M}_{100}$ and $\dot{M}_{300}$ there is an increase in the radiation efficiency up to a radius of $500\,r_g$. This increase is more pronounced in simulations $\dot{M}_{100}$. This increase is most likely attributed to the geometry of the photosphere. The curvature in the photosphere $\tau_r = 1$ at large radii causes the radiation from the optically thick region to escape into the optically thin region.

Fig. 3.22 shows that in simulations with high accretion rate $\dot{M}_{1000}$, the optical depth does not significantly change even at large radii, resulting in a constant radiation efficiency. The radiation efficiency of simulations with high accretion rate in both magnetic field simulations is similar, indicating that the effect of accretion rate dominates over the effect of the magnetic field on the radiation efficiency. The impact of the magnetic field on the efficiency is discussed in Section 3.2.3.

Fig. 3.22 indicates that the radiation efficiency for each accretion rate in simulations of 10^{10} G is 0.25%, 0.7%, and 2.5% from high to low accretion rates, respectively. This value for the stronger magnetic field 3×10^{10} G is 0.25%, 0.65%, and 1.6% from the high to the low accretion rates, respectively.

Next, I compute the beaming factor and apparent luminosity which are the important parameters from the observational perspective. These computations are similar to those in Section 3.2.3. The factor $1/b(\theta)$ can be computed by dividing $L_{iso}(\theta) = 4\pi d^2 F^r_{rad}$ by the actual luminosity L_r (the radiation luminosity in optically thin region, $\tau_r < 1$). In Fig. 3.23 is shown the beaming factor as $1/b$ versus θ for each simulation. It is shown that the beaming factor b varies between 0.05 and 0.008 in the simulation with 10^{10} G and between 0.05 to 0.01 in the simulation with 3×10^{10} G, both from the low to high accretion rate.

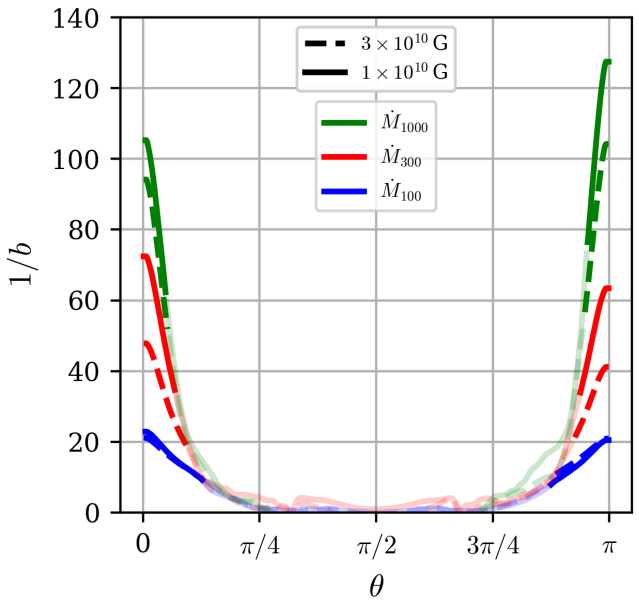

Figure 3.23: Parameter $1/b$ as a function of the viewing angle for each dipole simulation. The faded color indicates the optically thick region within the disk.

I show the apparent luminosity in Fig. 3.24. Similar to Fig. 3.13, the straight gray lines represent the viewing angles, and the faded-color straight lines are along the optically thick region where the apparent luminosity dropped to zero. The faded-color lines show the viewing angle at which no radiation flux could reach the observer. This viewing angle is shifted towards the polar axis with the increase in the accretion rate and the decrease in the magnetic field. The apparent luminosity in the lower magnetic field is between 42 - 220 $L_{\rm Edd}$ in the simulation of 10^{10} G and between 40 - 185 $L_{\rm Edd}$ in the simulation of 3×10^{10} G, both from low to high accretion rate.

I note that although the radiation efficiency decreases with increasing the accretion rate in each magnetic field simulation, the radiation is more strongly beamed and the apparent luminosity increases with the increase in the accretion rate.

3.4 Summary and conclusions

I simulate ULXs powered by accretion in moderately magnetized accreting neutron star in HMXBs.

I conducted 10 numerical simulations (Table 3.1) of the accreting magnetized neutron star with the accretion rate in the range of $100\,L_{\rm Edd}c^{-2}$ to $1000\,L_{\rm Edd}c^{-2}$. The neutron star dipole strength was in the range of $10^{10} - 10^{11}$ G following the prediction in KLK model (King & Lasota, 2020, 2019; King, Lasota, & Kluźniak, 2017).

The simulations are initialized with the equilibrium torus containing loops of the magnetic field which are oriented in opposite directions of the dipole magnetic field of the neutron star, leading to the magnetic reconnection. Thus in the strong magnetic field accreting material follows the field lines and falls on the surface of the neutron star.

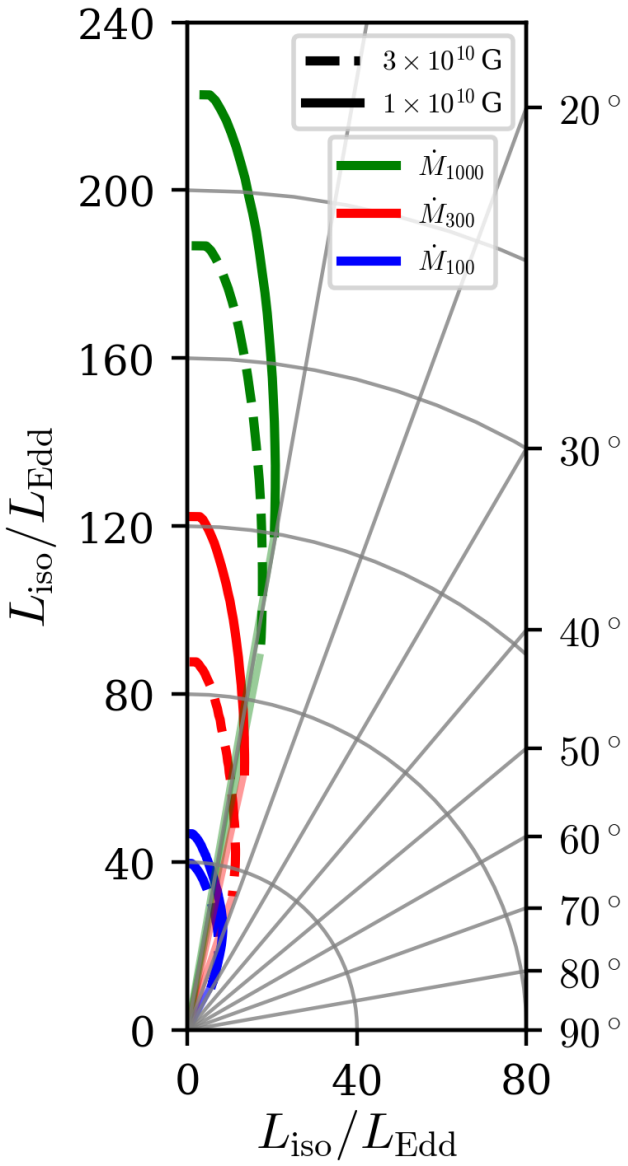

Figure 3.24: Isotropic luminosity in the unit of $L_{\rm Edd}$ in polar coordinate. The right and top axes show viewing angles. The straight gray solid lines correspond to particular viewing angles. The faded straight line in each magnetic field curve represents the optically thick region at which the radiation flux diminishes to zero.

In the first part of the study, I initialized the torus with the initial density producing the accretion rate above $200\,L_{\rm Edd}c^{-2}$ for models with different neutron star dipole strengths. In the second part of the study, I chose the dipole strengths 10^{10} G and 3×10^{10} G varying the density of the initial torus to simulate different accretion rates 100, 300, and $1000\,L_{\rm Edd}c^{-2}$.

Obtained results indicate that for the dipole strength from 10^{10} G to 10^{11} G the outflow rate increases from $80\,L_{\rm Edd}c^{-2}$ to $325L_{\rm Edd}c^{-2}$, respectively. The outflows propagate to angles close to the polar axis resulting in the cone-like optically thin region through which radiation flux escape towards the observer. This cone-like region widens with increasing dipole strength. Thus the radiation is more collimated in the weaker dipole in comparison to the stronger dipole. For $\dot{M}\simeq200L_{\rm Edd}c^{-2}$, the simulation with the weakest dipole in (10^{10} G) results in the smallest beaming factor of 0.02 and the highest apparent luminosity of about $120\,L_{\rm Edd}$, although the accretion rate in the weakest dipole simulation is lower than in the rest of magnetic field simulations.

The maximum apparent luminosity of the first part of this study is in the lower part of the luminosity observed from ULXs. The simulations with different accretion rates with the fixed dipole strengths indicate that with increasing the accretion rate, the outflow rate increases. The outflow rate increases from 60 to $4000\,L_{\rm Edd}c^{-2}$ for the accretion rate 100 to $1000\,L_{\rm Edd}c^{-2}$, respectively. Similar to the simulations with different dipole strengths, the outflow creates a cone-like optically thin region close to the polar axis. This cone-like region widens with a decrease in the accretion rate. The beaming factor of the highest accretion rate simulation ($1000\,L_{\rm Edd}c^{-2}$) with the dipole strength of 10^{10} G is 0.007 with the corresponding apparent luminosity $220\,L_{\rm Edd}$. The apparent luminosity in the magnetic field of $3\times10^{10}\,G$ and the accretion rate of $1000\,L_{\rm Edd}c^{-2}$ is about 185 Eddington units while in the accretion rate of $300\,L_{\rm Edd}c^{-2}$ it is about 100 Eddington units which is the lowest luminosity of detected ULXs. The accretion rate $100\,L_{\rm Edd}c^{-2}$ results in the apparent luminosity of about $40\,L_{\rm Edd}$ in both magnetic field simulations.

I conclude that the ULXs are likely accreting neutron stars with dipole magnetic fields of the order of 10^{10} G which they accrete beyond $300\,L_{\rm Edd}c^{-2}$.

A caveat in my study is that even with long simulations I performed, they reach about one-quarter of the pulsation period detected in PULXs. Thus my results are not suitable for the study of PULXs. Additionally, the thick outflows depending on the viewing angle may obscure the pulsation.

For future work, I will modify the model to study PULXs using 3D simulations with a tilted magnetic field relative to the rotation axis of the neutron star. This new study will be initiated with a stable accretion disk to minimize numerical artifacts and achieve a larger steady-state radius in a shorter simulation time.

I also note that although the $M1$ closure scheme is a powerful method to process radiation transfer in the code, for more accurate computation of the luminosity, post-processing radiation transfer would be beneficial. This can be achieved by e.g. the `HEROIC` code (Narayan, Zhu, et al., 2016). The code is capable of computing the radiation field and spectrum for an observer at infinity, taking into account different viewing angles.

Chapter 4

Paper 2: Moderately magnetized accreting neutron stars as ULXs with strong outflows

In this chapter, I present the paper intended for submission to the *Astrophysical Journal Letters* (ApJL). The primary focus of this letter is the beaming emission from super-Eddington accretion onto a neutron star with a magnetic field strength not exceeding 10^{11} G. The accretion rate exceeds 200 Eddington luminosities. We compare the outflows and apparent luminosities of accreting neutron stars with three different dipolar magnetic fields: 10^{10} G, 5×10^{10} G, and 10^{11} G. Our simulations reveal that, despite the lower accretion rate in the case of the weak dipole field (10^{10} G), the apparent luminosity is higher than in the simulations with stronger fields. The apparent luminosity exceeds 100 Eddington units, consistent with the luminosity of detected ULXs. The full study is presented in Chapter 3.

Draft version June 20, 2024
Typeset using LaTeX **twocolumn** style in AASTeX63

ULX collimation by outflows in moderately magnetized neutron stars

Fatemeh Kayanikhoo [1], Włodek Kluźniak [1] and Miljenko Čemeljić [2, 3, 1, 4]

[1] *Nicolaus Copernicus Astronomical Center of the Polish Academy of Sciences, Bartycka 18, 00-716 Warsaw, Poland*
[2] *College of Astronomy and Natural Sciences, SGMK Nicolaus Copernicus Superior School, Nowogrodzka 47A, 00-697 Warsaw, Poland*
[3] *Research Centre for Computational Physics and Data Processing, Institute of Physics, Silesian University in Opava, Bezručovo nám. 13, CZ-746 01 Opava, Czech Republic*
[4] *Academia Sinica, Institute of Astronomy and Astrophysics, P.O. Box 23-141, Taipei 106, Taiwan*

(Received; Revised; Accepted)

Submitted to ApJ

ABSTRACT

We perform radiative magnetohydrodynamics simulations in general relativity (GRRMHD) of super-Eddington accretion disk onto neutron stars endowed with a magnetic dipole corresponding to surface strengths not exceeding 100 GigaGauss. Accretion is found to power strong outflows which collimate the emergent radiation of the accretion columns, leading to apparent radiative luminosities of ~ 100 Eddington, when the true luminosity is a few Eddington units. Surprisingly, the collimation cone/angle widens with increasing magnetic field. Thus, in our simulations the apparent luminosity of the neutron star is substantially larger for weaker magnetic fields (10^{10} G) than for the stronger ones (10^{11} G).

Keywords: Ultraluminous X-ray sources, Magnetohydrodynamical simulations, Neutron stars

1. INTRODUCTION

Ultraluminous X-ray sources (ULXs) have puzzled astrophysicists since the 1990s. These non-nuclear extragalactic sources emit X-rays at luminosities exceeding $10^{41}\,\mathrm{erg\,s^{-1}}$, which is less than the luminosity of Active Galactic Nuclei (AGNs) but far surpassing the Eddington luminosity ($L_{\rm Edd}$) for a typical stellar-mass black hole (of mass $\sim 10\,M_\odot$) or a neutron star. Such extraordinary luminosity may be produced in binary systems where the accretor is either a massive black hole accreting below its Eddington limit or a stellar-mass black hole or a neutron star that accretes beyond its Eddington limit.

Over the years, different models have been proposed to explain ULXs. Colbert & Mushotzky (1999) suggested that the high luminosity of ULXs was attributed to sub-Eddington accretion in intermediate-mass black holes (IMBHs) with masses in the range of 10^2 to 10^4 $M_\odot$. Begelman (2002) suggested photon-bubble instability in accretion onto stellar mass black holes, but the model cannot explain luminosities higher than $3\times10^{40}\,\mathrm{ergs^{-1}}$ without beaming (see Lasota 2024, and references therein).

King et al. (2001) noted that ULXs may represent a transient stage in high-mass X-ray binaries (HMXB) characterized by extremely high mass transfer rates with compact accretor: stellar-mass black hole ($\sim 10M_\odot$), neutron star or white dwarf. They proposed super-Eddington accretion onto compact objects in intermediate and high mass X-ray binaries and emission geometrically beamed by outflows close to the accretor creating a funnel-like optically thin region. Radiation can reach the observer through the funnel, which is a fraction $b \ll 1$ of the solid angle of the sphere. Such an observer overestimates the true luminosity L by a beaming factor b in relation to the isotropic luminosity: $L_{\rm iso} \sim L/b$. The beaming emission was further studied by (King et al. 2017; King & Lasota 2019, 2020) known as KLK model.

We note that super-Eddington accretion and radiatively driven disk outflows were considered for black holes by Shakura & Sunyaev (1973), who find the disk luminosity to be proportional to $\sim [1+\ln \dot{M}/\dot{M}_{\rm Edd}]$. Here, the emitted radiation within a specific radius exceeds the Eddington limit called spherization radius. However, in the case of neutron stars the stellar mag-

Corresponding author: Fatemeh Kayanikhoo
fatima@camk.edu.pl

netic field may significantly affect the outflows, and the luminosity of the accretion stream hitting the stellar surface is expected to be on the order of $L \sim GM\dot{M}/R_*$, i.e., $L \sim 0.2\dot{M}c^2$ for a stellar radius of $R_* = 5r_g$, where $r_g = GM/c^2$ is the gravitational radius. In accreting neutron stars, the magnetic field truncates the accretion disk, allowing the material to accrete onto the neutron star along the magnetic field lines. Radiation can escape from the sides of the column, as detailed by Basko & Sunyaev (1976). If the spherization radius is larger than the magnetosphere the disk is radiatively outflow-driven between two radii.

In 2014, Bachetti et al. (2014) discovered that the source ULX–2 in the galaxy M82 exhibits pulsations in its lightcurve with an average period of 1.37 s. The coherence and the short period of this source indicate that the central object is a neutron star. This neutron star must accrete beyond Eddington limit, its apparent luminosity is $\sim 10^3 L_{\rm Edd}$ in the pulsed emission alone. This finding increased the possibility that ULXs are powered by super-Eddington accreting neutron stars. Subsequently, several other pulsating ULXs were discovered with spin periods and their derivatives in the range of less than a second to 12 minutes (e.g., Motch et al. 2014; Israel et al. 2016; Fürst, F. et al. 2018; Chandra et al. 2020).

In some models magnetars are considered as the accretor in ULXs (Ekşi et al. 2015; Mushtukov et al. 2017). Magnetic fields $\gtrsim 10^{14}$ G in accreting neutron star systems reduce electron scattering opacity for X-rays, resulting in an increase in the effective Eddington luminosity (Herold 1979; Ekşi et al. 2015). Strongly magnetized neutron stars ($B \geq 10^{14}\,G$) are required to produce the luminosities $\gtrsim 10^{40}\,{\rm erg\,s^{-1}}$ (Mushtukov et al. 2015). The scenario of accreting magnetars as ULXs was rejected by Kluźniak & Lasota (2015). They pointed out that ULX–2 M87 is not only distinguished from normal X-ray pulsars by its high luminosity but also the high spin-up rate of the neutron star that is 2 orders of magnitude higher than normal X-ray pulsars. They showed that the spin-up rate can not be attributed to a magnetar.

Lasota & King (2023) noted that the required magnetic field strength to increase the radiation luminosity up to the observed isotropic luminosity of ULXs is inconsistent with the spin-up rates seen in pulsating ULXs. In conclusion, a moderate magnetic field is required to explain the observed properties of ULXs powered by accreting neutron stars and concluded that the high luminosity of ULXs is caused by beaming emission as was shown in KLK model.

KLK model predicts the magnetic field of neutron star ULXs to be in the range of $10^{10}-10^{13}$ G with most of the values falling between $10^{10}-10^{11}$ G (King et al. 2017).

In this letter, we investigate the impact of the moderately strong dipolar magnetic field in the range of 10^{10} G to 10^{11} G on the luminosity and beaming emission. In Section 2, we outline the numerical method and the used simulation setup. Simulation outcomes and discussion are given in Section 3. We summarize our findings in the concluding Section 4.

2. NUMERICAL METHODS AND SIMULATIONS SETUP

We use the `Koral` code (Sądowski et al. 2015, 2013), to solve the equations of General Relativistic Radiative Magnetohydrodynamics (GRRMHD) on a static mesh with a fixed metric. Our setup is the same as described in Abarca et al. (2021), briefly summarized as follows. Conservation equations for matter and radiation energy-momentum are solved separately using standard explicit methods for gas and the M_1 closure scheme for radiation. Matter and radiation energy-momentum tensors are coupled with the radiation four-force (Mihalas & Mihalas 1984) through a local implicit method. The magnetic field is evolved by using the flux-interpolated constrained transport method (Tóth 2000), ensuring the divergence of the magnetic field remains at zero. The strong magnetizations within the neutron-star magnetosphere are addressed through a pioneering flooring scheme outlined by Parfrey & Tchekhovskoy (2017), later expanded for radiation considerations by Abarca et al. (2021).

We use a 2.5D grid based on the Schwarzschild metric with the signature $(-,+,+,+)$. The resolution of the simulations is $512 \times 510 \times 1$ cells in r, θ and ϕ directions, respectively. The grid spacing is logarithmically increasing in a radial direction, spanning from $r_{\rm in} = 5\,r_{\rm g}$ to $r_{\rm out} = 1000\,r_{\rm g}$, where $r_{\rm g}$ is the gravitational radius $r_{\rm g} = GM/c^2$. It is a well-established fact that in the axisymmetric cases, the magnetic field inside the accretion disk decays over time (the anti-dynamo theorem described in Cowling 1933). To address this, we utilize a mean-field dynamo (Sądowski et al. 2015) which effectively restores the magnetic field, mimicking the behavior expected in a full 3D simulation. This approach enables us to conduct long-duration simulations. We run the simulations to $50\,000\,t_{\rm g}$, where $t_g = GM/c^3$ is the gravitational time. We use the units where $G = c = 1$ in the equations.

We conducted simulations employing different strengths of the stellar dipole magnetic field, 1×10^{10}, 5×10^{10}, and 1×10^{11} G. The neutron star mass is 1.4

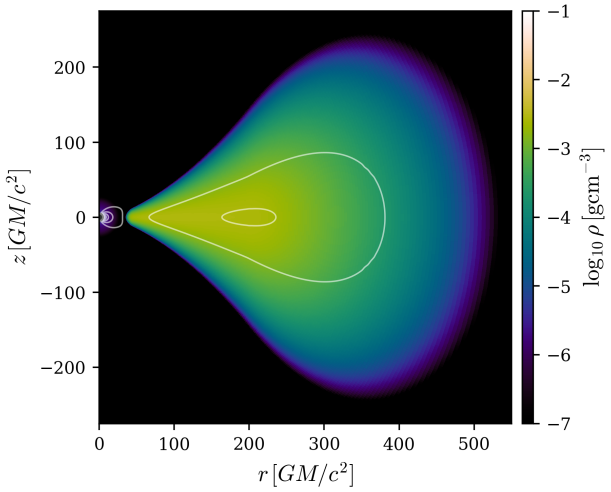

Figure 1. The initial rest mass density ρ in the fluid frame, shown with the logarithmic color grading in the simulation. Solid lines indicate the isocontour lines of the vector potential A_ϕ, which in our setup are parallel to the magnetic field lines. The surface magnetic field strength of dipole is 10^{11} G.

$M_\odot$ and the radius is $5\,r_\mathrm{g}$. We neglect the stellar rotation because the simulations run for 50 000 t_g, which is about 0.35 s of physical time, much smaller than the period of observed pulsating ULXs, which is of the order of seconds. All the simulations are initialized with the same equilibrium torus, which produces the mass accretion rate beyond $200\,L_\mathrm{Edd}c^{-2}$.

The initial setup for the simulation with the dipolar magnetic field of 10^{11} G is shown in Fig. 1. The simulation is initialized with a background atmosphere with density and internal energy several orders lower than in the initial torus. The inner radius of the torus is $34\,r_\mathrm{g}$ and it extends to radius $500\,r_\mathrm{g}$. We also note that in our model the disk is (nearly) Keplerian.

3. RESULTS AND DISCUSSION

We present the results in our simulations with the time-averaged data over the periods from $t = 15\,000\,t_\mathrm{g}$ to $50\,000\,t_\mathrm{g}$.

In Fig. 2 are shown the results for the radiation energy density and the rest-mass density, with the neutron star dipole magnetic fields differing by one order of magnitude. The disk is truncated at the magnetospheric (Alfvén) radius where the magnetic pressure dominates the ram pressure. The magnetospheric radius increases with the strength of the magnetic field. In the case of the weak magnetic field (10^{10} G), it is at $5.3\,r_\mathrm{g}$, very close to the surface of the neutron star while in the simulation of the strong magnetic field (10^{11} G), it is at about $18\,r_\mathrm{g}$.

During the simulation, the stellar dipole and the torus field lines, which are oriented in opposite directions, converge and undergo reconnection (Parfrey & Tchekhovskoy 2017; Abarca et al. 2021). As evident in the mid-plane of the disk of the left frame in Fig. 2, in the presence of the strong magnetic field (10^{11} G), the dipolar field lines close to the neutron star remain unchanged and the stream of dense matter follows the disk mid-plane field lines and the accretion column and falls on the surface of the neutron star. The right frame of Fig. 2 shows that in the simulation with the weaker dipole (10^{10} G), almost all dipolar field lines break and gas propagates to higher latitude. Thus, the radiation energy becomes more tightly collimated towards the polar axis. We discuss this fact in more details later in this section.

In the left-half panels of Fig. 2 is shown where the accreting material reaches the surface of the neutron star in the simulation with the weak magnetic field (right frame), radiation freely propagates toward the observer. In the simulation with the strong magnetic field (left frame), there is a thin layer of low-density material above the neutron star surface, between the accretion column and the neutron star axis. It is caused by the trapping of the background atmosphere in the strong magnetic field and this layer may slightly affect the radiation luminosity.

As the gas moves towards the neutron star, it releases energy in the form of thermal, kinetic, and radiation energies. In the accretion process, gravitational potential energy is converted into kinetic energy. Collisions within the disk convert kinetic energy into thermal energy, which heats the disk and causes radiation emission. It is crucial to accurately compute the kinetic energy that accelerates the outflow and powers the radiation luminosity. The radiation flux is

$$F^r_\mathrm{rad} = -R^r{}_t, \tag{1}$$

where $R^\mu{}_\nu$ is the radiation energy-momentum tensor, and the kinetic flux is

$$F^r_\mathrm{ke} = -\rho u^r(u_t + \sqrt{-g_{tt}}), \tag{2}$$

where u_t is the time component of 4-velocity, and $g_{tt} = -(1-2r_\mathrm{g}/r)$ in the Schwarzschild metric (for details see Sądowski et al. 2016). The lower time index causes a negative sign in the equations.

In Fig. 3 are shown the radiation flux (left-halt panels) and kinetic flux (right-half panels) for two magnetic fields 10^{11} G (at the top) and 10^{10} G (at the bottom). The fluxes are multiplied by $2\pi r\sin(\theta)$ and shown in the units of $[L_\mathrm{Edd}r_\mathrm{g}^{-1}]$. In each frame, the radius is extended to $500r_\mathrm{g}$, where the outer edge of the torus is located. Three contours in Fig. 3 separate different regions. The red dashed contour shows the zero

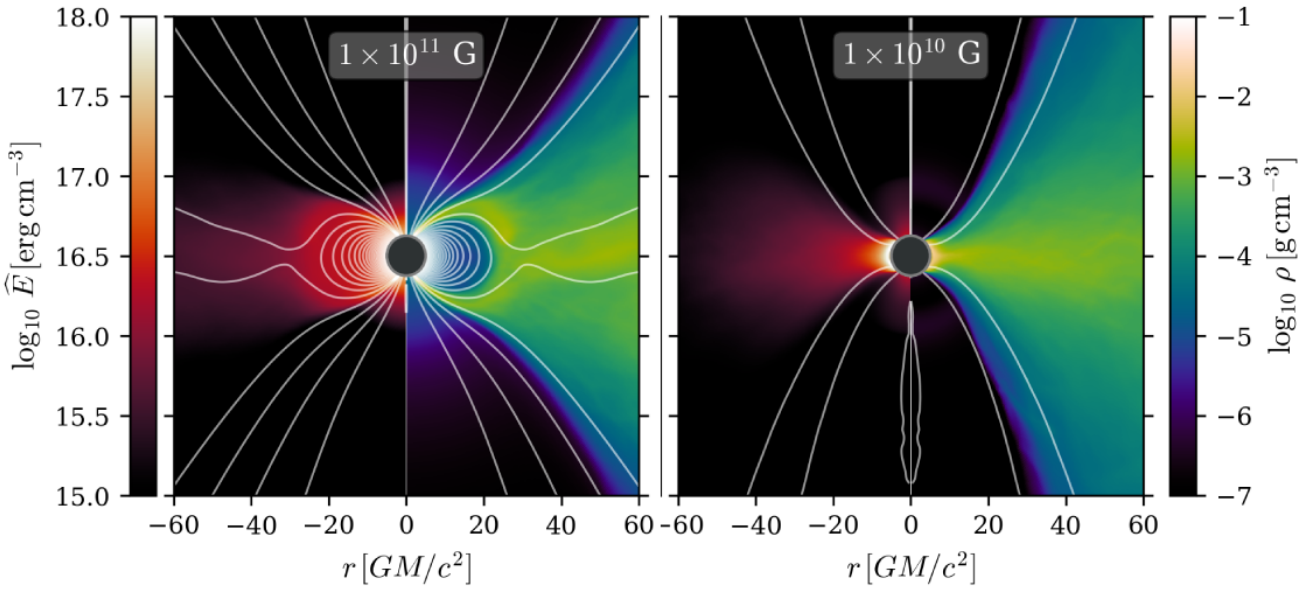

Figure 2. Our results in the cases with stellar dipoles of 10^{11} and 10^{10} G. The left half of the panels shows the radiation energy density $\hat{E}$ and the right half the rest-mass density ρ. Magnetic field lines are plotted as isocontours of the vector potential, A_ϕ. Note that the rarefied cones above and below the star are much wider for the 10^{11} G case.

Bernoulli surface where the relativistic Bernoulli parameter is computed:

$$Be = -\frac{T^t{}_t + R^t{}_t + \rho u^t}{\rho u^t}, \tag{3}$$

with $T^t{}_t$ and $R^t{}_t$ being the MHD and radiation energy densities, respectively. The zero Bernoulli surface splits the simulation domain into two parts. Above this surface, the gas with $Be > 0$ is energetic enough to reach infinity on its own. Below the surface, with $Be < 0$, the gas is energetically bounded within the disk. The white dashed and solid green lines represent surfaces of the photosphere computed in θ and r directions, respectively. The scattering optical depth along these contours are $\tau_\theta = 1$ and $\tau_\mathrm{r} = 1$, which are measured as follows,

$$\tau_\theta(\theta) = \int_0^\theta \rho\kappa_\mathrm{es}\sqrt{g_{\theta\theta}}d\theta, \tag{4}$$

$$\tau_\mathrm{r}(r) = \int_r^{r_\mathrm{out}} \rho\kappa_\mathrm{es}\sqrt{g_\mathrm{rr}}dr, \tag{5}$$

where $\kappa_\mathrm{es} = 0.34\,\mathrm{cm^2\,g^{-1}}$ is the electron scattering opacity for solar composition, r_out the outer boundary of the simulation.

The top-right panel in Fig. 3 shows that in the strong magnetic field simulation (10^{11} G) the outgoing kinetic flux above the zero Bernoulli surface is negligible. In the weak magnetic field simulation (10^{10} G), shown in the bottom-right panel, above zero Bernoulli surface there is a significant amount of outgoing kinetic flux. The outflows impact the photosphere structure in such a way that the photosphere surfaces $\tau_\theta = 1$ and $\tau_\mathrm{r} = 1$ (shown with the white dashed and solid green lines, respectively) are close to the polar axis of the neutron star in weak magnetic field simulation. The photosphere surface $\tau_\mathrm{r} = 1$ is located at the angle of 35° in the simulation with magnetic field 10^{11} G while it is along the viewing angle of about 15° in the simulation with magnetic field 10^{10} G.

The radiation flux is shown in the left panels of Fig. 3. The radiation flux is more beamed in the weak magnetic field simulation compared to the strong magnetic field simulation, attributable to the optically thin region ($\tau_\mathrm{r} < 1$) being narrower.

The top-left panel of Fig. 3 shows that in the simulation with the strong magnetic field, there is a larger amount of ingoing radiation flux along the equatorial plane, at the radii less than 100 r_g, compared to the simulation with the weak magnetic field. In the strong magnetic field, there is outgoing radiation flux within the zero Bernoulli surface at $r \gtrsim 300\,r_\mathrm{g}$. However, the simulation at the radii above $50\,r_\mathrm{g}$ contains numerical artifacts because the disk has not converged within the simulation time.

The accretion rate and outflow for three simulated magnetic field models are shown in Fig. 4. The accretion rate $\dot{M}(r)$ is measured by integrating the momentum density ρu^r over a spherical surface of a given radius:

$$\dot{M}(r) = -2\pi \int_0^\pi \rho u^r r^2 \sin\theta\, d\theta, \tag{6}$$

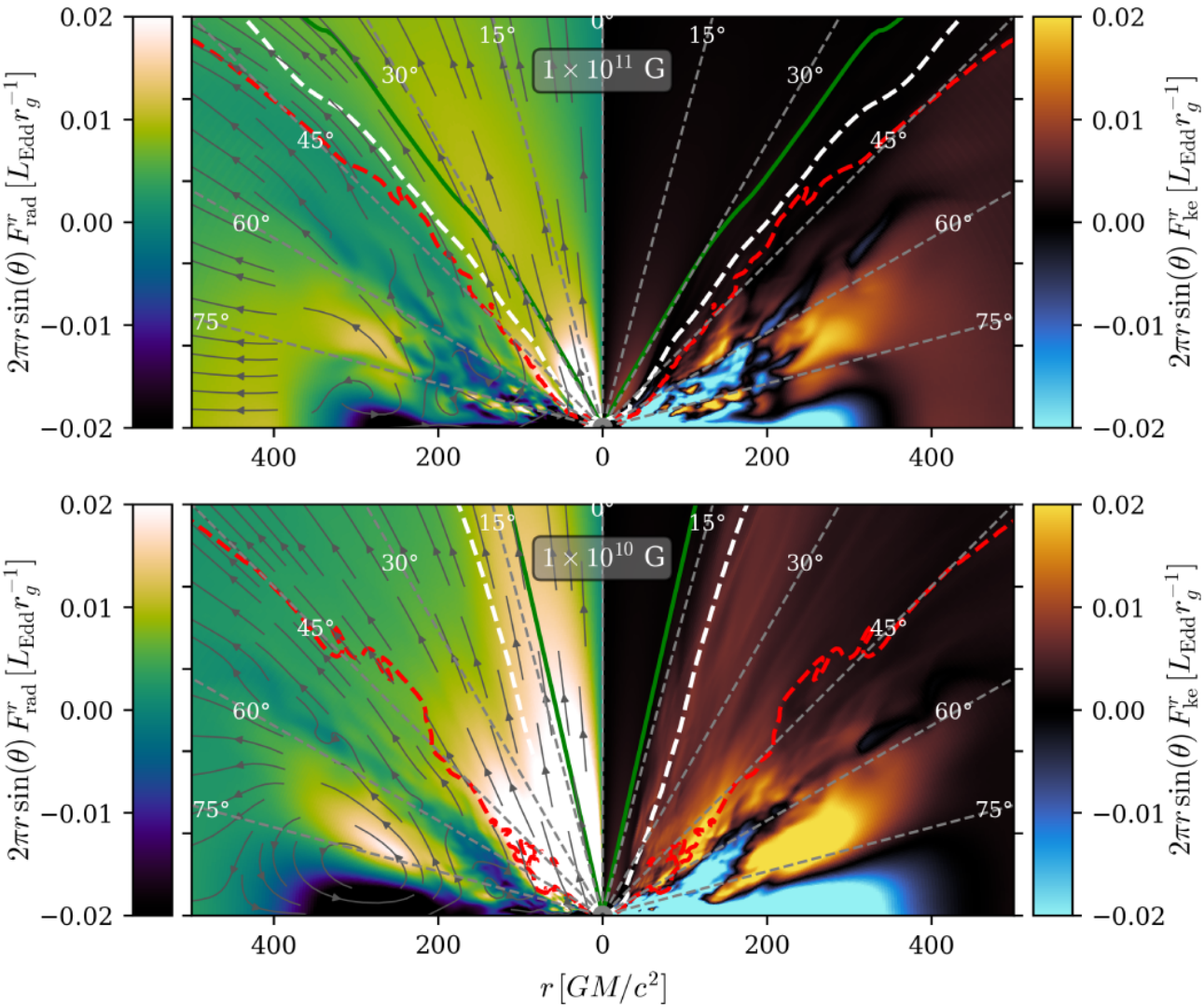

Figure 3. The radiation and kinetic fluxes in our simulations with the neutron star dipole 10^{11} G (*top panel*) and 10^{10} G (*bottom panel*) are shown in the left and right halves of each panel, respectively. The negative values indicate the direction towards the neutron star (inflow), while the positive values indicate outflow. The red dashed contour represents the zero Bernoulli surface. With the white dashed and solid green contours are delineated photospheres $\tau_\theta = 1$ and $\tau_r = 1$, respectively. The dashed grey lines show the viewing angles as labeled. The grey streamlines in the left half panels follow the radiation flux and indicate its direction.

and the outflow rate $\dot{M}_{\rm out}$ is computed from the momentum density of the gas outflowing away from the accretor ($u^r > 0$):

$$\dot{M}_{\rm out}(r) = 2\pi \int_0^\pi \rho u^r r^2 \sin\theta \, d\theta|_{u^r>0}. \qquad (7)$$

The radius at which the accretion rate is constant is called the steady-state radius. In our simulations, the accretion rate reaches the steady-state at $\sim 30\, r_{\rm g}$ in the simulations with the magnetic fields 10^{10} G and5×10^{10} G and at $20\, r_{\rm g}$ in the simulation with the magnetic field 10^{11} G. Our simulations show that the accretion rate decreases with decreasing magnetic field. As the dipole weakens, accreting material slows down as it approaches the neutron star. Subsequently, the material changes direction, resulting in significant outflows. This is shown in the middle panel of Fig. 4, where the outflow rate $\dot{M}_{\rm out}$ increases with decreasing the strength of the dipole.

Next, we compute the radiation luminosity in the optically thin region. Since radiation escapes from the accretion column along the θ direction, we compute the luminosity by integrating the radiation flux $F^r_{\rm rad}$ over

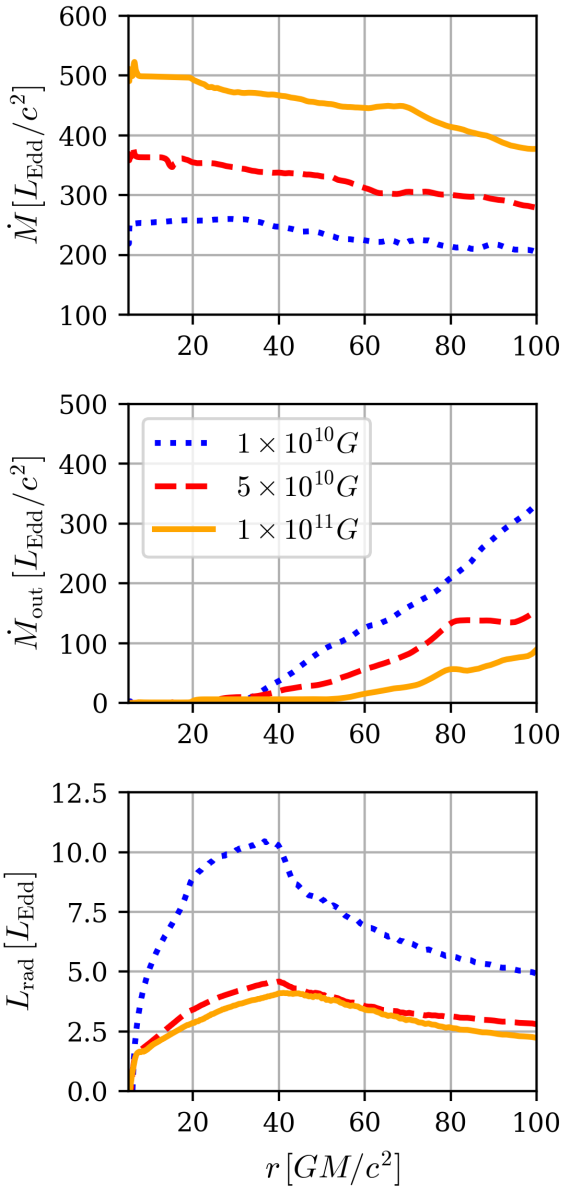

Figure 4. The accretion rate $\dot{M}$ (*top panel*) and outflow rate $\dot{M}_{\rm out}$ (*middle panel*) are shown in the unit of $L_{\rm Edd}/c^2$. *Bottom panel:* radiation luminosity in the optically thin region $\tau_\theta < 1$ in the unit of $L_{\rm Edd}$. From bottom to top, the magnetic field in each simulation is shown with a different color and line-style.

the spherical shell above the photosphere with $\tau_\theta = 1$:

$$L_{\rm rad} = 2\pi \int_{\tau_\theta<1} F^r_{\rm rad} r^2 \sin(\theta)\, d\theta. \quad (8)$$

The radiation luminosity within $\tau_\theta < 1$ is displayed in the bottom panel of Fig. 4. Due to the radiation shock, there is a steep rise with radius in radiation luminosity at the radii close to the star. Radiation luminosity increases up to radius $40\,r_{\rm g}$ as the radiation from the accretion column and disk are included. At distances greater than $40\,r_{\rm g}$, radiation decreases with increasing radius. This decrease in radiation luminosity is attributed to the momentum transfer of photons to the outflowing gas when they pass the outflow region. In the simulation with the weakest magnetic field (10^{10} G) which shows larger outflows, the drop in luminosity is more noticeable compared to the stronger magnetic field simulations.

We calculate the luminosity that reaches the observer by computing the luminosity in the optically thin region within the optical depth $\tau_{\rm r} < 1$ (the same as shown in Eq. 8). Since the accretion rate in each of the simulations is different, to enable comparison, we compute the radiation efficiency defined as the ratio of the radiation luminosity to the accretion rate $\dot{M}c^2$. The accretion rate is calculated at a radius of $20\,r_{\rm g}$. As mentioned earlier, at this radius, we find that the disk is in a steady-state in all simulated models presented in this letter.

The left panel of Fig. 5 shows the efficiency of radiation $L_{\rm rad}/(\dot{M}c^2)$ represented by thick colored lines, with different colors and line-styles corresponding to each magnetic field simulation. As the magnetic field increases, the efficiency of radiation luminosity decreases. A peak in the curve close to the star is caused by the radiation shock which is more significant in the stronger magnetic field simulations. We note that although we have implemented an energy-reflecting boundary condition with an albedo of 0.75 (Abarca et al. 2021; Abarca 2022), the photon-trapping phenomenon (Sądowski & Narayan 2016; Ohsuga et al. 2002) is so strong that the advected radiation flux dominates energy transport close to the surface of the neutron star. Consequently, the radiation efficiency is not as expected. The fluctuation in the curves at the small radii is most likely caused by the geometry of the photosphere close to the neutron star. The radiation efficiency is flattened at different radii depending on the strength of the dipole. At the radii where the curves are flat, the radiation efficiency of the simulation with the weakest magnetic field (10^{10} G) is about 0.007, while in the simulation with the strongest magnetic field (10^{11} G), is about 0.003. In the simulation with the weakest magnetic field (10^{10} G), there is a slight increase in the luminosity at $\gtrsim 400\,r_{\rm g}$, while in the strong magnetic field simulations ($\geq 5\times10^{10}$ G) the luminosity significantly increases at the radii $\gtrsim 200\,r_{\rm g}$. This increase is most likely due to the curvature of the photosphere at large radii enabling the radiation flux escape to the optically thin region (see Fig. 3). The

curvature of the photosphere can be attributed to the fewer outflows at larger radii.

The power in the outflow is computed by integrating the outgoing kinetic flux (given in Eq. 2) over a spherical surface at each radius,

$$L_{\rm ke} = 2\pi \int_0^{\theta=60^\circ} F^r_{\rm ke} r^2 \sin(\theta)\, d\theta \Big|_{u^r>0}, \qquad (9)$$

where the angle $\theta = 60^\circ$ is chosen to exclude the energy evolution within the torus.

The efficiency of the kinetic luminosity $L_{\rm ke}/(\dot{M}c^2)$ of the outflowing gas in each magnetic field simulation is represented by the three thin lines in the left panel of Fig. 5. The kinetic efficiency is of the same order of magnitude as the radiation efficiency in the simulation of the weakest magnetic field (10^{10} G) and about half of the radiation efficiency in the strongest magnetic field simulations (10^{11} G). At the radii less than $40\,r_{\rm g}$, where there are no outflows (as shown in the middle panel of Fig. 4) the kinetic luminosity diminishes to zero. At distances beyond $40\,r_{\rm g}$ with a significant amount of the outflow the kinetic luminosity increases steeply. In the simulations with dipole strengths $\geq 5\times10^{10}$ G the kinetic efficiency is almost constant (≤ 0.002) beyond the radius of about $100\,r_{\rm g}$. In the simulation with the weak magnetic field (10^{10} G) there is a steep rise in the kinetic efficiency to the radius of $150\,r_{\rm g}$, continuing to $250\,r_{\rm g}$. The maximum kinetic efficiency with this magnetic field simulation is about 0.007.

From the observational perspective, isotropic (apparent) luminosity $L_{\rm iso}$ is an important parameter. But if the source is not isotropic, the observer overestimates $L_{\rm iso}$ by a factor of $1/b$ where the beaming factor $b \ll 1$.

It was shown through numerical simulations in Abarca et al. (2018) that non-magnetized neutron stars cannot have an apparent luminosity that exceeds the Eddington limit, even with a super-Eddington accretion rate. Subsequently, Abarca et al. (2021) showed that in the simulation of a super-Eddington accreting neutron star with a dipolar magnetic field 2×10^{10} G, the apparent luminosity is beyond $100\,L_{\rm Edd}$.

We compute the apparent luminosity $L_{\rm iso} = 4\pi d^2 F^r_{\rm rad}$ where d is the distance between an observer and the object, in our simulations we compute the apparent luminosity at $d = 500\,r_{\rm g}$. To include all the radiation luminosity that may reach the observer depending of their viewing angle (neglecting cosmological effects) we compute $F^r_{\rm rad}$ in the optically thin region $\tau_{\rm r} < 1$.

In the right panel of Fig. 5, is shown the apparent luminosity $L_{\rm iso}$ in the units of $L_{\rm Edd}$ at various viewing angles. The viewing angles are indicated with straight grey solid lines. At large angles, where the optically thick disk is located, no radiation flux can be detected by the observer, so the apparent luminosity is zero. In our simulations, this angle changes with respect to the strength of the dipole which is shown by the faded-color lines for each magnetic field simulation. For instance, if we look at the object with a magnetic field 10^{10} G from a viewing angle of about 15°, the apparent luminosity is zero.

The observed luminosity of an object varies depending on the viewing angle, as shown in the right panel of Fig. 5. When the viewing angle is less than 15°. The apparent luminosity reaches the maximum value along the polar axis. It is evidence that the apparent luminosity decreases with increasing dipole strength, although the accretion rate changes conversely. The apparent luminosity reaches about $120\,L_{\rm Edd}$ for the simulation with dipole strength 10^{10} G, and is only about $40\,L_{\rm Edd}$ in the simulation with dipole strength 10^{11} G. Our simulations show that ULXs are likely powered by accreting neutron stars with a dipole of 10^{10} G. However, this luminosity is the lower luminosity of detected ULXs.

4. SUMMARY AND CONCLUSIONS

In this letter, we study beamed X-ray emission from neutron stars in the context of ULXs. We perform general relativistic radiative magnetohydrodynamics simulations of supercritical accretion onto neutron stars with dipolar magnetic fields in the range of 10^{10} to 10^{11} G (maximum surface values, corresponding to dipole strengths 10^{28} to $10^{29}\,{\rm G}\cdot{\rm cm}^3$ for our canonical neutron star radius of 10 km). The mass accretion rate onto the star is set to be above $200\,L_{\rm Edd}/c^2$; the rate of mass flow through the accretion disk is even higher, reflecting strong outflows from the disk.

Our simulations show that the magnetic field 10^{10} G leads to significant outflows about $300\,L_{\rm Edd}c^{-2}$, locating the photosphere close to the polar axis of the neutron star, roughly on the surface of a cone of opening angle $\approx 15^\circ$. Thus, the radiation escaping toward the observer through the optically thin cone is highly beamed and reaches an apparent luminosity of about 120 Eddington units along the polar axis although the true luminosity is about 10 Eddington units. For a magnetic field increased by an order of magnitude (B = 10^{11} G) the outflow is about $100\,L_{\rm Edd}/c^2$, and the optically thin region is widened to an angle of about 35°. Here, the luminosity is less collimated compared to the lower magnetic field. The maximum value of apparent luminosity is about 40 Eddington luminosity along the polar axis.

The beaming factor b is about 0.02 in the weak magnetic field simulation and about 0.08 in the strong magnetic field simulation. The beaming factor in our

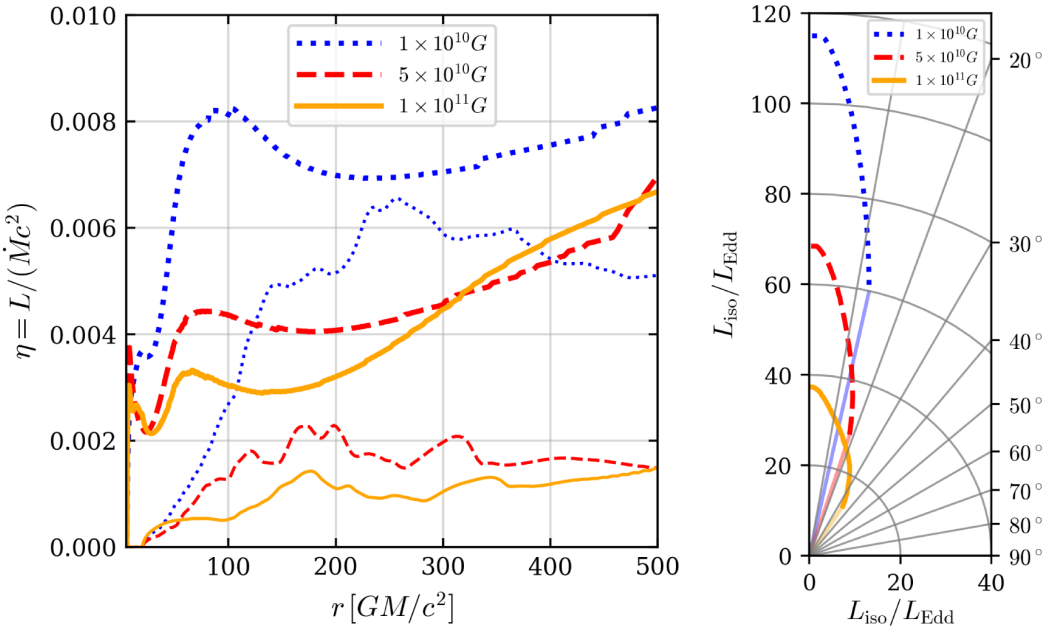

Figure 5. *Left panel:* The radiative efficiency in the optically thin region $\tau_{\rm r} < 1$ (thick lines) and kinematic efficiency (thin lines) both relative to the mass accretion rate onto the neutron star, $L/(\dot{M}c^2)$, as a function of the radius. The kinetic luminosity is computed from outgoing kinetic flux above the torus $\theta \leq 60°$ shown in Fig. 3. *Right panel:* The isotropic luminosity as a function of the viewing angle, $L_{\rm iso}(\theta) = 4\pi d^2 F^r_{\rm rad}(\theta)$, computed at $d = 500 r_{\rm g}$ in the optically thin cone, $\tau_r < 1$. The radiation luminosity is taken to drop to zero at $\tau_r = 1$ shown with faded colors, i.e. at viewing angles corresponding to the opening angle of the optically thin cone. In this polar diagram of the beaming pattern, the straight grey solid lines correspond to particular viewing angles. From bottom to top in both panels, the magnetic field in each simulation is shown with a different color and line-style.

model is comparable to the one estimated in the KLK model. However, our simulations cannot be directly be compared with the KLK model, as the spherization and magnetosphere radii are close in the KLK model, whereas, in our model, the spherization radius is significantly larger.

We conclude that ultraluminous X-ray sources are likely powered by neutron stars with a dipolar magnetic field in order of 10^{10} G which accreting above 200 Eddington luminosities.

In future work, we will conduct numerical simulations across a wide range of magnetic fields and accretion rates to determine the limit for interpreting ultraluminous X-ray sources powered by accreting neutron stars.

We also note that for more accurate computation of the luminosity, post-processing radiation transfer is required. This can be achieved using the `HEROIC` code (Narayan et al. 2016). The code is capable of computing the radiation field and spectrum for an observer at infinity, taking into account different viewing angles. This processing will be done in future research.

ACKNOWLEDGMENTS

F.K. thanks David Abarca and Dominik Gronkiewicz for their useful discussions and technical help, and Jean-Pierre Lasota and Agata Różańska for their valuable advice and suggestions. Research in CAMK was in part supported by the Polish National Center for Science grant 2019/33/B/ST9/01564. M.Č. acknowledges the Czech Science Foundation (GAČR) grant No. 21-06825X and the support by the International Space Science Institute (ISSI) in Bern, which hosted the International Team project No. 495 (Feeding the spinning top) with its inspiring discussions. We gratefully acknowledge Polish high-performance computing infrastructure PLGrid (HPC Center: ACK Cyfronet AGH) for providing computer facilities and support within computational grant no. PLG/2023/016648.

REFERENCES

Abarca, D. 2022, PhD thesis, Nicolaus Copernicus Astronomical Center Polish Academy of Sciences

Abarca, D., Kluźniak, W., & Sądowski, A. 2018, Monthly Notices of the Royal Astronomical Society, 479, 3936, doi: 10.1093/mnras/sty1602

Abarca, D., Parfrey, K., & Kluźniak, W. 2021, The Astrophysical Journal, Letter, 917, L31, doi: 10.3847/2041-8213/ac1859

Bachetti, M., Harrison, F., Walton, D. J., et al. 2014, Nature, 514, 202

Basko, M. M., & Sunyaev, R. A. 1976, Monthly Notices of the Royal Astronomical Society, 175, 395, doi: 10.1093/mnras/175.2.395

Begelman, M. C. 2002, The Astrophysical Journal, 568, L97, doi: 10.1086/340457

Chandra, A. D., Roy, J., Agrawal, P. C., & Choudhury, M. 2020, Monthly Notices of the Royal Astronomical Society, 495, 2664, doi: 10.1093/mnras/staa1041

Colbert, E. J. M., & Mushotzky, R. F. 1999, The Astrophysical Journal, 519, 89, doi: 10.1086/307356

Cowling, T. G. 1933, Monthly Notices of the Royal Astronomical Society, 94, 39, doi: 10.1093/mnras/94.1.39

Ekşi, K. Y., Andaç, I. C., Çıkıntoğlu, S., et al. 2015, Monthly Notices of the Royal Astronomical Society: Letters, 448, L40, doi: 10.1093/mnrasl/slu199

Fürst, F., Walton, D. J., Heida, M., et al. 2018, A&A, 616, A186, doi: 10.1051/0004-6361/201833292

Herold, H. 1979, Phys. Rev. D, 19, 2868, doi: 10.1103/PhysRevD.19.2868

Israel, G. L., Papitto, A., Esposito, P., et al. 2016, Monthly Notices of the Royal Astronomical Society: Letters, 466, L48, doi: 10.1093/mnrasl/slw218

King, A., & Lasota, J.-P. 2019, Monthly Notices of the Royal Astronomical Society, 485, 3588

—. 2020, Monthly Notices of the Royal Astronomical Society, 494, 3611, doi: 10.1093/mnras/staa930

King, A., Lasota, J.-P., & Kluzniak, W. 2017, Monthly Notices of the Royal Astronomical Society: Letters, 468, L59, doi: 10.1093/mnrasl/slx020

King, A. R., Davies, M. B., Ward, M. J., Fabbiano, G., & Elvis, M. 2001, The Astrophysical Journal, 552, L109, doi: 10.1086/320343

Kluźniak, W., & Lasota, J.-P. 2015, Monthly Notices of the Royal Astronomical Society: Letters, 448, L43, doi: 10.1093/mnrasl/slu200

Lasota, J., & King, A. 2023, Monthly Notices of the Royal Astronomical Society, 526, 2506, doi: 10.1093/mnras/stad2926

Lasota, J.-P. 2024, Problems in the astrophysics of accretion onto compact celestial bodies. https://arxiv.org/abs/2311.16013

Mihalas, D., & Mihalas, B. W. 1984, Foundations of radiation hydrodynamics

Motch, C., Pakull, M. W., Soria, R., Grisé, F., & Pietrzyński, G. 2014, Nature, 514, 198, doi: 10.1038/nature13730

Mushtukov, A. A., Suleimanov, V. F., Tsygankov, S. S., & Poutanen, J. 2015, Monthly Notices of the Royal Astronomical Society, 447, 1847–1856, doi: 10.1093/mnras/stu2484

Mushtukov, A. A., Verhagen, P. A., Tsygankov, S. S., et al. 2017, Monthly Notices of the Royal Astronomical Society, 474, 5425, doi: 10.1093/mnras/stx2905

Narayan, R., Zhu, Y., Psaltis, D., & Sadowski, A. 2016, Monthly Notices of the Royal Astronomical Society, 457, 608

Ohsuga, K., Mineshige, S., Mori, M., & Umemura, M. 2002, The Astrophysical Journal, 574, 315, doi: 10.1086/340798

Parfrey, K., & Tchekhovskoy, A. 2017, The Astrophysical Journal, Ltter, 851, L34, doi: 10.3847/2041-8213/aa9c85

Shakura, N. I., & Sunyaev, R. A. 1973, A&A, 24, 337

Sądowski, A., Narayan, R., Tchekhovskoy, A., et al. 2015, MNRAS, 447, 49, doi: 10.1093/mnras/stu2387

Sądowski, A., Narayan, R., Tchekhovskoy, A., & Zhu, Y. 2013, Monthly Notices of the Royal Astronomical Society, 429, 3533, doi: 10.1093/mnras/sts632

Sądowski, A., Lasota, J.-P., Abramowicz, M. A., & Narayan, R. 2016, Monthly Notices of the Royal Astronomical Society, 456, 3915, doi: 10.1093/mnras/stv2854

Sądowski, A., & Narayan, R. 2016, Monthly Notices of the Royal Astronomical Society, 456, 3929, doi: 10.1093/mnras/stv2941

Tóth, G. 2000, Journal of Computational Physics, 161, 605, doi: 10.1006/jcph.2000.6519

Chapter 5

Conclusions and remarks

The objective of my thesis is to conduct numerical simulations with radiation transfer, to study the ultraluminous X-ray sources (ULXs), focusing on accretion-powered pulsars with moderate dipolar magnetic fields as the source of ultraluminous X-rays.

Due to the importance of precision in numerical simulations in evaluating astrophysical systems under extreme physical conditions, my PhD project has been divided into two main parts: PART I involves evaluating the numerical simulation codes with respect to energy conversion in magnetohydrodynamics (MHD) simulations. PART II focuses on simulating super-Eddington accretion onto moderately magnetized neutron stars and investigating the impact of two main parameters, the mass accretion rate and strength of magnetic dipole on the apparent luminosity of this system.

PART I. I performed the well-established Orszag-Tang test problem for MHD simulation codes in two high-performance codes in astrophysics, Newtonian code `Pluto` and general relativistic radiative magnetohydrodynamics code (GRRMHD) `Koral`. I conducted simulations of relativistic, resistive, and ideal MHD models in both 2D and 3D and compared the precision of two codes in capturing substructures.

- The numerical dissipation was estimated using resistive and ideal MHD simulations in `Pluto`. The numerical dissipation at the resolution of 512×512 was estimated to be 10^{-4} which is the lower limit of resistivity for plasmoid unstable magnetic reconnection.
- In the ideal non-relativistic MHD simulations, kinetic and magnetic energies dissipate to internal energy, heating the plasma during the simulation.
- In relativistic MHD simulations, energy is mainly converted between magnetic and kinetic forms during the simulation.
- The reconnection rate is consistent with Petschek's fast reconnection in resistive MHD.
- Reconnection depends on resolution in low resolutions and remains constant in high resolutions.
- The code comparison indicated that `Koral` is more precise in capturing substructures in comparison to `Pluto`.

- The simulations conducted using `Koral` included fewer unphysical artifacts in low resolusions compared to `Pluto`.

Part II. I investigated accreting neutron stars with the apparent luminosities consistent with ULXs. In six numerical simulations, I investigated how the dipole strength of the neutron star impacts the structure of the accretion disk/column and apparent luminosity. The effect of the super-Eddington accretion rate was investigated with three accretion rates for two dipole magnetic field strengths. The results are as follows:

- With increasing dipole magnetic field strength, the magnetospheric radius is located further from the star, approximating well the analytical solution.
- The efficiency of the accretion disk in the stronger dipole simulation (10^{11} G) is smaller than in the weak dipole simulation (10^{10} G).
- Although the accretion rate decreases with an increase in the dipole strength, the apparent luminosity of the weaker dipole is higher.
- The apparent luminosity in the simulations with dipole weaker than 3×10^{10} G is $\gtrapprox$ 100 Eddington units which is the lower limit of the luminosity of ULXs.
- With decreasing accretion rate in each dipole strength simulation, the magnetospheric radius is located further from the star. The magnetospheric radius in a weak dipole field of 10^{10} G as a function of the accretion rate is very close to the neutron star surface.
- The efficiency of radiation luminosity decreases with increasing the accretion rate.
- The apparent luminosity increases with increasing the accretion rate.
- In both dipole simulations (10^{10} and 3×10^{10} G) with the accretion rate of 100 Eddington luminosities, the apparent luminosity remains about 40 Eddington units which is not compatible with ULXs.
- The accretion rate beyond 300 Eddington luminosities in both dipole simulations (10^{10} and 3×10^{10} G) results in the apparent luminosity beyond 100 Eddington units which is compatible with ULXs.
- The highest apparent luminosity corresponds to the dipole strength of 10^{10} G and accretion rate of 1000 Eddington luminosities that is about 220 Eddington limits.

Caveats. The accretion systems involving compact objects are characterized by strong gravitational forces, high temperatures, radiation, intense magnetic fields, and rapid velocities. These conditions pose significant challenges for numerical simulations, especially when considering a neutron star as the accretor, with its hard surface and intrinsic magnetic field.

The most challenging part was the inner radial boundary. I used the energy-reflecting boundary condition on the surface of the neutron star, as implemented in

`Koral` by Abarca, Parfrey, & Kluźniak (2021). Although the albedo in my simulations is formally 0.75, the high accretion rate, along with a strong magnetic field, results in a much lower value of reflection on the surface of the neutron star which is less than 5%.

I ran simulations for a long time and time-averaged data were computed over a long duration. However, the disk converges and reaches a steady state at a small radius in simulations with strong magnetic fields. I intend to extend the simulation time to reduce numerical artifacts at larger radii. Additionally, the simulations were initialized with an equilibrium torus, which requires a longer simulation time for the disk to converge. I will initialize the simulations with an initial stable disk to address this issue.

Future plan. For the numerical simulations study of pulsating ULXs, I wrote a proposal during the last year of my PhD and I obtained a grant from the National Science Center of Poland. I will conduct 3D simulations of the super-Eddington accreting neutron star with an inclined magnetic field axis. I will investigate the impact of the inclination angle of the magnetic field relative to the rotation axis on the accretion structure, luminosity and pulsations of ULXs. I will also use the `HEROIC` code (Narayan, Zhu, et al., 2016) for post-processing radiative transfer, recomputing the radiation field and spectrum, enabling us to compare the simulations with observational data.

References

Abarca, D. (2022). *Numerical simulations of accretion onto neutron stars* (Unpublished doctoral dissertation). Nicolaus Copernicus Astronomical Center Polish Academy of Sciences.

Abarca, D., Kluźniak, W., & Sądowski, A. (2018, 06). Radiative GRMHD simulations of accretion and outflow in non-magnetized neutron stars and ultraluminous X-ray sources. *Monthly Notices of the Royal Astronomical Society*, *479*(3), 3936-3951.

Abarca, D., Parfrey, K., & Kluźniak, W. (2021, August). Beamed Emission from a Neutron-star ULX in a GRRMHD Simulation. *The Astrophysical Journal, Letter*, *917*(2), L31.

Abramowicz, M. A., Czerny, B., Lasota, J. P., & Szuszkiewicz, E. (1988, September). Slim Accretion Disks. ApJ, *332*, 646.

Bachetti, M., Harrison, F., Walton, D. J., Grefenstette, B., Chakrabarty, D., Fürst, F., Barret, D., Beloborodov, A., Boggs, S., Christensen, F. E., et al. (2014). An ultraluminous x-ray source powered by an accreting neutron star. *Nature*, *514*(7521), 202–204.

Balbus, S. A., & Hawley, J. F. (1991, July). A Powerful Local Shear Instability in Weakly Magnetized Disks. I. Linear Analysis. *Astrophysical journal*, *376*, 214.

Balbus, S. A., & Hawley, J. F. (1998, Jan). Instability, turbulence, and enhanced transport in accretion disks. *Rev. Mod. Phys.*, *70*, 1–53.

Basko, M. M., & Sunyaev, R. A. (1976, 05). The Limiting Luminosity of Accreting Neutron Stars With Magnetic Fields. *Monthly Notices of the Royal Astronomical Society*, *175*(2), 395-417.

Begelman, M. C. (2002, April). Super-Eddington Fluxes from Thin Accretion Disks? *Astrophysical Journal Letter*, *568*(2), L97-L100.

Brightman, M., Harrison, F. A., Fürst, F., Middleton, M. J., Walton, D. J., Stern, D., Fabian, A. C., Heida, M., Barret, D., & Bachetti, M. (2018). Magnetic field strength of a neutron-star-powered ultraluminous x-ray source. *Nature Astronomy*, *2*(4), 312–316.

Canuto, V., Lodenquai, J., & Ruderman, M. (1971, May). Thomson scattering in a strong magnetic field. *Phys. Rev. D*, *3*, 2303–2308.

Carpano, S., Haberl, F., Maitra, C., & Vasilopoulos, G. (2018, 02). Discovery of pulsations from NGC300ULX1 and its fast period evolution. *Monthly Notices of the Royal Astronomical Society: Letters*, *476*(1), L45-L49.

Chael, A. (2024, April). Hybrid GRMHD and Force-Free Simulations of Black Hole Accretion. *arXiv e-prints*, arXiv:2404.01471.

Chael, A. A., Narayan, R., & Sądowski, A. (2017, 07). Evolving non-thermal electrons in simulations of black hole accretion. *Monthly Notices of the Royal Astronomical Society*, *470*(2), 2367-2386.

Chandra, A. D., Roy, J., Agrawal, P. C., & Choudhury, M. (2020, 06). Study of recent outburst in the Be X-ray binary RX J0209.6-7427 with AstroSat: a new ultraluminous X-ray pulsar in the Magellanic Bridge? *Monthly Notices of the Royal Astronomical Society*, *495*(3), 2664-2672.

Chatterjee, K., Chael, A., Tiede, P., Mizuno, Y., Emami, R., Fromm, C., Ricarte, A., Blackburn, L., Roelofs, F., Johnson, M. D., Doeleman, S. S., Arras, P., Fuentes, A., Knollmüller, J., Kosogorov, N., Lindahl, G., Müller, H., Patel, N., Raymond, A., Traianou, E., & Vega, J. (2023, February). Accretion Flow Morphology in Numerical Simulations of Black Holes from the ngEHT Model Library: The Impact of Radiation Physics. *Galaxies*, *11*(2), 38.

Colbert, E. J. M., & Mushotzky, R. F. (1999, jul). The nature of accreting black holes in nearby galaxy nuclei. *The Astrophysical Journal*, *519*(1), 89–107.

Cowling, T. G. (1933, November). The magnetic field of sunspots. *Monthly Notices of the Royal Astronomical Society*, *94*, 39-48.

Das, P., & Porth, O. (2024, jan). Three-dimensional grmhd simulations of neutron star jets. *The Astrophysical Journal Letters*, *960*(2), L12.

Doroshenko, V., Tsygankov, S., & Santangelo, A. (2018). Orbit and intrinsic spin-up of the newly discovered transient x-ray pulsar swift j0243.6+6124. *A&A*, *613*, A19.

Dubus, G., Hameury, J.-M., & Lasota, J.-P. (2001, July). The disc instability model for x-ray transients: Evidence for truncation and irradiation. *Astronomy and Astrophysics*, *373*(1), 251–271.

Dubus, G., Lasota, J.-P., Hameury, J.-M., & Charles, P. (1999, February). X-ray irradiation in low-mass binary systems. *Monthly Notices of the Royal Astronomical Society*, *303*(1), 139–147.

Elsner, R. F., & Lamb, F. K. (1977, August). Accretion by magnetic neutron stars. I. Magnetospheric structure and stability. *The Astrophysical Journal*, *215*, 897-913.

Fabbiano, G. (1989, January). X-rays from normal galaxies. *Annual Review of Astronomy and Astrophysics*, *27*, 87-138.

Frank, J., King, A. R., & Raine, D. (2002). *Accretion power in astrophysics*. Cambridge university press.

Fürst, F., Walton, D. J., Heida, M., Harrison, F. A., Barret, D., Brightman, M., Fabian, A. C., Middleton, M. J., Pinto, C., Rana, V., Tramper, F., Webb, N., & Kretschmar, P. (2018). A tale of two periods: determination of the orbital ephemeris of the super-eddington pulsar ngc 7793 p13. *A&A*, *616*, A186.

Gammie, C. F., McKinney, J. C., & Tóth, G. (2003, May). HARM: A Numerical Scheme for General Relativistic Magnetohydrodynamics. ApJ, *589*(1), 444-457.

Giacconi, R., Gursky, H., Kellogg, E., Schreier, E., & Tananbaum, H. (1971, July). Discovery of Periodic X-Ray Pulsations in Centaurus X-3 from UHURU. ApJ, *167*, L67.

Gommers, R., Virtanen, P., Haberland, M., Burovski, E., Weckesser, W., Reddy, T., Oliphant, T. E., Cournapeau, D., Nelson, A., alexbrc, Roy, P., Peterson, P., Polat, I., Wilson, J., endolith, Mayorov, N., van der Walt, S., Brett, M., Laxalde, D., Larson, E., Sakai, A., Millman, J., Lars, peterbell10, Carey, C., van Mulbregt, P., eric-jones, Kai, McKibben, N., & Colley, L. (2024, May). *scipy/scipy: SciPy 1.14.0rc1.* Zenodo.

Hallur, P., Medeiros, L., & Christian, P. (2023, September). Characterizing Power Spectra of GRMHD Simulations using the Taylor Frozen Hypothesis. In *Aas/high energy astrophysics division* (Vol. 20, p. 117.13).

Harding, A. K. (2013, December). The neutron star zoo. *Frontiers of Physics*, *8*(6), 679-692.

Harris, C. R., Millman, K. J., van der Walt, S. J., Gommers, R., Virtanen, P., Cournapeau, D., Wieser, E., Taylor, J., Berg, S., Smith, N. J., Kern, R., Picus, M., Hoyer, S., van Kerkwijk, M. H., Brett, M., Haldane, A., del Río, J. F., Wiebe, M., Peterson, P., Gérard-Marchant, P., Sheppard, K., Reddy, T., Weckesser, W., Abbasi, H., Gohlke, C., & Oliphant, T. E. (2020, September). Array programming with NumPy. Nature, *585*(7825), 357-362.

Heida, M., Lau, R. M., Davies, B., Brightman, M., Fürst, F., Grefenstette, B. W., Kennea, J. A., Tramper, F., Walton, D. J., & Harrison, F. A. (2019, sep). Discovery of a red supergiant donor star in sn2010da/ngc 300 ulx-1. *The Astrophysical Journal Letters*, *883*(2), L34.

Herold, H. (1979, May). Compton and thomson scattering in strong magnetic fields. *Phys. Rev. D*, *19*, 2868–2875.

Hewish, A., Bell, S. J., Pilkington, J. D. H., Scott, P. F., & Collins, R. A. (1968, February). Observation of a Rapidly Pulsating Radio Source. Nature, *217*(5130), 709-713.

Houck, J. C., & Chevalier, R. A. (1992, August). Linear Stability Analysis of Spherical Accretion Flows onto Compact Objects. ApJ, *395*, 592.

Hunter, J. D. (2007, May). Matplotlib: A 2D Graphics Environment. *Computing in Science and Engineering*, *9*(3), 90-95.

Illarionov, A. F., & Sunyaev, R. A. (1975, February). Why the Number of Galactic X-ray Stars Is so Small? A&A, *39*, 185.

Israel, G. L., Belfiore, A., Stella, L., Esposito, P., Casella, P., Luca, A. D., Marelli, M., Papitto, A., Perri, M., Puccetti, S., Castillo, G. A. R., Salvetti, D., Tiengo, A., Zampieri, L., D'Agostino, D., Greiner, J., Haberl, F., Novara, G., Salvaterra, R., Turolla, R., Watson, M., Wilms, J., & Wolter, A. (2017). An accreting pulsar with extreme properties drives an ultraluminous x-ray source in ngc 5907. *Science*, *355*(6327), 817-819.

Israel, G. L., Papitto, A., Esposito, P., Stella, L., Zampieri, L., Belfiore, A., Rodríguez Castillo, G. A., De Luca, A., Tiengo, A., Haberl, F., Greiner, J., Salvaterra, R., Sandrelli, S., & Lisini, G. (2016, 10). Discovery of a 0.42-s pulsar in the ultraluminous X-ray source NGC-7793 P13. *Monthly Notices of the Royal Astronomical Society: Letters*, *466*(1), L48-L52.

Jiang, Y.-F., Stone, J. M., & Davis, S. W. (2014, nov). A global three-dimensional radiation magneto-hydrodynamic simulation of super-eddington accretion disks. *The Astrophysical Journal*, *796*(2), 106.

Kawashima, T., Mineshige, S., Ohsuga, K., & Ogawa, T. (2016, sep). A radiation-hydrodynamics model of accretion columns for ultra-luminous x-ray pulsars. *Publications of the Astronomical Society of Japan*, *68*(5), 83.

Kawashima, T., & Ohsuga, K. (2020, 02). Super-critical column accretion on to strongly magnetized neutron stars in ULX pulsars. *Publications of the Astronomical Society of Japan*, *72*(1).
(15)

Kayanikhoo, F., Čemeljić, M., Wielgus, M., & Kluźniak, W. (2023a). *Energy dissipation in astrophysical simulations: results of the orszag-tang test problem.*

Kayanikhoo, F., Čemeljić, M., Wielgus, M., & Kluźniak, W. (2023b, 12). Energy distribution and substructure formation in astrophysical MHD simulations. *Monthly Notices of the Royal Astronomical Society*, *527*(4), 10151-10167.

King, A., & Lasota, J.-P. (2019). No magnetars in ulxs. *Monthly Notices of the Royal Astronomical Society*, *485*(3), 3588–3594.

King, A., & Lasota, J.-P. (2020, 04). Pulsing and non-pulsing ULXs: the iceberg emerges. *Monthly Notices of the Royal Astronomical Society*, *494*(3), 3611-3615.

King, A., Lasota, J.-P., & Kluźniak, W. (2017, 02). Pulsing ULXs: tip of the iceberg? *Monthly Notices of the Royal Astronomical Society: Letters*, *468*(1), L59-L62.

King, A., Lasota, J.-P., & Middleton, M. (2023, June). Ultraluminous x-ray sources. *New Astronomy Reviews*, *96*, 101672.

King, A. R. (2009, February). Masses, beaming and Eddington ratios in ultraluminous X-ray sources. MNRAS, *393*(1), L41-L44.

King, A. R., Davies, M. B., Ward, M. J., Fabbiano, G., & Elvis, M. (2001, apr). Ultraluminous x-ray sources in external galaxies. *The Astrophysical Journal*, *552*(2), L109.

Kluźniak, W., & Lasota, J.-P. (2015, 01). An ultraluminous nascent millisecond pulsar. *Monthly Notices of the Royal Astronomical Society: Letters*, *448*(1), L43-L47.

Komissarov, S. S. (1999, 02). A Godunov-type scheme for relativistic magnetohydrodynamics. *Monthly Notices of the Royal Astronomical Society*, *303*(2), 343-366.

Kretschmar, P., Fürst, F., Sidoli, L., Bozzo, E., Alfonso-Garzón, J., Bodaghee, A., Chaty, S., Chernyakova, M., Ferrigno, C., Manousakis, A., Negueruela, I., Postnov, K., Paizis, A., Reig, P., Rodes-Roca, J. J., Tsygankov, S., Bird, A. J., Bissinger né Kühnel, M., Blay, P., Caballero, I., Coe, M. J., Domingo, A., Doroshenko, V., Ducci, L., Falanga, M., Grebenev, S. A., Grinberg, V., Hemphill, P., Kreykenbohm, I., Kreykenbohm né Fritz, S., Li, J., Lutovinov, A. A., Martínez-Núñez, S., Mas-Hesse, J. M., Masetti, N., McBride, V. A., Neronov, A., Pottschmidt, K., Rodriguez, J., Romano, P., Rothschild, R. E., Santangelo, A., Sguera, V., Staubert, R., Tomsick, J. A., Torrejón, J. M., Torres, D. F., Walter, R., Wilms, J., Wilson-Hodge, C. A., & Zhang, S. (2019). Advances in understanding high-mass x-ray binaries with integraland future directions. *New Astronomy Reviews*, *86*, 101546.

Lančová, D., Abarca, D., Kluźniak, W., Wielgus, M., Sądowski, A., Narayan, R., Schee, J., Török, G., & Abramowicz, M. (2019, October). Puffy Accretion Disks: Sub-Eddington, Optically Thick, and Stable. ApJ, *884*(2), L37.

Lasota, J., & King, A. (2023, 09). Ultraluminous X-ray sources are beamed. *Monthly Notices of the Royal Astronomical Society*, *526*(2), 2506-2509.

Lasota, J.-P. (2024). *Problems in the astrophysics of accretion onto compact celestial bodies.*

Matsushita, S., Kawabe, R., Matsumoto, H., Tsuru, T. G., Kohno, K., Morita, K. I., Okumura, S. K., & Vila-Vilaro, B. (2000). Formation of a massive black hole at the center of the superbubble in m82. *Astrophys. J. Lett.*, *545*, L107.

McKinney, J. C., Dai, L., & Avara, M. J. (2015, 09). Efficiency of super-Eddington magnetically-arrested accretion. *Monthly Notices of the Royal Astronomical Society: Letters*, *454*(1), L6-L10.

McKinney, W., et al. (2010). Data structures for statistical computing in python. In *Scipy* (Vol. 445, pp. 51–56).

Meyer-Hofmeister, E., Cheng, H., & Liu, B. F. (2024, 6). A large population of neutron star low-mass X-ray binaries with long outburst recurrence time ? MNRAS.

Mihalas, D., & Mihalas, B. W. (1984). *Foundations of radiation hydrodynamics.*

Mishra, B., Fragile, P. C., Johnson, L. C., & Kluźniak, W. (2016, 09). Three-dimensional, global, radiative GRMHD simulations of a thermally unstable disc. *Monthly Notices of the Royal Astronomical Society*, *463*(4), 3437-3448.

Motch, C., Pakull, M. W., Soria, R., Grisé, F., & Pietrzyński, G. (2014, oct). A mass of less than 15 solar masses for the black hole in an ultraluminous x-ray source. *Nature*, *514*(7521), 198–201.

Murguia-Berthier, A., Parfrey, K., Tchekhovskoy, A., & Jacquemin-Ide, J. (2024, jan). From feast to famine: A systematic study of accretion onto oblique pulsars with 3d grmhd simulations. *The Astrophysical Journal Letters*, *961*(1), L20.

Mushtukov, A. A., Suleimanov, V. F., Tsygankov, S. S., & Poutanen, J. (2015, January). The critical accretion luminosity for magnetized neutron stars. *Monthly Notices publisher=Oxford Universof the Royal Astronomical Society,ity Press (OUP)*, *447*(2), 1847–1856.

Narayan, R., Sądowski, A., Penna, R. F., & Kulkarni, A. K. (2012, 11). GRMHD simulations of magnetized advection-dominated accretion on a non-spinning black

hole: role of outflows. *Monthly Notices of the Royal Astronomical Society*, *426*(4), 3241-3259.

Narayan, R., Zhu, Y., Psaltis, D., & Sądowski, A. (2016). Heroic: 3d general relativistic radiative post-processor with comptonization for black hole accretion discs. *Monthly Notices of the Royal Astronomical Society*, *457*(1), 608–628.

Noble, S. C., Gammie, C. F., McKinney, J. C., & Del Zanna, L. (2006, April). Primitive Variable Solvers for Conservative General Relativistic Magnetohydrodynamics. ApJ, *641*(1), 626-637.

Ohsuga, K., Mineshige, S., Mori, M., & Umemura, M. (2002, jul). Does the slim-disk model correctly consider photon-trapping effects? *The Astrophysical Journal*, *574*(1), 315.

Paczynski, B. (1992). Gb 790305 as a very strongly magnetized neutron star. *Acta Astronomica (ISSN 0001-5237), vol. 42, no. 3, p. 145-153.*, *42*, 145–153.

Papitto, A., & Torres, D. F. (2015, jun). A propeller model for the sub-luminous state of the transitional millisecond pulsar psr j1023+0038. *The Astrophysical Journal*, *807*(1), 33.

Parfrey, K., & Tchekhovskoy, A. (2017, December). General-relativistic Simulations of Four States of Accretion onto Millisecond Pulsars. *The Astrophysical Journal, Ltter*, *851*, L34.

Penna, R. F., Kulkarni, A., & Narayan, R. (2013, November). A new equilibrium torus solution and GRMHD initial conditions. A&A, *559*, A116.

Revnivtsev, M., & Mereghetti, S. (2014, December). Magnetic fields of neutron stars in x-ray binaries. *Space Science Reviews*, *191*(1–4), 293–314.

Revnivtsev, M., & Mereghetti, S. (2018). The strongest magnetic fields in the universe. In V. Beskin et al. (Eds.), *The strongest magnetic fields in the universe* (p. p. 299). New York, NY: Springer New York.

Romanova, M. M., Koldoba, A. V., Ustyugova, G. V., Blinova, A. A., Lai, D., & Lovelace, R. V. E. (2021, 06). 3D MHD simulations of accretion on to stars with tilted magnetic and rotational axes. *Monthly Notices of the Royal Astronomical Society*, *506*(1), 372-384.

Sądowski, A., & Narayan, R. (2015, 10). Photon-conserving Comptonization in simulations of accretion discs around black holes. *Monthly Notices of the Royal Astronomical Society*, *454*(3), 2372-2380.

Sądowski, A., & Narayan, R. (2016, 01). Three-dimensional simulations of super-critical black hole accretion discs–luminosities, photon trapping and variability. *Monthly Notices of the Royal Astronomical Society*, *456*(4), 3929-3947.

Sądowski, A., Narayan, R., Tchekhovskoy, A., Abarca, D., Zhu, Y., & McKinney, J. C. (2014, 12). Global simulations of axisymmetric radiative black hole accretion discs in general relativity with a mean-field magnetic dynamo. *Monthly Notices of the Royal Astronomical Society*, *447*(1), 49-71.

Sądowski, A., Narayan, R., Tchekhovskoy, A., & Zhu, Y. (2013, 01). Semi-implicit scheme for treating radiation under M1 closure in general relativistic conservative fluid dynamics codes. *Monthly Notices of the Royal Astronomical Society*, *429*(4), 3533-3550.

Shakura, N. I., & Sunyaev, R. A. (1973, January). Black holes in binary systems. Observational appearance. A&A, *24*, 337-355.

Shklovsky, I. S. (1967, April). On the Nature of the Source of X-Ray Emission of Sco XR-1. ApJ, *148*, L1.

Sądowski, A. (2011, August). Slim accretion disks around black holes. *arXiv e-prints*, arXiv:1108.0396.

Sądowski, A., Lasota, J.-P., Abramowicz, M. A., & Narayan, R. (2016, March). Energy flows in thick accretion discs and their consequences for black hole feedback. MNRAS, *456*(4), 3915-3928.

Sądowski, A., Narayan, R., Tchekhovskoy, A., Abarca, D., Zhu, Y., & McKinney, J. C. (2015, February). Global simulations of axisymmetric radiative black hole accretion discs in general relativity with a mean-field magnetic dynamo. *Monthly Notices of the Royal Astronomical Society*, *447*, 49-71.

Sądowski, A., Narayan, R., Tchekhovskoy, A., & Zhu, Y. (2013, March). Semi-implicit scheme for treating radiation under M1 closure in general relativistic conservative fluid dynamics codes. *Monthly Notices of the Royal Astronomical Society*, *429*(4), 3533-3550.

Syunyaev, R. A., & Shakura, N. I. (1986, April). Disk Accretion onto a Weak Field Neutron Star - Boundary Layer Disk Luminosity Ratio. *Soviet Astronomy Letters*, *12*, 117-120.

Sądowski, A., & Narayan, R. (2016, 01). Three-dimensional simulations of super-critical black hole accretion discs – luminosities, photon trapping and variability. *Monthly Notices of the Royal Astronomical Society*, *456*(4), 3929-3947.

Sądowski, A., Narayan, R., McKinney, J. C., & Tchekhovskoy, A. (2014, 01). Numerical simulations of super-critical black hole accretion flows in general relativity. *Monthly Notices of the Royal Astronomical Society*, *439*(1), 503-520.

Takahashi, H. R., Mineshige, S., & Ohsuga, K. (2018, jan). Supercritical accretion onto a non-magnetized neutron star: Why is it feasible? *The Astrophysical Journal*, *853*(1), 45.

Takahashi, H. R., & Ohsuga, K. (2017, aug). General relativistic radiation MHD simulations of supercritical accretion onto a magnetized neutron star: Modeling of ultraluminous x-ray pulsars. *The Astrophysical Journal*, *845*(1), L9.

Takasao, S., Tomida, K., Iwasaki, K., & Suzuki, T. K. (2018, apr). A three-dimensional simulation of a magnetized accretion disk: Fast funnel accretion onto a weakly magnetized star. *The Astrophysical Journal*, *857*(1), 4.

Tomsick, J. A., Gelino, D. M., Halpern, J. P., & Kaaret, P. (2004, aug). The low quiescent x-ray luminosity of the neutron star transient xte j2123–058. *The Astrophysical Journal*, *610*(2), 933.

Townsend, L. J., Kennea, J. A., Coe, M. J., McBride, V. A., Buckley, D. A. H., Evans, P. A., & Udalski, A. (2017, 07). The 2016 super-Eddington outburst of SMC X-3: X-ray and optical properties and system parameters. *Monthly Notices of the Royal Astronomical Society*, *471*(4), 3878-3887.

Trudolyubov, S. P. (2008, 06). XMM-Newton discovery of transient X-ray pulsar in NGC 1313. *Monthly Notices of the Royal Astronomical Society: Letters*, *387*(1), L36-L40.

Truemper, J., Pietsch, W., Reppin, C., Voges, W., Staubert, R., & Kendziorra, E. (1978, February). Evidence for strong cyclotron line emission in the hard X-ray spectrum of Hercules X-1. ApJ, *219*, L105-L110.

Tsygankov, S. S., Doroshenko, V., Lutovinov, A. A., Mushtukov, A. A., & Poutanen, J. (2017). Smc: the closest ultraluminous x-ray source powered by a neutron star with non-dipole magnetic field. *A&A*, *605*, A39.

van der Walt, S., Colbert, S. C., & Varoquaux, G. (2011, March). The NumPy Array: A Structure for Efficient Numerical Computation. *Computing in Science and Engineering*, *13*(2), 22-30.

Vasilopoulos, G., Petropoulou, M., Koliopanos, F., Ray, P. S., Bailyn, C. B., Haberl, F., & Gendreau, K. (2019, 08). NGC 300 ULX1: spin evolution, super-Eddington accretion, and outflows. *Monthly Notices of the Royal Astronomical Society*, *488*(4), 5225-5231.

Walton, D. J., Mackenzie, A. D. A., Gully, H., Patel, N. R., Roberts, T. P., Earnshaw, H. P., & Mateos, S. (2022, January). A multimission catalogue of ultraluminous X-ray source candidates. *Monthly Notices of the Royal Astronomical Society*, *509*(2), 1587-1604.

Wasserman, I., & Shapiro, S. L. (1983, Feb). Masses, radii, and magnetic fields of pulsating X-ray sources : is the "standard" model self-consistent ? ApJ, *265*, 1036-1046.

Yang, H., & Li, X. (2023, mar). Magnetic inclination evolution of accreting neutron stars in intermediate/low-mass x-ray binaries. *The Astrophysical Journal*, *945*(1), 2.

Zhang, L., Blaes, O., & Jiang, Y.-F. (2023, jan). Dynamics of neutron star accretion columns in split-monopole magnetic fields. *Monthly Notices of the Royal Astronomical Society*, *520*(1), 1421–1438.